

University of Stuttgart
Germany



MAX-PLANCK-GESELLSCHAFT

Resolving Tunneling Processes into Yu-Shiba-Rusinov States under Microwave Irradiation

Von der Fakultät Mathematik und Physik der Universität Stuttgart zur Erlangung der Würde
eines Doktors der Naturwissenschaften (Dr. rer. nat.) genehmigte Abhandlung

Vorgelegt von

Janis Noah Malte Siebrecht

aus Heidelberg

Hauptberichter:	Dr. habil. Christian Ast
Mitberichter:	Prof. Dr. Sebastian Loth
Prüfungsvorsitzende:	Prof. Dr. Maria Daghofer

Tag der mündlichen Prüfung: 23.03.2023

Max-Planck-Institut für Festkörperforschung
Universität Stuttgart
2023

Abstract

This thesis presents the construction and optimization of a scanning tunneling microscope which is then used to study tunneling processes into magnetic impurities in a superconductor-superconductor junction under microwave irradiation.

We start with the construction of a scanning tunneling microscope (STM) operating at a base temperature of 0.56 K using a Joule-Thomson ^3He cycle. We apply a number of modifications, most notably the addition of powder filters at the (cold) scan head, to reduce the width of the Josephson effect from $96\text{ }\mu\text{V}$ to $12\text{ }\mu\text{V}$. This width is closely related to the energy resolution and we conclude that this setup can compete with state-of-the-art mK-STMs when it comes to energy resolution.

Magnetic impurities on superconductors lead to single levels inside the superconducting gap – so called Yu-Shiba-Rusinov (YSR) states. We study the system of YSR states on a vanadium tip in contact with a superconducting V(100) surface. We expose this system to microwaves in the range of 60 to 90 GHz by means of an external antenna. We observe the emergence of a family of peaks which is not predicted by Tien-Gordon theory. We account for these peaks by considering the fact that tunneling into YSR states must preserve parity. It is therefore a two-step process where the YSR state is first excited by the tunneling electron and then subsequently relaxes. With the help of microwaves, we enable a second process. Here, the microwaves excite the YSR state and its relaxation can be observed. This process is not possible without microwaves and we label the family of peaks originating from this process *excited state tunneling*. Accessing the excited state of YSR states is a first step towards manipulation of YSR states by microwave driving.

We corroborate the experimental observations with theoretical modelling based on a Green's functions approach. We observe that the full approach reproduces the features seen in the experimental data. A simplified model covers the main physics on a qualitative level. This model includes a threshold which needs to be overcome to excite the YSR state with microwaves. Additionally, we find that the resonant nature of this tunneling process necessitates higher-order calculations. In particular, the lowest order approximation breaks down at conductances two orders of magnitude lower compared to the situation without microwaves. This implies that microwave-assisted tunneling into YSR states could be a useful platform for studying higher order processes.

Overall this thesis presents a technological improvement which makes it possible to resolve

a hitherto unseen microwave-assisted tunneling process into YSR states. This process excites the YSR state and is therefore a basis for the manipulation of YSR states using microwaves. Our analysis reveals the necessity of a higher-order Green's functions approach to describe the observed resonances quantitatively.

Zusammenfassung

Diese Dissertation präsentiert die Konstruktion und die Optimierung eines Rastertunnelmikroskops, das dann benutzt wird, um Tunnelprozesse in magnetische Störstellen in einem Supraleiter-Supraleiter Tunnelkontakt unter Mikrowelleneinstrahlung zu untersuchen.

Wir beginnen mit der Konstruktion eines Rastertunnelmikroskops (RTM), das bei einer Basistemperatur von 0.56 K mit einem ^3He -Zyklus arbeitet. Wir nehmen eine Reihe von Änderungen vor, allen voran die Aufnahme von Pulver-Filtern am (kalten) Scankopf, um die Breite des Josephson Effects von $96\ \mu\text{V}$ auf $12\ \mu\text{V}$ zu reduzieren. Die Breite hängt mit der Energieauflösung eng zusammen und wir schlussfolgern, dass dieses System in Bezug auf Energieauflösung mit state-of-the-art mK-RTMs konkurrieren kann.

Magnetische Störstellen auf Supraleitern führen zu einzelnen Energieniveaus in der supraleitenden Lücke, so genannte Yu-Shiba-Rusinov (YSR) Zustände. Wir untersuchen das System von YSR Zuständen auf einer Vanadium Spitze, die im Kontakt mit einer supraleitenden V(100) Oberfläche steht. Wir setzen das System Mikrowellen im Bereich von 60 bis 90 GHz mit Hilfe einer externen Antenne aus. Wir beobachten, dass sich eine Reihe von Peaks bildet, die nicht von der Tien-Gordon Theorie vorhergesagt werden. Wir erklären diese Peaks mit Hilfe der Tatsache, dass Tunneln in YSR Zustände die Parität erhalten muss. Es handelt sich daher um einen zweischrittigen Prozess, bei dem der YSR Zustand zuerst von einem tunnelden Elektron angeregt wird und danach relaxiert. Mit Hilfe der Mikrowellen realisieren wir einen zweiten Prozess. Hier regen die Mikrowellen den Zustand an und seine Relaxation kann beobachtet werden. Dieser Prozess ist ohne Mikrowellen nicht möglich und wir bezeichnen die Peaks, die zu diesem Prozess gehören, *Tunneln in den angeregten Zustand*. Die Ansteuerung des angeregten YSR Zustandes ist ein erster Schritt in die Richtung der Manipulation von YSR Zuständen mit Mikrowellen.

Wir untermauern die experimentellen Beobachtungen mit theoretischen Modellierungen, die auf Green's Funktionen basieren. Wir beobachten, dass der volle Ansatz das experimentelle Verhalten reproduziert. Ein vereinfachtes Modell beschreibt die physikalischen Vorgänge auf einer qualitativen Ebene. Dieses Model umfasst eine Schwelle, die überschritten werden muss, um den YSR Zustand mit Mikrowellen anzuregen. Zusätzlich erkennen wir, dass die resonante Natur dieses Tunnelprozesses Berechnungen zu höherer Ordnung erfordert. Genauer gesagt bricht die Näherung zu niedrigster Ordnung bei einer Leitfähigkeit zusammen, die zwei Größenordnungen kleiner ist im Vergleich zu einer Situation ohne Mikrowellen. Dies bedeutet, dass Mikrowellen-assistiertes Tunneln in YSR Zustände ein nützliches System zur Untersuchung

von Prozessen höherer Ordnung sein könnte.

Insgesamt stellt diese Arbeit eine technologische Verbesserung vor, die es ermöglicht, einen bisher noch nicht beobachteten Mikrowellen-assistierten Tunnelprozess in YSR Zustände aufzulösen. Dieser Prozess regt den YSR Zustand an und ist daher ein Ausgangspunkt für die Manipulation von YSR Zuständen mit Mikrowellen. Unsere Analyse zeigt auf, dass Green's Funktionen von höherer Ordnung notwendig sind, um die beobachteten Resonanzen quantitativ zu beschreiben.

Contents

1	Introduction	1
2	Theoretical Background	4
2.1	Introduction to Scanning Tunneling Microscopy	5
2.1.1	Tunneling Effect	5
2.1.2	Concept of a Scanning Tunneling Microscope	6
2.1.3	Mathematical Description	7
2.1.4	Technical Challenges	8
2.2	Recent Advances in Scanning Tunneling Microscopy	8
2.3	Green's Functions and the Tunneling Current	11
2.4	Electronic transport in STM	12
2.5	Superconductivity	14
2.5.1	Macroscopic Description	14
2.5.2	Microscopic Description	14
2.6	Yu-Shiba-Rusinov States	18
2.6.1	Basic Theory of YSR States	18
2.6.2	Relation of YSR states to Quantum dots	22
2.6.3	Recent Experiments on YSR States	23
2.6.4	Majorana Bound States	25
2.7	The Phase in Tunnel Junctions	25
2.8	Microwave-Assisted Tunneling	27
2.9	The Josephson Effect	29
2.10	(Multiple) Andreev Reflections	31
3	Experimental Setup	37

3.1	Basic Layout	37
3.2	Design of the Scan Head	38
3.3	Electrical Connections	40
3.4	Microwave Antenna	44
3.5	Design of the ^3He Cryostat	46
3.6	Vibration Isolation	49
3.7	Outlook: New light sources	50
4	Energy Resolution of the New Setup	52
4.1	Cold Filters	52
4.2	Noise Reduction Strategies	55
4.3	Josephson Effect Data	56
4.4	Height of Coherence Peaks	59
4.5	Outlook	60
5	Microwave Excitation of YSR States	62
5.1	YSR states on a Vanadium tip	62
5.2	Sample and Tip Preparation	63
5.3	Observation of Anomalous Peaks	65
5.4	Frequency-Dependent Measurements	67
5.4.1	Transfer Function	67
5.4.2	Constant Amplitude Sweeps	69
5.4.3	Physical Picture	71
5.5	Derivation of a Modified Tien-Gordon Equation	74
5.5.1	Full Green's Function Approach	74
5.5.2	Simplified Model	79
5.6	Outlook	84
6	Modeling the Conductance Dependence	87
6.1	Model and Parameters	87
6.2	Validity of the Models	89

6.3	Peak Evolution with Conductance	93
6.4	Outlook	96
7	Conclusion and Outlook	97

List of Figures

2.1	Schematic of the 1D Schrödinger equation	5
2.2	Schematic of a scanning tunneling microscope	6
2.3	Illustration of the equation for tunneling	7
2.4	Schematic of the different variations in STM	9
2.5	Plots of the BCS density of states	16
2.6	dI/dV of superconductor-superconductor tunneling.	17
2.7	Schematic of the Anderson Impurity Model	20
2.8	Calculated dI/dV of BCS-YSR tunneling.	20
2.9	Calculated temperature-dependent YSR-BCS spectra	21
2.10	Schematic of a quantum dot	22
2.11	Schematic of a quantum phase transition of a YSR state	24
2.12	Model conductance map generated with the Tien-Gordon equation	28
2.13	Illustration of the inversion of the Tien-Gordon equation	29
2.14	Schematic explaining the Josephson effect	30
2.15	Schematic of MARs between two superconductors	32
2.16	Modelling of Andreev reflections	32
2.17	Andreev reflections in a SC-SC junction	34
2.18	Andreev bound state	35
3.1	3D drawing of the whole experimental setup	38
3.2	3D drawing of the tunnel junction	39
3.3	Two versions for the orientation of the piezoelectric scanner	39
3.4	Schematic of the measurement lines for the tunneling current	40
3.5	Schematic of the cables and thermalization used inside the cryostat	41
3.6	Cross-section of the interface	42

3.7	Design of the E-Band antenna	44
3.8	Comparison of the two commercial adapters	45
3.9	Cabling to the antenna	46
3.10	Schematic of the two modes of cryostat operation	48
3.11	Vibration spectra of different damping stages	50
3.12	Design of the Josephson junction array	51
4.1	Transmission of home-built powder filters	53
4.2	Transmission of commercial π -filters at low temperatures	54
4.3	Schematic of the improved setup	55
4.4	Power spectral density of the setup (a) before and (b) after the improvements . .	56
4.5	Josephson effect (a) before and (b) after improvements	57
4.6	Josephson effect as a function of conductance	58
4.7	Superconductor- superconductor spectra	60
5.1	Topographies of a V(100) surface	63
5.2	Algorithm for generating a YSR state on the tip	64
5.3	Normalized dI/dV curves of various YSR states	65
5.4	False color plots of spectra as a function of MW intensity at 61 GHz	66
5.5	False color plots of spectra as a function of MW intensity at 89.2 GHz	67
5.6	Illustration of the transfer function feedback algorithm	68
5.7	Plots of the transfer function	69
5.8	Frequency dependent RF spectra	70
5.9	YSR spectra with microwaves	71
5.10	Schematic of the ground state and excited state tunneling processes	72
5.11	Comparison of the electron and Andreev picture	74
5.12	Comparison of Gaussian and Dynes broadening	75
5.13	Fitting using the full approach	76
5.14	Fitting of amplitude-dependent maps	77
5.15	Modelling the frequency-dependent measurements	78

5.16	Illustration of the algorithm related to the modified TG equation	82
5.17	Analysis of the evolution of excited state tunneling with the dimensionless amplitude α	83
5.18	Color coding of experimental data	84
5.19	Spectra with pulsed microwaves	86
6.1	Extraction of the parameters for the model	88
6.2	Dependence of peaks on the lifetime of the YSR state	89
6.3	Evolution of calculated spectra with conductance	91
6.4	Evolution of calculated microwave spectra with conductance	92
6.5	Evolution of experimental spectra with conductance	94
6.6	Evolution of peak height with conductance	95

List of Tables

2.1	List of systems showing YSR states in STM measurements	23
3.1	Comparison of the properties of ^3He and ^4He	47

List of Acronyms

ABS	Andreev bound state
AC	alternating current
AR	Andreev reflection
AFM	atomic force microscope
BCS	Bardeen-Cooper-Schrieffer
BSCCO	$\text{Bi}_2\text{Sr}_2\text{Ca}_{n-1}\text{Cu}_n\text{O}_{2n+4+x}$
CW	continuous wave
DC	direct current
ESR	electron spin resonance
EST	excited state tunneling
GST	ground state tunneling
JJ	Josephson junction
JT	Joule-Thomson
MAR	multiple Andreev reflection
MW	microwave
PEEK	polyether ether ketone
PTFE	polytetrafluoroethylene
PZT	lead zirconate titanate
QD	quantum dot
QP	quasiparticle
QPT	quantum phase transition
RCSJ	resistively and capacitively shunted Josephson junction
RF	radio frequency
RMS	root mean square
SC	superconductor
SIS	superconductor-insulator-superconductor
SR	semirigid
STM	scanning tunneling microscope
TG	Tien-Gordon
UHV	ultra-high vacuum
YSR	Yu-Shiba-Rusinov

1

Introduction

Energy is one of the most fundamental concepts not only in physics, but throughout quantitative science in general. Whenever a process happens, it can be described in terms of the potential to do work, i.e. energy. This may range from the scale of $3 M_{\odot} c^2 = 5 \times 10^{47} \text{ J}$ (as in the case of gravitational waves released by the merging of two black holes [1] – here M_{\odot} is the solar mass and c the speed of light) to as little as $h \times 1420 \text{ MHz} = 6 \mu\text{eV}$ (as in the case in the hyperfine transition of the hydrogen atom [2] – here h is Planck’s constant). Indeed, when speaking about quantized energy transfer – namely transitions between single levels, there is immediately a technological interest, namely the quest for qubits. With data storage becoming increasingly important in the modern world, the miniaturization of information storage is a rapidly growing area of research. The lowest limit to this would be storing information in a single state. Such qubits have already been demonstrated in various systems such as electron donors in semiconductors [3] or quantum dots [4]. One of the most versatile techniques in this context is scanning tunneling microscopy (STM) [5]. It offers the ability to image single atoms, manipulate them [6] and most importantly, probe them using bias voltage spectroscopy. Looking at it in terms of energy, there has been a constant effort to improve the energy resolution, reaching down to $9 \mu\text{eV}$ [7], which brings us to the lower end of the energy scale previously mentioned.

It is precisely at this bottom of the energy scale where the work of this thesis was carried out. In the first part, we present how we arrived there – how we obtained an energy resolution of $12 \mu\text{eV}$. To do so, one has to keep in mind that if one wants to investigate phenomena with small energies, the thermal energy $k_{\text{B}}T$ can become a nuisance and any of these experiments requires cooling. Now the dilution refrigerator has been available since the 1960s [8] and with laser cooling, researchers have even achieved μK temperatures in atomic gases [9], even though in that case temperature only refers to the thermal energy of a small number of atoms. Cooling an entire STM is challenging and it took several decades for the appearance of the first mK-STMs [10–12]. In addition to that, electronic noise poses another major challenge to high-resolution measurements, requiring sophisticated filtering and grounding strategies [7, 13, 14]. Various

improvements have been suggested and here we implement metal powder filters [15] (amongst other improvements) and achieve an energy resolution of $12 \mu\text{eV}$, demonstrating firstly that the current mK machines are not nearly at the limit in terms of energy resolution and secondly, that such energy resolutions are possible even for pure ^3He systems.

The most famous phenomenon associated with low temperatures is superconductivity. Aside from the benefits which a dissipationless current can hold, the tunneling of Cooper pairs between two superconductors, i.e. the Josephson effect, opens a rich area of research applications, ranging from detection devices (superconducting quantum interference device – SQUID) [16] to a definition of the voltage standard [17]. Josephson junctions have already lived up to their promise for coherent manipulation, leading to so-called "phase qubits" [18, 19]. Keeping in mind such advantages that superconductivity holds for the study of quantum phenomena, we chose to work with impurities on YSR for the second and main part of this thesis. YSR states are localized states due to magnetic adatoms on a superconductor. The magnetic moment can break a Cooper pair, leading to sub-gap states. Because there are no quasiparticles inside the gap, the level is protected, making it an ideal candidate for the study of two-level physics. Knowing that one of the requirements for qubit operations set forth by DiVincenzo [20] is manipulation, we use microwaves to interact with YSR states, or more precisely to interact with the tunneling process into YSR states. We find that microwaves can interact with an Andreev process to excite the YSR state. In particular, we see two families of processes – one where the YSR state is excited by the tunneling process and then relaxes by interaction with the microwave field – and another one where the microwave field excites the YSR state which then subsequently relaxes by tunneling across the junction. This second process, which we call *excited state tunneling*, could be used as a starting point for pump probe schemes to truly control the YSR state in a coherent manner. Apart from this outlook on control of quantum states, the study of YSR states under microwave irradiation is insightful from a perspective of resonance. Resonant phenomena have in common that if the driving is tuned to a natural frequency of the system, a strongly non-linear response is seen [21, 22]. Here, the resonant driving of the YSR states leads to a breakdown of simple models which consider just the lowest order Andreev reflections. We find that for driven YSR-superconductor junctions, a full Green's function approach is necessary at conductances two orders of magnitude lower than in the case of the undriven system. This implies that the modeling of similar work [23] should be treated with care. Drawing a connection to the beginning, this work can be seen from an energy perspective. We explore techniques to improve our energy resolution, then probe our system in a regime where the microwave energy matches an energy scale in the system and both are larger than the thermal energy, i.e. $\hbar\omega \sim E_{\text{system}} > k_{\text{B}}T$.

This thesis follows a traditional structure. It starts by laying out the key theories relevant for this work. Most importantly, it introduces the technique of scanning tunneling microscopy and presents a brief overview of the different extensions to this technique. Then, we present Green's functions as a tool to describe tunneling processes in STM and give an overview of

superconductivity, in particular in the context of STM. Being closely connected to superconductivity, YSR states are the natural next section of the thesis. We conclude the theory chapter with a study of microwave-assisted tunneling as well as higher order tunneling processes. The second chapter is a record of the experimental setup which was constructed in the scope of this thesis. We focus on the design of the scan head, the choice of material for electrical connections and the vibration isolation. Chapter 4 demonstrates the effect of these strategies and shows data obtained after the installation of the powder filters. It contains data illustrating how the width of the Josephson effect reduces with these improvements. With this high energy resolution, we study YSR states under microwave irradiation in Chapter 5. We find anomalous peaks and present a simplified theory to explain this family of peaks as a microwave-enabled excitation of the YSR state with subsequent resonant relaxation. The penultimate chapter is devoted to an analysis of the validity of various models and simplifications to understand that higher order processes become relevant at low transparencies ($\tau < 10^{-3}$) under microwave irradiation. Finally, we summarize this work and give an outlook for future endeavors.

2

Theoretical Background

This chapter provides the background knowledge needed to understand the ensuing chapters. The first two sections cover scanning tunneling microscopy, giving both a mathematical description and presenting some of the main extensions to STM which have been developed. Given that higher order tunneling processes play an important role in this work, this chapter also reviews a Green's function approach for describing the tunneling current. This approach is then used to give a mathematical account of superconductivity and Yu-Shiba-Rusinov (YSR) states. This foundation is particularly relevant for Chapters 5 and 6. Finally, we give an account of microwave-assisted tunneling and introduce higher order phenomena such as the Josephson effect and multiple Andreev reflections which are key for understanding the work about the energy resolution (Chapter 4) and the analysis of the conductance dependence of microwave-assisted tunneling (Chapter 6), respectively.

2.1 Introduction to Scanning Tunneling Microscopy

2.1.1 Tunneling Effect

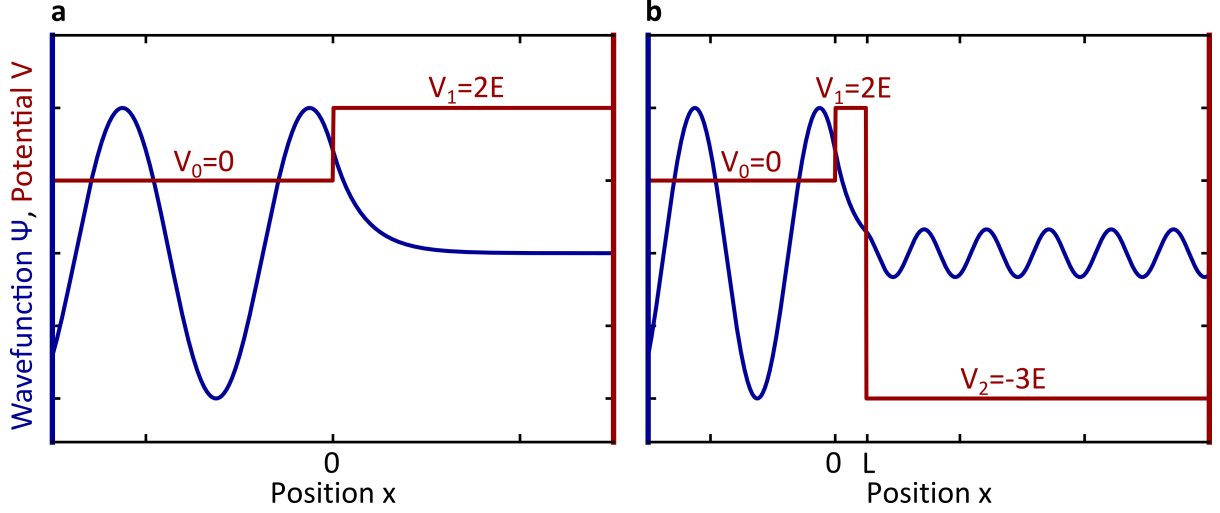


Figure 2.1: Schematic of the 1D Schrödinger equation. (a) shows the solution with a potential step $V_1 = 2E$ and (b) with a return to a potential $V_2 = -3E$ after length L .

Consider a time-independent Schrödinger equation with a step-like potential of height $V_0 = 2E$ as shown in Figure 2.1(a). Here Ψ is the wavefunction, E the energy, m the mass of the particle and $\Theta(x)$ the Heaviside step function:

$$\left(-\frac{\hbar^2}{2m} \frac{\partial^2}{\partial x^2} + V_0 \Theta(x) \right) \Psi = E \Psi \quad (2.1)$$

There are oscillatory solutions with wave vectors $k = \sqrt{\frac{2mE}{\hbar^2}}$ for $x < 0$ and there is an exponential decay with decay constant $\kappa = \sqrt{\frac{2mE}{\hbar^2}}$ for $x \geq 0$. This means that there is non-zero probability to find the particle in the classically forbidden region $x \geq 0$.

If we now reduce the barrier to $V_2 < E$ for some $x > L$, the particle can again propagate in the region $x > L$ as shown in Figure 2.1(b). This transfer through the forbidden region is called tunneling because the particle can cross the barrier of V_0 without having sufficient energy to overcome it classically. Another important observation from this simple problem is the fact that the wavefunction in the classically forbidden region decays exponentially, meaning that the amplitude in the region $x > L$ is exponentially sensitive to variations in the barrier length L . More precisely, if we define an incoming wavefunction for $x < 0$ as $\psi_{\text{inc}}(x) = Ae^{ikx}$ (where A is a normalization factor) and a transmitted wavefunction $\psi_{\text{trans}}(x) = Ate^{ik_1x}$, then it turns out that the transmission probability $T = |t|^2$ (in the case of $\kappa L \ll 1$ where $\kappa = \sqrt{\frac{2m(V_0-E)}{\hbar^2}}$)

evolves as [24]:

$$T \propto e^{-2\kappa L} \quad (2.2)$$

Now in real physical systems, there are two quantities which determine the height of the barriers: firstly the work function $W = -E_F - e\phi$, which measures how much energy is needed to take an electron from the metal into vacuum (the Fermi level E_F), and secondly the electrical potential ϕ between the two materials, which determines the relative offset of the two Fermi levels. For most materials, the work function is of $O(\text{eV})$ [25], which means that $\kappa^{-1} = O(\text{\AA})$. This means that the tunneling current is sensitive to variations in the barrier width on the \AA scale.

2.1.2 Concept of a Scanning Tunneling Microscope

A scanning tunneling microscope (STM) exploits this tunneling effect. A schematic drawing is shown in Figure 2.2. A sharp tip is brought in tunnel contact with a sample. Then to measure a current, a bias voltage is applied between the tip and the sample. Based on this current, a feedback loop helps to find the correct position to reach a certain setpoint current. With this feedback loop active, the tip is then moved along x and y , allowing us to record the topography of the sample. Through the exponential dependence of the tunneling current on the distance, it is possible to achieve a vertical resolution on the order of 10 pm, which means that atomic resolution is possible. In contrast to other microscopy techniques, the resolution is much higher because there is no wavelength limitation as in light or electron microscopes. Additionally there are no lenses because there is no beam to focus, thereby eliminating another source of noise that is present in other microscopy techniques.

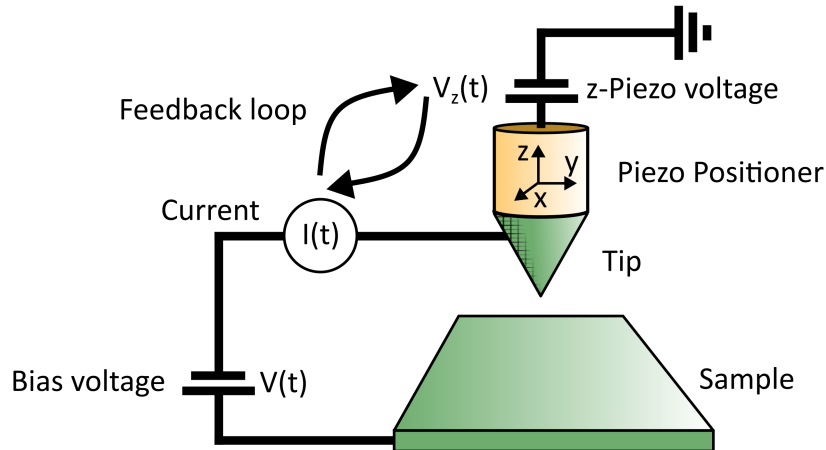


Figure 2.2: Schematic of a scanning tunneling microscope. The tip can be positioned using a piezoelectric tube. The position is found using a feedback loop between the current and the z -position.

2.1.3 Mathematical Description

A more rigorous approach is needed to describe the tunneling current quantitatively. Real materials have energy levels over a wide range of energies- i.e. density of states.

This can be treated within Bardeen's tunneling formalism [26]. This approach takes the unperturbed wavefunctions of tip $\Psi_{L,m}$ (with Hamiltonian H_L) and sample $\Psi_{R,m}$ (with Hamiltonian H_R). If we now consider a particle that is in state $|\Psi_{L,n}\rangle$ initially, then the presence of the sample is a perturbation. If the total Hamiltonian is H , then the perturbation $H - H_R$ will introduce solutions of the form:

$$\Psi(t) = \Psi_{L,n}(0)e^{-iE_n t/\hbar} + \sum_m a_{mn}(t)\Psi_{R,m}e^{-iE_m t/\hbar} \quad (2.3)$$

Importantly, the matrix element $M_{mn} = \langle \Psi_{L,m} | H - H_R | \Psi_{R,n} \rangle$ comes up in the calculation of time-dependent perturbation theory. Without presenting the detailed steps here, looking at equation 2.3, one can see that the sum over states in the sample leads to a density of states and that the coefficients $a(t)$ would be proportional to this matrix element and therefore decay exponentially with the width of the barrier. From this starting point, a formula for the tunneling current can be derived [27], where we set the Fermi levels to zero. Here ρ_L and ρ_R are densities of states, M is the matrix element and $f(E)$ is the Fermi function:

$$I(V) = \frac{4\pi e}{\hbar} \int_{-\infty}^{\infty} [f(E - eV) - f(E)] \rho_L(E - eV) \rho_R(E) |M|^2 dE \quad (2.4)$$

In other words, the tunneling current is a convolution of tip and sample density of states. If one is known, sweeping the bias voltage can give information about the other. Figure 2.3 illustrates this equation. The bias voltage shifts the Fermi levels relative to each other, allowing electrons to tunnel from an occupied to an unoccupied state. At finite temperatures, the Fermi level is smeared out by a width $k_B T$.

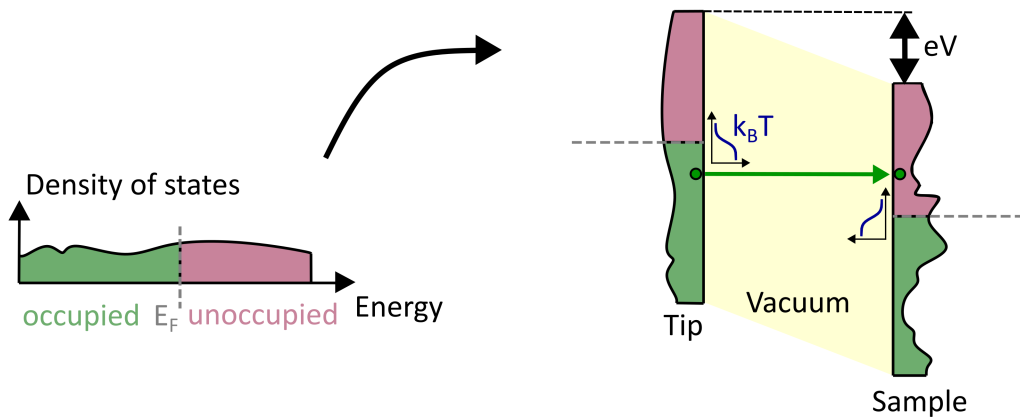


Figure 2.3: Illustration of the equation for tunneling. Tip and sample density of states are convolved with a thermal broadening.

An extension to this theory is the Tersoff-Hamann formula [28] which considers the geometric shape of the tip.

Now instead of the current, if we wish to access the density of states, we need to measure the derivative of the current, i.e. the conductance, directly. Here an AC modulation technique is helpful. A small modulation in the bias voltage $V(t) = V_0 + V_1 \cos(\omega t)$ induces a time dependent current:

$$I(V) = I(V_0) + \left(\frac{dI}{dV} \right)_{V_0} V_1 \cos(\omega t) + O(V_1^2) \quad (2.5)$$

Demodulating with a signal of the same frequency, we see that the demodulated current is to first order proportional to $\frac{dI}{dV}$. This is the most common technique to find the differential conductance. The amplitude of the lock-in can introduce additional noise [29]. In fact, if we consider the measurement of the demodulated current $\overline{I(V) \cos(\omega t)}$ averaged over one period $T = 2\pi/\omega$, we find, by substituting $\nu = V_1 \cos(\omega t)$ and integrating by parts:

$$\frac{1}{T} \int_0^T I(V(t)) \cos(\omega t) dt = \int_{-V_1}^{V_1} I(V_0 + \nu) \frac{\nu d\nu / (\pi V_1)}{\sqrt{V_1^2 - \nu^2}} = \int_{-V_1}^{V_1} I'(V_0 + \nu) \frac{\sqrt{V_1^2 - \nu^2}}{\pi V_1} d\nu \quad (2.6)$$

This means that the true differential conductance $I'(V_0)$ is convolved with the semicircular broadening function specified above.

2.1.4 Technical Challenges

The technique of STM inherently poses several challenges. Firstly, to measure features on the order of $O(100 \text{ pm})$, the vibrations need to be sufficiently low. More precisely, current state-of-the-art laboratories are built to achieve RMS velocities below 1 nm/s [30]. This requires multi-stage vibration strategies including passive dampers such as concrete blocks, air cushions and springs, as well as active dampers. Secondly, a sharp tip leads to high electric fields which could ionize any nitrogen/oxygen molecules. This means that some insulating medium must be chosen, which is usually ultra-high vacuum (UHV). Apart from that, UHV opens the possibility to prepare and keep atomically clean surfaces. Finally, to measure currents on the order of $O(10 \text{ pA})$, high amplification and a low noise environment are required.

Once these requirements are met, STM opens the possibility to study a plethora of physical phenomena at the atomic scale. The next section presents some highlights of these recent developments.

2.2 Recent Advances in Scanning Tunneling Microscopy

Since its invention, the technique of STM has seen several improvements and extensions. If one considers the basic setup in figure 2.2, each of the components can be modified. Figure 2.4

presents some main extensions.

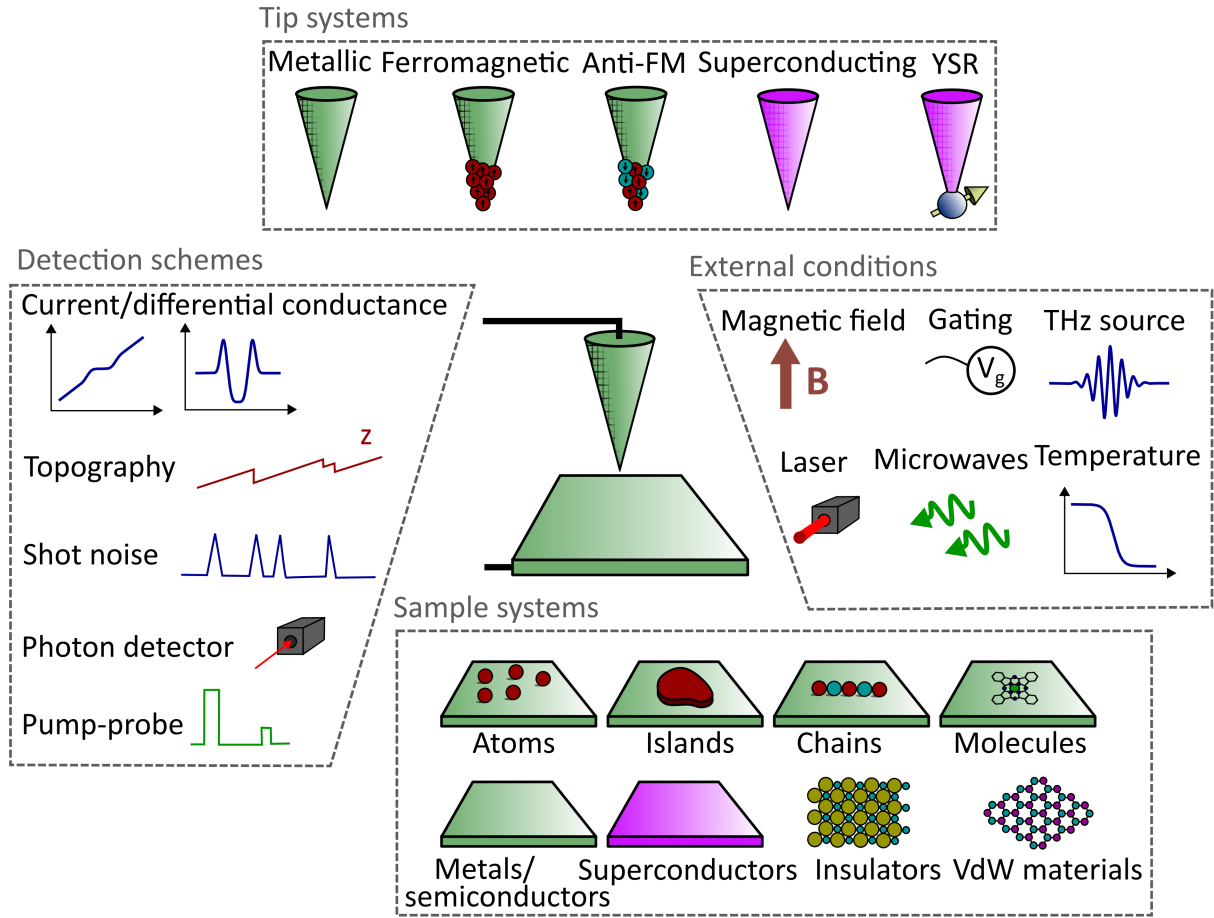


Figure 2.4: Schematic of the different variations in STM. Examples of different sample systems, tip systems, external conditions and detection schemes are shown.

Firstly, the question is: what systems can we study? The first STM image was taken on the semiconductor silicon [5] and most work is carried out on clean metal surfaces [31]. With the advent of better preparation techniques, the deposition of molecules, islands, atoms or insulators is possible, each of which has enabled new routes of investigation. Firstly, the ability to manipulate single atoms allows STMs to engineer structures atom by atom, with the most famous example being the quantum corral [6]. Islands are closely related to proximity effects. For example, it is speculated that monolayers of CrBr_3 on NbSe_2 might host so-called Majorana bound states at the edge [32]. Molecules on conductors [33] enabled the study of the Kondo effect [34] which arises from the interaction of magnetic moments with conduction electrons. Even larger molecules like glycans can also be imaged with STM [35] combined with more sophisticated deposition techniques. Lastly, insulators such as NaCl [36] or MgO [37] help to study charging processes or can reduce the decoherence due to electrons from the substrate.

The other part of the tunnel junction, i.e. the tip, can also be changed to study new phenomena.

Ferromagnetic tips are spin-polarized, opening the possibility to investigate magnetic and spin properties of the sample, such as skyrmions [38]. To measure spin properties in the zero-field limit, antiferromagnetic tips such as MnNi [39] are useful. Apart from that, superconducting tips enable the study of numerous effects related to superconductivity, such as Andreev reflections [40] or the Tedrow-Meservey effect [41, 42]. Finally, several functionalizations of tips are possible, for example with Yu-Shiba-Rusinov states [43] or with ESR sensitive apices [44].

With a given set of tip and sample system, various physical or chemical properties can be analyzed. The most conventional tools are topographic maps, where the surface is rastered in constant current or constant height mode. Yet already these can be used to gain structural information, for example to study the effect of a hydrogen evolution reaction in the presence of polymers on Au(111) [45]. Another key tool for STM is the measurement of differential conductance (dI/dV). This can give information about the density of states. In combination with rastering, the so-called grid spectroscopy can be used to map the spatial extent of spectroscopic features as for example edge modes [46]. Not only the signal itself, but also the noise can give information about the underlying processes. For instance, the quantization of charge carriers leads to Poissonian noise at small current, so-called shot noise [47]. This has been used to extract the number of charge carriers involved in one tunneling event [48]. Another experiment where noise can be useful is stochastic resonance [49]. Here, the way in which the system synchronizes with the external drive can give information about its dynamic properties. Apart from electronic properties, photonic properties like luminescence [50] have been explored using photon detectors. This has led to advances in the study of excitons [51], which are electron-hole bound states in a solid state material. Pump probe schemes have opened the avenue towards switching of magnets [52] and measuring the lifetime of systems directly [53].

Finally, one can vary the external conditions to drive the system and study its behaviour. For example, magnetic fields induce a Zeeman splitting which can be measured in the dI/dV [42]. Temperature is usually a source of decoherence. Therefore temperature-dependent measurements can help with studying phenomena which are sensitive to temperature such as the Kondo effect [54]. Fast signals can be used to study the dynamics of systems. With THz sources, it is possible to study dynamics on the picosecond time scale [55, 56]. Recently, optical pulses enabled sub-femtosecond resolution in STM measurements [57], thereby making it possible to track electron motion in molecules [58]. Finally, microwaves are a tool to excite systems such as for example single TiH molecules in ESR-STM [44].

The list of available methods and systems is steadily growing, making STM a key technique for understanding phenomena at the atomic scale – ranging from fields such as superconductivity to biomolecules.

2.3 Green's Functions and the Tunneling Current

Bradeen's formula (equation 2.4) is a good first approximation to calculate the tunneling current. However, in several cases, an extension of this formula is needed to model the experimental data. In particular for many-body phenomena, Green's functions turn out to be more useful. Therefore, this chapter presents a short overview of the Green's function treatment of tunneling. If treated rigorously, the problem of tunneling becomes mathematically challenging as we are dealing with a non-equilibrium situation where current is flowing from one electrode to the other at finite temperatures. This includes Green's functions and the Keldysh formalism [59]. As Green's functions are an essential tool for understanding the theory of YSR states, this chapter focuses on Green's functions while leaving the Keldysh formalism as bonus reading. This section largely follows the derivation presented by Cuevas and Scheer [60].

Consider a system where two electrodes are coupled by a hopping t . The Hamiltonian then reads:

$$H = H_L + H_R + \sum_{\sigma} t c_{L\sigma}^{\dagger} c_{R\sigma} + \text{h.c.} \quad (2.7)$$

Now the time-dependent current is simply the change in charge on one of the electrodes:

$$I(\tau) = -e \frac{d}{d\tau} \sum_{\sigma} \langle c_{R\sigma}^{\dagger}(\tau) c_{R\sigma}(\tau) \rangle \quad (2.8)$$

We wish to calculate the expectation value of the current and can use Ehrenfest's theorem: $\frac{d}{d\tau} \langle A \rangle = \frac{1}{i\hbar} \langle [A, H] \rangle + \langle \frac{\partial A}{\partial \tau} \rangle$. This gives the general expression for the current because $\langle \frac{\partial A}{\partial \tau} \rangle = 0$ in the steady state:

$$I(\tau) = \frac{ie}{\hbar} \langle [c_{R\sigma}^{\dagger}(\tau) c_{R\sigma}(\tau), H] \rangle = -\frac{ie}{\hbar} \langle t c_{L\sigma}^{\dagger}(\tau) c_{R\sigma}(\tau) - \text{h.c.} \rangle \quad (2.9)$$

At this point, it is useful to draw a connection to Green's functions. The Green's function is defined as the propagator of the Schrödinger equation (where a small imaginary part has been added to the energy to choose the contour):

$$[E \pm i\eta - H(x)] G^{r,a}(x - x') = \delta(x - x') \quad (2.10)$$

By Fourier-transforming, one obtains:

$$G^{r,a}(E) = [E \pm i\eta - H]^{-1} \quad (2.11)$$

Now this Green's function seems like a complicated mathematical construct, but it captures the underlying physics of the system. This is because it is the response of the system to a perturbation in terms of a δ -function, thereby covering all possible responses. One important physical property of the Green's function can be derived from the identity $\frac{1}{E \pm i\eta} = P(1/E) \mp \delta(E)$, where P denotes the principal value. This leads to the density of states:

$$\rho(E) = -\frac{1}{\pi} \text{Im}(G^r(E)) \quad (2.12)$$

By assuming that the tunneling term H_T is a perturbation, one finds Dyson's equation:

$$G^{r,a}(E) = g^{r,a}(E) + g^{r,a}(E) H_T G^{r,a}(E) \quad (2.13)$$

where $g^{r,a}(E) = [E \pm i\eta - (H_L + H_R)]^{-1}$ is the unperturbed Green's function and the term H_T can be generalized to the self-energy Σ . Now usually one knows the left and right Green's function and wishes to avoid a Green's function describing the whole system. Therefore it is customary to project onto the levels of the left (right) electrode, for example by saying: $G_{LR} = \langle L|G|R \rangle$

This can now be related to tunneling current in the following way. In the Keldysh formalism, one can define [60]:

$$G_{LR}^{+-}(\tau, \tau') = i \langle c_{L\sigma}^\dagger(\tau) c_{R\sigma}(\tau') \rangle \quad (2.14)$$

From this expression, we see immediately that Green's functions and the tunneling current are closely linked. We can write:

$$I = \frac{4\pi t}{\hbar} \int_{-\infty}^{\infty} dE [G_{RL}^{+-}(E) - G_{LR}^{+-}(E)] \quad (2.15)$$

Additionally, the recursive nature of Dyson's equation means that the current has different contributions of increasing order in the tunneling t , which correspond to higher order tunneling processes. Now the non-equilibrium Green's function includes the Fermi function: $G_{LR}^{+-}(E) = [G_{LR}^a(E) - G_{LR}^r(E)] f(E)$.

2.4 Electronic transport in STM

In STM, like in other non-equilibrium experiments, electrons are transferred from one electrode through a barrier into another electrode. This means that many results from electronic transport theory become relevant to STM.

Consider a similar situation as in subsection 2.1.3, where there is a left and a right electrode. If these electrodes are now connected by one transport channel, then the current is the product of the number of charges with their velocity times the transmission probability [61]:

$$I = nevT = \int [f(E + eV) - f(E)] N(E) v(E) T(E) dE \quad (2.16)$$

Here $N(E)$ is density of states per unit length, i.e. $L \int N(E) dE = 2 \frac{k}{2\pi/L}$ such that $N(E) = \frac{1}{\pi} \frac{\partial k}{\partial E}$. Now the velocity is also $v(E) = \frac{1}{\hbar} \frac{\partial E}{\partial k}$, so that we find for the current:

$$I = \int (f(E + eV) - f(E)) \frac{e}{\pi \hbar} T(E) dE \quad (2.17)$$

For small temperatures, the difference in Fermi functions is just a rectangle of width eV . This gives the famous Landauer formula for the conductance G , where we have replaced T by a sum

over transmission channels T_i :

$$G = \frac{2e^2}{h} \sum_i T_i \quad (2.18)$$

The key interpretation is that there is a quantum of conductance $G_0 = \frac{2e^2}{h}$ for each transport channel. This is also relevant for STM to quantify how close the tip is to the sample. Instead of specifying a setpoint current, it is often more helpful to convert this into the transparency/transmission τ which measures the ratio of the experimental conductance (in the normal state for superconductors, i.e., at voltages greater than the gap, $|eV| \gg 2\Delta$) to the quantum of conductance:

$$G_N = \tau G_0 \quad (2.19)$$

The quantization of charge leads to so-called shot noise. To understand the origin of shot noise, consider a derivation based on transmission through a barrier [47]. Considering the forward current of one channel with one spin species with occupation probability f , the net forward expectation value is $\langle n_{\text{fwd}} \rangle = fT$. Now, the occupation can be zero or one, resulting in $\langle n_{\text{fwd}}^2 \rangle fT$. Therefore, we find for the variance of the occupation number:

$$\langle (n_{\text{fwd}} - \langle n_{\text{fwd}} \rangle)^2 \rangle = fT(1 - fT) \quad (2.20)$$

Integrating over the energy, this gives the noise in terms of the Fermi function:

$$S_{\text{fwd}} = 2 \frac{G_0}{2} \int T f(E) [1 - f(E)] dE \quad (2.21)$$

Using equation 2.17, one finds Schottky's result for the noise in the regime where $T \ll 1$:

$$S_{\text{fwd}} = 2e \langle I_{\text{fwd}} \rangle \quad (2.22)$$

It should be noted that the noise at higher transmission becomes sub-poissonian due to the correction term in equation 2.21. This deviation from the Poissonian value is called the Fano factor which is defined as:

$$F = \frac{S}{2e \langle I \rangle} \quad (2.23)$$

The shot noise is strongly sensitive to the number of charge carriers involved in the tunneling process. Therefore, a generalization of equation 2.21 in the context of Andreev reflections (see section 2.10) is [62]:

$$S = 2G_0 \int dE \left[\sum_{n=1}^{\infty} n^2 R_n - \left(\sum_{n=1}^{\infty} n R_n \right)^2 \right] \quad (2.24)$$

Here n is the number of times a quasiparticle crosses a barrier and R_n is the probability for such a process. Depending on which processes are allowed, this equation predicts the formation of steps in the shot noise as a function of bias voltage across a superconductor-superconductor junction.

2.5 Superconductivity

2.5.1 Macroscopic Description

In some materials, the resistivity drops to zero below a certain temperature (the critical temperature T_C). This phenomenon is called superconductivity. Superconductors are perfect diamagnets which means that they expel magnetic fields such that the magnetic field inside a superconductor is always zero, i.e. $\mathbf{B} = 0$. This phenomenon is called the Meissner effect. The superconducting phase transition can be understood in terms of a phenomenological approach, namely the Landau expansion of the free energy in terms of an order parameter:

$$f = \alpha|\psi|^2 + \frac{1}{2}\beta|\psi|^4 \quad (2.25)$$

Now as α changes sign, the minimum of the free energy changes from $\psi = 0$ to $|\psi| = \sqrt{-\alpha/\beta}$. While this model can be applied to several different phase transitions, in the context of superconductivity, ψ would be the wavefunction of the superconducting condensate, α is a temperature-dependent parameter, $\alpha = \alpha_0(T - T_C)$ and β is a constant. An extension including the magnetic field is the Ginzburg-Landau theory. The free energy is [63]:

$$f = \alpha|\psi|^2 + \frac{1}{2}\beta|\psi|^4 + \frac{1}{2m^*}|(-i\hbar\nabla - 2e\mathbf{A})\psi|^2 + \frac{1}{2\mu_0}B^2 \quad (2.26)$$

Here \mathbf{A} is the magnetic vector potential and \mathbf{B} the magnetic field. Now there are two parameters which can be measured experimentally: the coherence length ξ and the penetration depth λ . These relate to the parameters α and β in the following way:

$$\xi = \sqrt{\frac{\hbar^2}{4m^*|\alpha|}} \quad (2.27)$$

$$\lambda = \sqrt{\frac{m^*\beta}{4\mu_0 e^2 |\alpha|}} \quad (2.28)$$

Here the coherence length is a natural decay length of the wavefunction ψ and the penetration depth is the natural length of the magnetic vector potential. The ratio $\kappa = \lambda/\xi$ is a criterion to distinguish between type-I ($\kappa < 1/\sqrt{2}$) and type-II ($\kappa > 1/\sqrt{2}$) superconductors. While type-I superconductors lose superconductivity globally when a magnetic field is applied, type-II superconductors form normal conducting vortices [64].

2.5.2 Microscopic Description

These macroscopic properties can be understood in terms of the formation of Cooper pairs. Normally, electrons experience a Coulomb repulsion, but phonons can cause electrons to pair up.

The mathematical microscopic description is BCS theory [65]. By assuming a phonon-mediated attractive potential, one arrives at:

$$H = \sum_{\mathbf{k}\sigma} \xi_{\mathbf{k}} c_{\mathbf{k}\sigma}^\dagger c_{\mathbf{k}\sigma} + \frac{1}{N} \sum_{\mathbf{k}\mathbf{k}'\sigma\sigma'} V_{\mathbf{k}\mathbf{k}'} c_{\mathbf{k}\uparrow}^\dagger c_{-\mathbf{k}\downarrow}^\dagger c_{-\mathbf{k}'\downarrow} c_{\mathbf{k}'\uparrow} \quad (2.29)$$

By introducing a gap parameter $\Delta_{\mathbf{k}} = -\frac{1}{N} \sum_{\mathbf{k}'} V_{\mathbf{k}\mathbf{k}'} \langle c_{-\mathbf{k}'\downarrow} c_{\mathbf{k}\uparrow} \rangle$, one can find the mean field Hamiltonian:

$$H = \sum_{\mathbf{k}\sigma} \xi_{\mathbf{k}} c_{\mathbf{k}\sigma}^\dagger c_{\mathbf{k}\sigma} + \sum_{\mathbf{k}} \left(\Delta_{\mathbf{k}} c_{\mathbf{k}\uparrow}^\dagger c_{-\mathbf{k}\downarrow}^\dagger + \text{h.c.} \right) \quad (2.30)$$

This Hamiltonian can be written in terms of a Nambu basis $\Psi_{\mathbf{k}} = \left(c_{\mathbf{k}\uparrow}, c_{-\mathbf{k}\downarrow}^\dagger \right)^T$:

$$H = \sum_{\mathbf{k}} \Psi_{\mathbf{k}}^\dagger \begin{pmatrix} \xi_{\mathbf{k}} & \Delta_{\mathbf{k}} \\ \Delta_{\mathbf{k}}^* & -\xi_{\mathbf{k}} \end{pmatrix} \Psi_{\mathbf{k}} \quad (2.31)$$

This Hamiltonian is diagonalized by a superposition of electrons and holes, the so-called Bogoliubov quasiparticles with energy $E = \sqrt{\xi_{\mathbf{k}}^2 - |\Delta_{\mathbf{k}}|^2}$. The quasiparticles are superpositions of holes and electrons, i.e.:

$$c_{\mathbf{k}\uparrow} = u_{\mathbf{k}}^* \gamma_{\mathbf{k}\uparrow} + v_{\mathbf{k}} \gamma_{-\mathbf{k}\downarrow}^\dagger \quad (2.32)$$

$$c_{-\mathbf{k}\downarrow}^\dagger = u_{\mathbf{k}} \gamma_{-\mathbf{k}\downarrow}^\dagger - v_{\mathbf{k}}^* \gamma_{\mathbf{k}\uparrow} \quad (2.33)$$

Here the factors $u_{\mathbf{k}}$ and $v_{\mathbf{k}}$ satisfy the condition $|u_{\mathbf{k}}|^2 + |v_{\mathbf{k}}|^2 = 1$ such that $\gamma_{\mathbf{k}\uparrow}$ are still fermionic particles.

The Green's function of a BCS superconductor can be written in the Nambu basis:

$$G_{\mathbf{k}}^{r,a}(E) = \frac{1}{(E \pm i\eta)^2 - \xi_{\mathbf{k}}^2 - |\Delta_{\mathbf{k}}|^2} \begin{pmatrix} E + \xi_{\mathbf{k}} & \Delta_{\mathbf{k}}^* \\ \Delta_{\mathbf{k}} & E - \xi_{\mathbf{k}} \end{pmatrix} \quad (2.34)$$

Summing over momentum states $\frac{NL^3}{(2\pi)^3} \int d\mathbf{k}^3$, using the residue theorem and assuming that Δ is constant, we find the Green's function in terms of the normal density of states ρ_0 :

$$G^{r,a}(E) = \frac{-\pi\rho_0}{\sqrt{\Delta^2 - E^2}} \begin{pmatrix} E & \Delta \\ \Delta & E \end{pmatrix} \quad (2.35)$$

With the knowledge of the previous section, the density of states is just the imaginary part of the Green's function, giving both electron and hole density of states at positive and negative energies, as expected. Sometimes a broadening parameter η is introduced to account for finite lifetimes of quasiparticles [66]. The new equation for the density of states reads:

$$\rho(E) = \rho_0 \text{Re} \left[\frac{E + i\eta}{\sqrt{(E + i\eta)^2 - \Delta^2}} \right] \quad (2.36)$$

A key result of BCS theory is a prediction for the critical temperature [24]:

$$\Delta = 1.76 k_B T_C \quad (2.37)$$

While this formula gives an accurate estimate for some elemental superconductors, it does not have predictive power for more complicated superconducting materials such as compounds.

Figure 2.5(a) shows the density of states for different values of η . For higher η , the coherence peaks become smaller and the gap is more filled. Panel (b) shows the effect of changing the superconducting gap Δ at constant η .

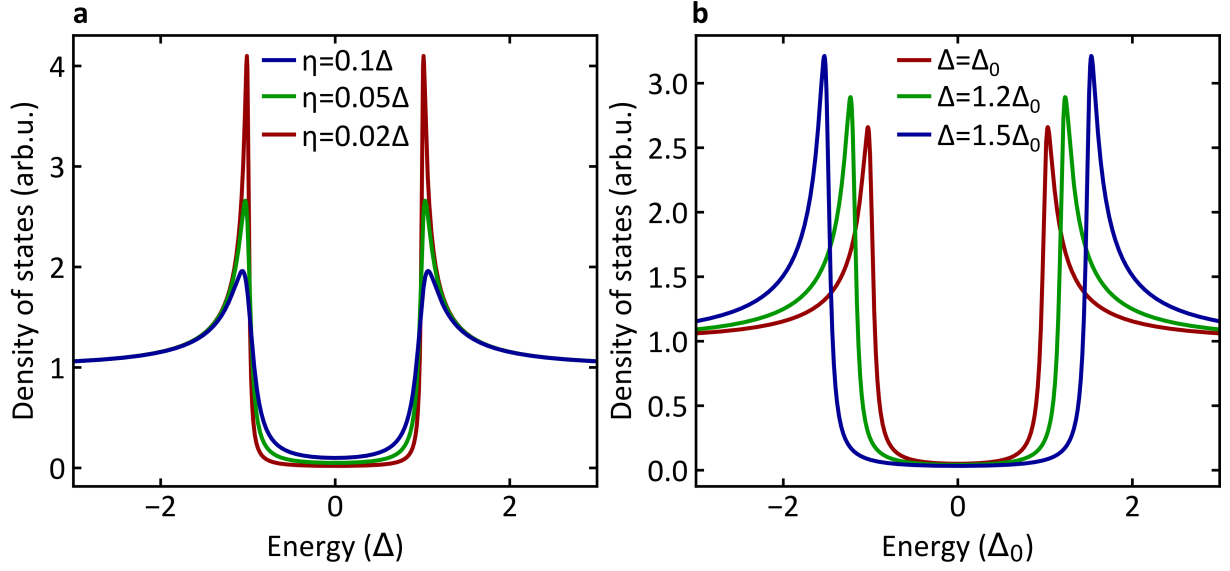


Figure 2.5: Plots of the BCS density of states. (a) Density of states at different values of η . (b) Density of states at different values of Δ where $\eta = 0.05\Delta_0$.

To model the tunneling between two superconductors at lowest order, we can resort to Equation 2.4. Figure 2.6(a) shows the current dependence of a superconductor-superconductor junction at different temperatures. Both sides of the tunnel junction are gapped, such that there is no current for $|eV| < 2\Delta$ at zero temperatures. At finite temperatures, there are thermally excited quasiparticles, leading to a small current within the gap which is suppressed by a Boltzmann factor $e^{-\Delta/k_B T}$. Panel (b) shows the corresponding differential conductance. The coherence peaks at $\pm 2\Delta/e$ which become sharper at lower temperature are a characteristic feature of SIS junctions in STM. Again, the peak at zero bias voltage is due to thermal excitations.

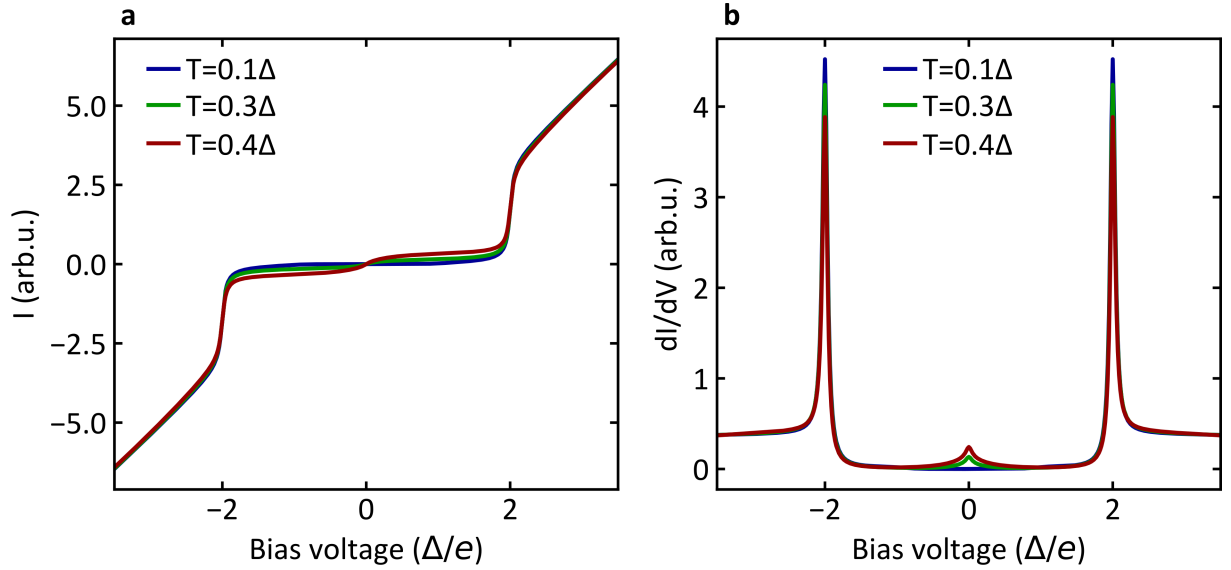


Figure 2.6: dI/dV of superconductor-superconductor tunneling. (a) Lowest order superconductor- superconductor tunneling current for $\eta = 0.02\Delta$ at variable temperature. (b) Differential conductance at the same conditions.

There are different types of superconductors in practice. In the previous subsection, we have already distinguished between type-I and type-II superconductors. Other classes of superconductors, as for example cuprates [67], iron based superconductors [68] or heavy fermion superconductors [69] cannot be described by BCS theory and often the crystal structure leads to some anisotropy in the superconducting properties. Superconductors where Δ is not constant (e.g. d -wave superconductors [70]) do not show the characteristic gap in STM measurements. Integrating over different values of $\Delta(\mathbf{k}) \propto \cos(k_x) - \cos(k_y)$ means that there is no zero-current region as in the case of s -wave superconductors. This has been observed experimentally on BSCCO for example [71].

Electrons are fermionic which means that the overall wavefunction $\Psi = \Psi_{\text{spin}} \Psi_{\text{space}}$ must have odd parity. For conventional singlet-pairing Ψ_{spin} is odd, such that Ψ_{space} must be even. This would imply that p -wave superconductors are forbidden. Under special circumstances, Cooper pairs form triplets, resulting in so-called p -wave superconductors [72].

2.6 Yu-Shiba-Rusinov States

2.6.1 Basic Theory of YSR States

Shiba-Kondo Model

It is well known that magnetic fields can quench superconductivity globally. This raises the question how a magnetic impurity placed on a superconductor will interact with the surrounding Cooper pairs and possibly break them. Here, we focus on impurities on s -wave superconductors. This problem was first addressed by Yu, Shiba and Rusinov [73–75]. The starting point for the study of an impurity on a superconductor is the inclusion of an interaction between a superconductor and the impurity due to potential scattering (spin independent) of strength $V\delta(\mathbf{r})$ and exchange scattering $JS\sigma_z\delta(\mathbf{r})$ [74, 76]:

$$H_{\text{imp}} = \sum_{\sigma} (V - JS\sigma) c_{R\sigma}^{\dagger} c_{R\sigma} \quad (2.38)$$

With the normal density of states ρ_0 , one can introduce the parameters:

$$\alpha = \pi\rho_0 JS \quad (2.39)$$

$$\beta = \pi\rho_0 V \quad (2.40)$$

Here α measures the coupling to the substrate and does not break electron-hole symmetry. The parameter β makes the electron and hole part of the resulting Green's function different. Based on Dyson's equation, the following formula can be derived for the energy of the YSR bound state [76]:

$$\epsilon = \Delta \frac{1 - \alpha^2 - \beta^2}{\sqrt{(1 - \alpha^2 + \beta^2) + 4\alpha^2}} \quad (2.41)$$

This reduces to $\epsilon = \Delta \frac{1 - \alpha^2}{1 + \alpha^2}$ for the case of $\beta = 0$.

Anderson Impurity Model

Another related model is the Anderson Impurity Model [77]. It assumes that the localized energy state which has excitations of energy ϵ_d and a Coulomb repulsion of strength U , giving the Hamiltonian:

$$H = H_{\text{BCS}} + H_{\text{imp}} + H_{\text{hop}} \quad (2.42)$$

Here, H_{BCS} is the Hamiltonian of the superconducting substrate, coupled to the impurity by $H_{\text{hop}} = \sum_{dk} V_{dk} c_{k\sigma}^{\dagger} c_{d\sigma} + \text{h.c.}$, where $c_{k\sigma}^{\dagger}$ creates an electron in the substrate and $c_{d\sigma}^{\dagger}$ creates one in the impurity. The impurity itself has the Hamiltonian:

$$H_{\text{imp}} = \sum_{\sigma} \epsilon_{d\sigma} c_{d\sigma}^{\dagger} c_{d\sigma} + U n_{d\uparrow} n_{d\downarrow} \quad (2.43)$$

A full solution requires a numerical renormalization group approach [78, 79]. However, in certain limits, an analytical solution is possible, giving insight into the underlying physics. One common approximation is the mean-field approach with $U = \epsilon_d + \frac{U_d}{2} (\langle n_{d\uparrow} \rangle + \langle n_{d\downarrow} \rangle)$.

Next, one has to consider an exchange interaction J , allowing us to rewrite the Hamiltonian as [80]:

$$H_{\text{imp}} = U(n_{\uparrow} + n_{\downarrow}) + J(n_{\uparrow} - n_{\downarrow}) \quad (2.44)$$

At this point, the combination of superconductivity and spin-dependent scattering results in 4×4 matrices. If we use σ_i as the Pauli matrices in spin space and τ_j as the Pauli matrices in electron-hole space, we can re-write the Hamiltonian as:

$$H_{\text{imp}} = U(\sigma_0 \otimes \tau_3) + J(\sigma_3 \otimes \tau_0) \quad (2.45)$$

To calculate the Green's function of the impurity dressed with the superconductor, the starting point is Dyson's equation, equation 2.13, where we use i and S as indices for the impurity and the substrate, respectively:

$$G_{ii} = g_{ii} + g_{ii} H_{\text{hop}} G_{Si} \quad (2.46)$$

$$G_{Si} = g_{SS} H_{\text{hop}} G_{ii} \quad (2.47)$$

This gives:

$$G_{ii} = (1 - |t_S|^2 g_{ii} g_{SS})^{-1} g_{ii} \quad (2.48)$$

where t_S is the hopping in H_{hop} which can be expressed as a rate Γ_S using the substrate density of states n_S such that $\Gamma_S = |t_S|^2 n_S$. Now all the other parts of the total Hamiltonian are spin-symmetric, which means that the spin part of the Green's function is diagonal. Finally, the Green's function is [81]:

$$G(E) = \frac{\Gamma_S E \sigma_0 + ((E - J) \sigma_0 + U \sigma_3) \sqrt{\Delta^2 - E^2} + \Gamma_S \Delta \sigma_1}{((E - J)^2 - U^2 - \Gamma_S^2) \sqrt{\Delta^2 - E^2} + 2J\Gamma_S E} \quad (2.49)$$

From this, the density of states can be calculated using equation. Moreover, the energy of the YSR peak can be determined from the divergence of the denominator in the Green's function. In the regime where $E \ll J, \Gamma_S$, one finds [80]:

$$\epsilon = \pm \Delta \frac{J^2 - U^2 - \Gamma_S^2}{\sqrt{(\Gamma_S^2 + (J - U)^2)(\Gamma_S^2 + (J + U)^2)}} \quad (2.50)$$

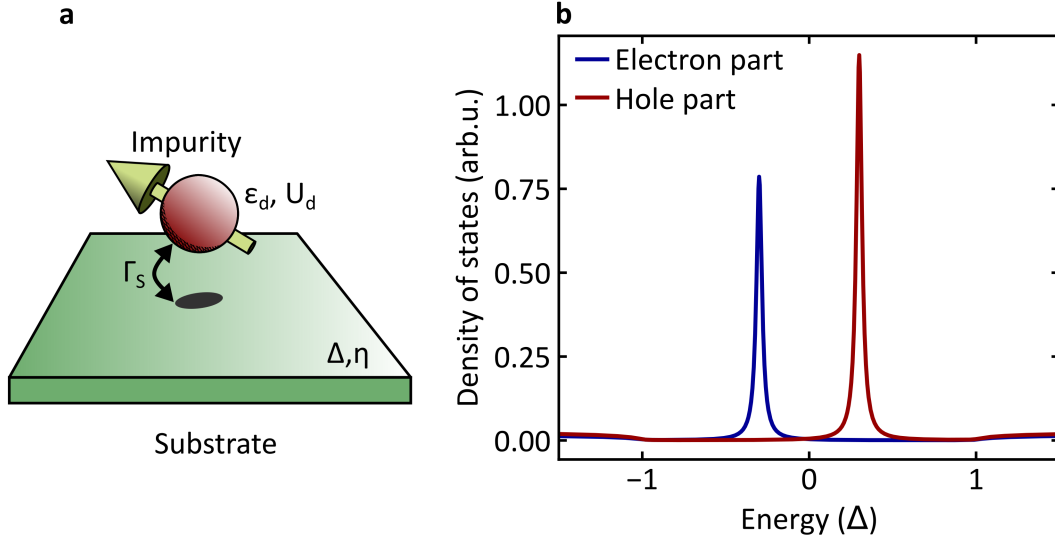


Figure 2.7: Schematic of the Anderson Impurity Model. (a) Schematic of the mathematical terms. (b) Calculated density of states with (parameters in meV) $\Delta = 1, \eta = 0.02, \Gamma_S = 100, J = 75, U = 20$.

Figure 2.7(a) shows a schematic of the terms involved in the Anderson impurity model. Panel (b) shows the electron and hole parts of the density of states for the parameters specified in the caption. The two peaks corresponding to the YSR states are the most prominent feature. Outside the gap, $|eV| > \Delta$, there is a non-zero density of states as expected for a superconducting substrate. However, the BCS peaks are suppressed due to the presence of the YSR state.

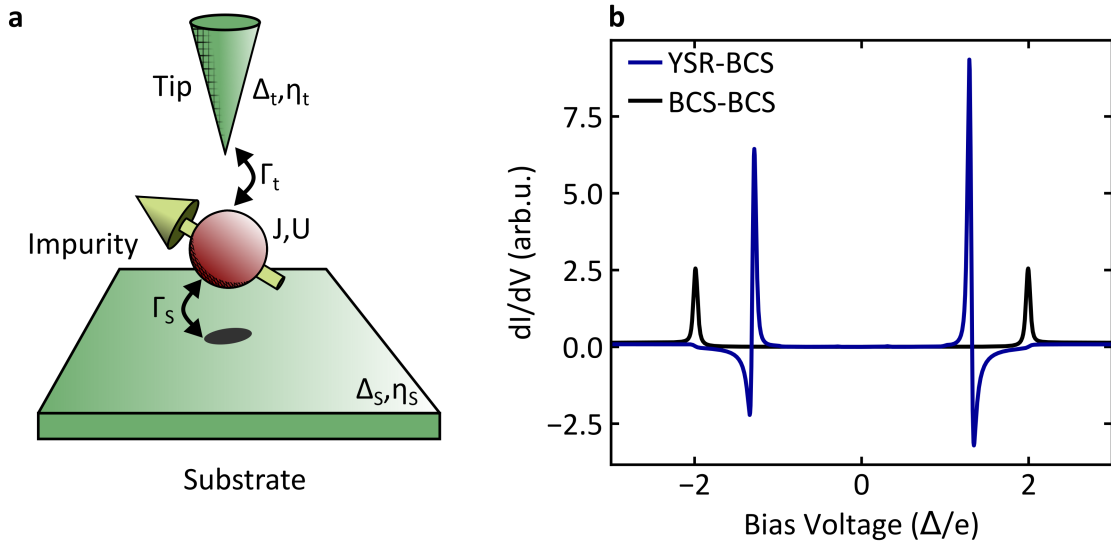


Figure 2.8: Calculated dI/dV of BCS-YSR tunneling. (a) Schematic of the mathematical terms. (b) Calculated dI/dV with (parameters in meV) $\Delta = 1, \eta = 0.02, \Gamma_S = 100, J = 75, U = 20$.

In this work, YSR states are probed using a superconducting tip. This means that the peaks at

energy ϵ are located at positions $\pm(\Delta_S + \epsilon)$ in the dI/dV spectrum. The peaks are a convolution of the BCS density of states with the YSR density of states which means that the shape of the peak is largely determined by the (usually broader) BCS state in the tip. To model a YSR state on the tip, we simply change the parameters Γ_t and Γ_s as shown in Figure 2.8(a) which shows the junction and the parameters. If $\Gamma_t \gg \Gamma_s$, this would imply that the impurity is on the tip and vice versa for an impurity on the sample. Panel (b) shows the resulting dI/dV spectrum calculated with the Anderson impurity model. As in the case of superconductor-superconductor tunneling, there are thermal peaks at non-zero temperature. The spectral weight of these YSR states is suppressed by a Boltzmann factor $e^{-\epsilon/(k_B T)}$. Particularly for low energy YSR states, this thermal contribution can be significant. It should be noted that the asymmetry of the thermal states is flipped with respect to the ground states. Figure 2.9(a) shows this result which has already been reported in the literature [76]. The normal electron peak (at positive bias voltage, labelled e_n) is higher which means that its thermal counterpart e_t appears at negative bias voltage. Likewise, the smaller hole peak h_n leads to an even smaller thermal hole peak h_t at positive bias voltage. As shown in panel (b), this effect becomes more pronounced with higher temperature.

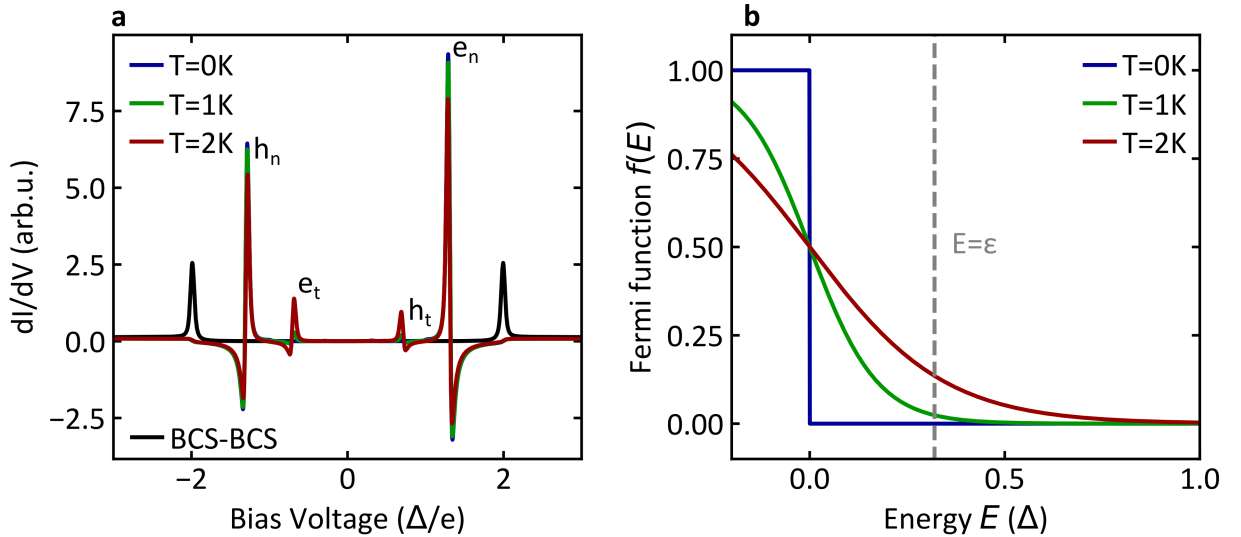


Figure 2.9: Calculated temperature-dependent YSR-BCS spectra. (a) dI/dV spectra at different temperatures. (b) Calculated Fermi function at these temperatures. The parameters are (in meV): $\Delta = 1$, $\eta = 0.01$, $\Gamma_S = 100$, $J = 75$, $U = 20$.

For real YSR states, there is usually a superposition of the BCS channels with a YSR channel. This superposition of channels is considered in Chapter 5.

2.6.2 Relation of YSR states to Quantum dots

Quantum dots (QD) are systems where a gate constricts the charge in a region such that there are single electron levels [82]. This means that QD operate in a regime which is very similar to STM. In addition to that, both QD and YSR states host isolated single levels. This means that a good understanding of QD physics can be beneficial for experiments on YSR states. In practice, quantum dots are created by confining electrons to a narrow region, for example using GaAs/AlGaAs heterostructures [83].

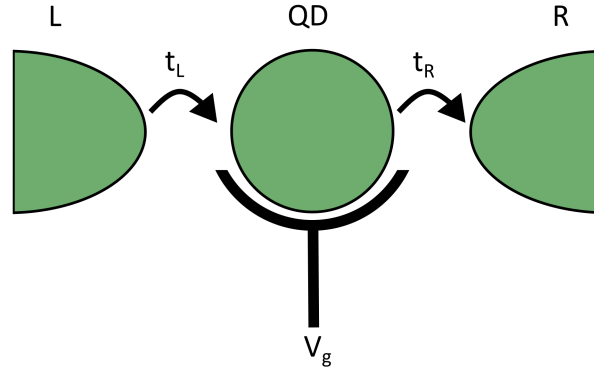


Figure 2.10: Schematic of a quantum dot. The dot is placed between two electrodes such that electrons can tunnel across the dot.

Figure 2.10 shows the basic design of a quantum dot. There are two electrodes which are coupled to the quantum dot region. The Fermi level of the dot region can be controlled with a gate voltage V_g . Now if one electron tries to travel across the dot, it experiences a Coulomb repulsion which has to be overcome. If the charging energy is large compared to the thermal energy, $E_C = \frac{e^2}{2C} \gg k_B T$, then the conductance will show peaks as a function of gate voltage each time the occupation of the dot changes from N to $N + 1$. This effect is called the Coulomb blockade [84]. To draw a connection to STM, charging effects are also relevant here. However, there is no Coulomb blockade in the conventional sense because of phase fluctuations [85]. This is called dynamical Coulomb blockade. Apart from that, the observation of a $0 - \pi$ transition which has been observed in quantum dots [86], has recently also been seen in STM [87]. Moreover, while Figure 2.10 bears significant resemblance to the Anderson impurity model (see Figure 2.8), it should be noted that the regime where $t_L \sim t_R$ can easily be realised in quantum dots, whereas in STM, this is an extreme scenario where the tip is almost in point contact with the sample. Finally, ideas such as Cooper pair splitting [88] or spin qubits [89, 90] could inspire experiments conducted with YSR states. Overall quantum dots and YSR states in STM can be used to study very similar phenomena and the two fields are closely linked.

2.6.3 Recent Experiments on YSR States

In the context of STM, there are two methods of inducing YSR states: one is by depositing atoms/molecules on a superconductor and the other is using intrinsic impurities themselves. Table 2.1 shows a non-exhaustive list of different sample systems which have been investigated.

Table 2.1: List of systems showing YSR states in STM measurements. We list the substrate and the adatom species.

Substrate	Source of YSR states	Reference
Nb(110)	Mn,Gd,Cr,Fe,Co,V	[91–93]
Pb(111)	Mn,FeP,MnPc	[76, 94–96]
Pb(110)	Fe	[97]
Pb on Si(111)	Mn,Cr	[98]
V(100)	intrinsic	[43, 99]
FeTe _{0.55} Se _{0.45}	Fe	[100]
NbSe ₂	CoPc,MnPc	[46, 101]
NbSe ₂	intrinsic due to Fe doping	[102]
β Bi ₂ Pd	Cr	[103]
Bi on Nb(110)	Gd	[104]
Ta(100)	Fe	[105, 106]
Re(0001)	Fe,Mn,Co	[107]

With this long list of candidate systems, various properties of YSR states have been studied. Firstly, it is important to study the coupling strength J , which has been done by analyzing the peak position of the YSR state relative to the size of the superconducting gap Δ [91]. Creating dimers by placing a second atom next to the adatom leads to variations in the YSR energy. This can either be done by changing the atom species [98] and/or the distance of the dimer atoms [104]. Another tuning parameter is the tip-sample distance. By tuning this distance and thus the atomic force exerted by the tip, the coupling can be varied. Then it is possible to explore the quantum phase transition between the screened and unscreened spin state [81, 94]. Figure 2.11 shows a schematic of the transition between the weak and strong coupling regime.

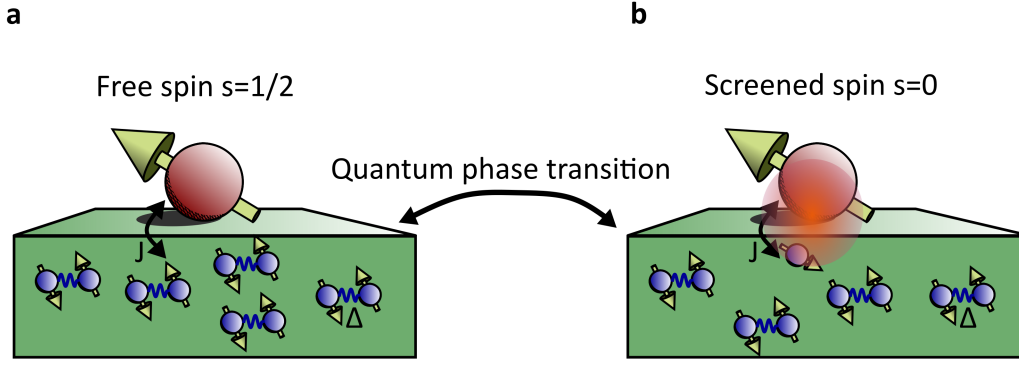


Figure 2.11: Schematic of a quantum phase transition of a YSR state. With increasing coupling J , the spin can be screened leading to a different parity in the ground state.

Other works have studied the tunneling regimes between superconductors and YSR states, i.e., how the tunneling processes into YSR states depend on conductance. There is a consensus about three regimes [43, 76]:

1. Linear regime
2. Sublinear regime
3. Andreev regime

In the linear regime, the tunneling rate is low such that the YSR state can always relax and the current scales with conductance [76]. In the sublinear regime, resonant Andreev processes are suppressed, but the tunneling rate is comparable to the relaxation rate of the YSR state such that the YSR state makes a bottleneck and the current scales sublinearly with conductance. This transition gives information about the lifetime of YSR states. Finally, at high enough conductances, resonant Andreev processes become relevant and lead to a superlinear dependence. For the case of YSR-YSR tunneling there are even more regimes and the extracted lifetime was estimated to be 48 ns for intrinsic impurities on V(100) at 10 mK [43].

These regimes immediately pose the question about how many charges are tunneling. This question has been tackled by a study of the shot noise [108], though an analysis is complex due to the simultaneous presence of Andreev reflections and quasiparticle tunneling.

Naturally, at higher conductances, the Josephson effect will become visible. The influence of YSR states on the Josephson effect is the subject of several investigations, providing information about the local variations of the order parameter [97] or the interference with the BCS channel across the quantum phase transition [87].

Another aspect of YSR states is their spin polarization. Spin polarized tips could be used to probe this feature and first attempts of doing so have been reported [100, 105]. Similarly, tips

functionalized with YSR states gave insight about the spin selection rules for tunneling between YSR states [99].

Exposing asymmetric YSR states to microwaves below 40 GHz [96] has lead to the observation of deviations from Tien-Gordon theory. This was explained in terms of different electron and hole parts in the tunneling processes involving the YSR state.

To summarize, currently the energy of YSR states and their conductance has been studied extensively. Other tools such as spin-polarized tips, atom manipulation or shot noise spectroscopy are in the development. Additionally, first indirect estimates of the lifetime of YSR states have been made [43, 76, 108]. These are yet to be confirmed by pump-probe schemes. While there are studies on the interaction of microwaves with YSR states, the coherent manipulation of YSR states is yet to be seen.

2.6.4 Majorana Bound States

One feature that distinguishes quantum computing from classical computing is the existence of entangled states such as $|\Psi\rangle = \frac{1}{\sqrt{2}}(|0\rangle + |1\rangle)$. Therefore it is important to discover systems that enable such entanglement operations. This is the main motivator for Majorana bound states. A Majorana fermion [109] is its own antiparticle, i.e. $\gamma = \gamma^\dagger$. This means that these particles could host a variety of interesting phenomena such as non-Abelian statistics [110]. In solid state physics, it has been speculated that chains on a p -wave superconductor could host similar Majorana modes [111]. The main difference to YSR states is that these Majorana bound states come in pairs (at both ends of a chain, for example) and give rise to zero-bias conductance peaks with their conductance quantized to $G_0 = \frac{2e^2}{h}$ [112]. While such zero-bias peaks have been reported in STM [113] as well as in nanowires [114], the demonstration of their topological properties has hitherto been elusive.

2.7 The Phase in Tunnel Junctions

This section is primarily based on the results presented by Ingold and Nazarov [115].

Going back to equation 2.7, we should introduce a phase parameter which accounts for the fact that the phases between the two electrodes might differ, i.e $t \rightarrow te^{i\phi}$. This accounts for the fact that the time-dependent wave functions on the left and right side may not be synchronized. For a normal conductor, one may define the phase difference in terms of the bias voltage $V(t)$ between the two electrodes:

$$\phi(t) = \frac{e}{\hbar} \int_{-\infty}^t V(\tau) d\tau \quad (2.51)$$

By considering a simple $L - C$ circuit, the energy $E = \frac{1}{2}CV^2 + \frac{1}{2}LI^2$ becomes:

$$H = \frac{Q^2}{2C} + \frac{\hbar^2}{2e^2L} (\phi - eVt/\hbar)^2 \quad (2.52)$$

In analogy to the simple harmonic oscillator $H = p^2/2m + kx^2/2m$, the charge and phase can be converted into operators and become conjugate variables:

$$[Q, \phi] = ie \quad (2.53)$$

This is sometimes referred to as second quantization or quantization of charge and it becomes particularly relevant in small junctions like quantum dots or STM. Now in general, the perfect LC circuit will experience some dissipation due to the environment, which dictates the behavior of the phase fluctuations. It is useful to define a $P(E)$ function which is the Fourier transform of these phase fluctuations $J(t) = \langle [\phi(t) - \phi(0)]\phi(0) \rangle$:

$$P(E) = \frac{1}{2\pi\hbar} \int_{-\infty}^{\infty} e^{J(t)+iEt/\hbar} dt \quad (2.54)$$

After some calculations, one finds that the basic tunneling formula 2.4 is modified by the inclusion of the $P(E)$ -function which introduces a broadening. The forward tunneling rate Γ_{\rightarrow} is then:

$$\Gamma_{\rightarrow}(V) = \frac{1}{e^2 R_T} \int_{-\infty}^{\infty} \int_{-\infty}^{\infty} f(E - eV) [1 - f(E')] \rho_L(E - eV) \rho_R(E') P(E - E') dE' dE \quad (2.55)$$

Here R_T is the tunneling resistance which can be rewritten in terms of the conductance as $R_T = (\tau G_0)^{-1}$. In the case of $k_B T \ll e^2/(2C)$, and no environmental impedance, the $P(E)$ -function is a δ -function and Equation 2.55 becomes Bardeen's formula.

This $P(E)$ function has various mathematical properties. For example, it satisfies the detailed balance:

$$P(-E) = e^{-E/(k_B T)} P(E) \quad (2.56)$$

This means that a particle tunneling across the junction is more likely to give energy to the environment than gaining energy from the environment. More precisely, it can only gain energy coming from thermal excitation of the environment. Furthermore, it is a probability density function, which means $\int_{-\infty}^{\infty} P(E) dE = 1$. Its expectation value is the charging energy, $\langle E \rangle = \frac{e^2}{2C}$. This means that on average, a particle loses this charging energy to the environment. Its physical interpretation is that it induces a broadening due to interaction with the environment. It becomes relevant in experimental setups where the instrumental noise has been reduced such that these effects becomes important.

The $P(E)$ approach is flexible because all possible environments (with total impedance $Z_T(\omega)$) can be encoded in the $P(E)$ function through $J(t)$ based on the fluctuation-dissipation relation:

$$J(t) = G_0 \int_0^{\infty} \frac{d\omega}{\omega} \text{Re} Z_T(\omega) \left(\coth\left(\frac{\hbar\omega}{2k_B T}\right) [\cos(\omega t) - 1] - i \sin(\omega t) \right) \quad (2.57)$$

Now for STM, there is a junction capacitance C_J and all the other environmental factors can be summarized in an impedance $Z(\omega)$, such that a common model for the impedance in STM is [13]:

$$Z_T = \frac{1}{i\omega C_J + Z^{-1}(\omega)} \quad (2.58)$$

Starting with equation 2.51, we can also consider a sinusoidal driving voltage. This then gives the following relation:

$$\hbar \frac{\partial \phi}{\partial t} = eV_{DC} + eV_{AC} \sin(\omega t) \quad (2.59)$$

As we have seen, the phase is subject to strong fluctuations. It is therefore more accurate to write:

$$\phi(t) = \frac{eV_{DC}t}{\hbar} - \frac{eV_{AC} \cos(\omega t)}{\hbar\omega} + \tilde{\phi}(t) + \phi_0 \quad (2.60)$$

Here $\tilde{\phi}(t)$ are the fluctuations which have been treated in this section and the AC drive is the subjection of the next section.

2.8 Microwave-Assisted Tunneling

As seen in the previous section, an AC voltage can lead to a modulation in the phase. This has a characteristic effect on the tunneling current as first reported by Tien and Gordon [116]. Upon integrating equation 2.59 and inserting the result in $\Psi = \Psi_0 e^{-iEt/\hbar + i\phi}$, one can use the identity $e^{iA \sin(\alpha)} = \sum_n J_n(A) e^{in\alpha}$, where J_n is the n -th order bessel function of the first kind and we have introduced the dimensionless amplitude $\alpha = \frac{eV_{AC}}{\hbar\omega}$. This then gives a modified density of states in the presence of microwaves:

$$\rho_{MW}(E) = \sum_n J_n^2(\alpha) \rho(E + n\hbar\omega) \quad (2.61)$$

Plugging this term into the Bardeen expression for the tunneling current, one finds that the tunneling current can be expressed in terms of the original tunneling current in the following way:

$$I(V, \alpha) = \sum_n J_n^2(\alpha) I(V + n\hbar\omega/e, 0) \quad (2.62)$$

The physical interpretation of this equation is as follows: the tunneling electron interacts with the microwave field, allowing it to absorb or emit quanta of $\hbar\omega$. Classically, the maximum available energy is $V_{DC} + V_{AC}$, such that the maximum number of quanta absorbed/emitted is $\frac{eV_{AC}}{\hbar\omega}$. As it is a quantum effect, this transition is not sharp, but there is some tail of density of states decaying beyond this threshold. Figure 2.12 shows an example of equation 2.62 applied to a Gaussian peak.

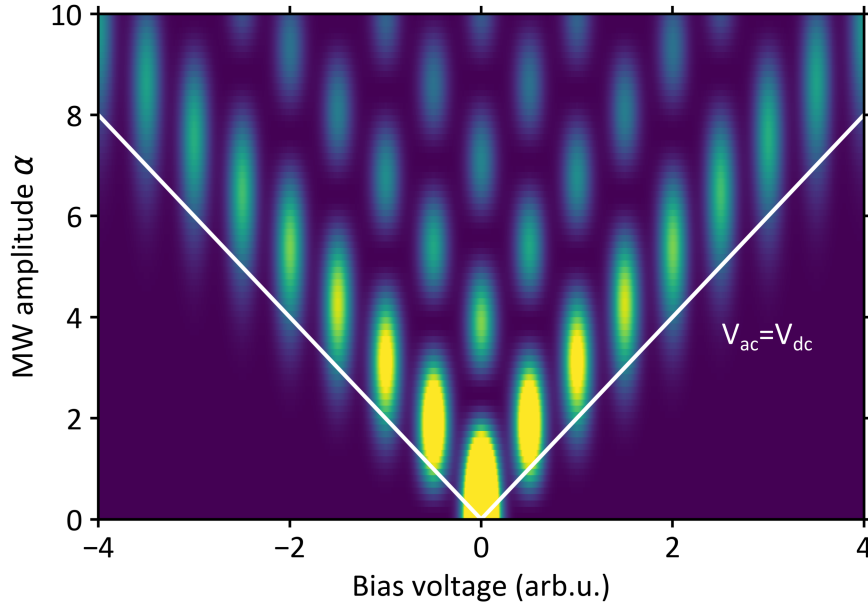


Figure 2.12: Model conductance map generated with the Tien-Gordon equation. The classical line $V_{AC} = V_{DC}$ is shown in white. It can be seen that there is a tail of density of states outside the region enclosed by the white lines.

The Tien-Gordon equation can readily be inverted by taking the Fourier transformation. To simplify the notation, we write equation 2.62 as:

$$g(x) = \sum_n J_n^2(\alpha) f(x - n) \quad (2.63)$$

Taking the Fourier transform, the shift along x becomes a phase shift which can be factored out. We can then find the following equation to calculate the original spectrum (without MW) from a spectrum with microwaves:

$$f(x) = \frac{1}{2\pi} \int_{-\infty}^{\infty} \frac{\tilde{g}(k) e^{ikx}}{\sum_n e^{-ikn} J_n^2(\alpha)} dk \quad (2.64)$$

Here, k is a conjugate variable to the voltage and $\tilde{g}(k)$ is the Fourier transform defined by:

$$\tilde{g}(k) = \int_{-\infty}^{\infty} g(x) e^{-ikx} dx \quad (2.65)$$

In practice, this back-transform only works accurately when (i) the spectrum has sufficiently low noise, (ii) the dimensionless amplitude α is accurately known and (iii) there are no higher order processes in the spectrum. This is because Tien-Gordon theory is only valid within the tunneling approximation [116]. Figure 2.13 illustrates the inversion of the Tien-Gordon equation in practice. We start with a superconductor-superconductor spectrum measured with a vanadium tip on a V(100) surface at 0.56 K. The dI/dV spectrum shows the two characteristic BCS peaks as seen in panel (a). Once we apply the microwaves, replicas form at multiples of $\hbar\omega/e$ as seen in panel (b). We then apply a Fourier transform (panel (c)) which can then be inverted

(panel (d)). While this back-transformation reproduces the two salient features, i.e. the peaks, the calculated spectrum is very noisy, indicating that high quality data along with good filtering during the Fourier transformation are required.

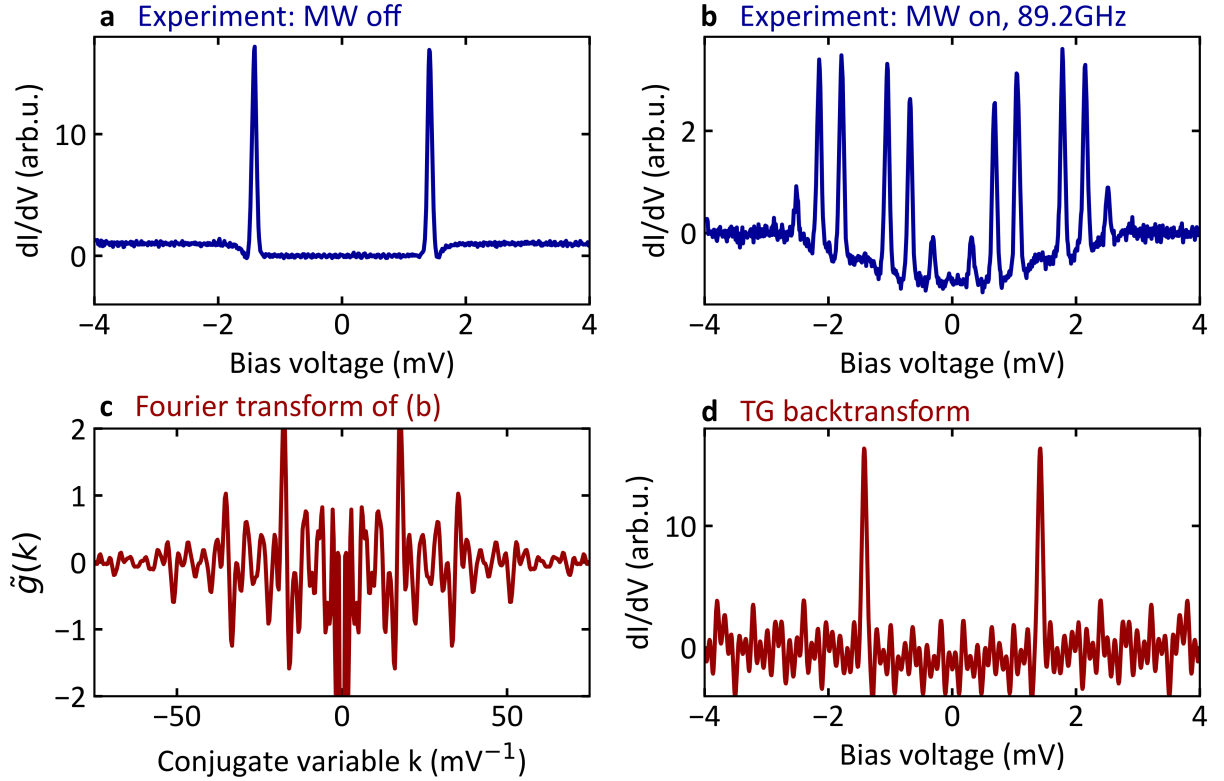


Figure 2.13: Illustration of the inversion of the Tien-Gordon equation. (a) shows an original superconductor-superconductor spectrum measured on V(100) with a vanadium tip at a setpoint of 500 pA and a bias voltage of 3 mV. (b) shows the corresponding spectrum when microwaves at 85.6 GHz are applied. (c) shows the Fourier transformation of (b) and (d) shows the calculated back-transformation.

The Josephson effect has to be treated separately; it turns out [117] that an equivalent equation can be derived, except with the replacement $e \rightarrow 2e$ due to the presence of cooper pairs. More generally, it has been shown that for a transfer of m charges, replicas will form at multiples of $\frac{\hbar\omega}{me}$ [118], but the simple Tien-Gordon theory (even with that replacement) breaks down due to interference processes [119].

2.9 The Josephson Effect

One of the most prominent features associated with superconductivity is the Josephson effect [120, 121]. In the context of planar architectures, where the phase is well-defined, one finds

that there is a current which is related to the phase difference ϕ between two superconductors coupled by a tunneling barrier:

$$I = I_C \sin(\phi) \quad (2.66)$$

It is the current due to transfer of Cooper pairs and as such a second order process. In real systems, a tunnel contact always has a capacitive element and possibly also a resistive component associated to it. Therefore, one of the most common models to understand Josephson junctions is the resistively and capacitively shunted Josephson junction (RCSJ), as shown in Figure 4.6(a). The new equation for the total current is the sum over all the elements:

$$I_{\text{tot}} = \frac{V}{R} + C\dot{V} + I_C \sin(\phi) \quad (2.67)$$

Using Gor'kov's relation between phase and voltage, i.e. $2eV = \hbar\dot{\phi}$, one finds an equation of motion for the phase. It turns out that depending on the capacitance, a washboard potential as shown in panel (b) forms, meaning that current can only flow above a threshold current I_C , namely when the washboard potential has no local minima. Panel (c) shows a typical $I - V$ curve in the under-damped regime where there is no hysteresis.

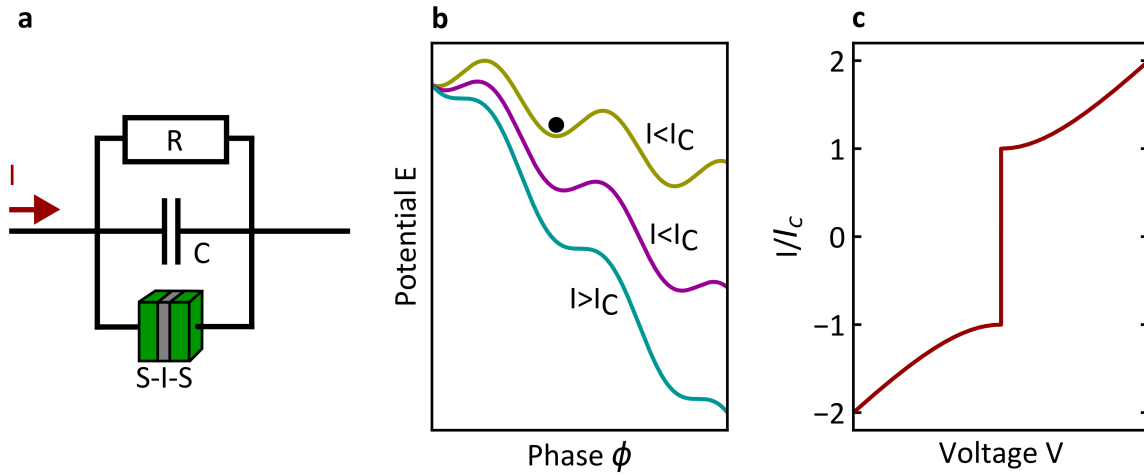


Figure 2.14: Schematic explaining the Josephson effect. (a) shows the circuit of the RCSJ model, (b) shows the washboard potential for different current biases and (c) shows the Josephson effect in the under-damped regime.

The relation between the gap Δ and the critical current I_C was derived by Ambegaokar and Baratoff [122] with the following equation:

$$I_C R_N = \frac{\pi \Delta}{2e} \tanh\left(\frac{\Delta}{k_B T}\right) \quad (2.68)$$

Now in the simplest case we can express the normal state resistance R_N in terms of the transparency and the quantum of conductance: $R_N = (\tau G_0)^{-1}$. This means that equation 2.68 at low temperatures $k_B T \ll \Delta$ simplifies to: $I_C = \Delta \tau \frac{\pi e}{h}$. In STMs, tunneling is charge dominated, and the Josephson effect manifests itself as a feature located at zero bias voltage [123,

124]. A simple model for such phase diffusive Josephson junctions is the following equation [125] (first derived by Ivanchenko and Zilberman [126]):

$$I(V) = I_0 \frac{V/V_p}{1 + (V/V_p)^2} \quad (2.69)$$

Here V_p is a measure of the width of the Josephson effect.

A more rigorous treatment involves $P(E)$ -theory. Based on the observations from Section 2.7, it is possible to derive an equation for the Josephson effect. One has to keep in mind that a tunnel junction is a tunneling resistance and a capacitance at the same time, making the STM effectively a low pass filter [127]. Assuming that the junction interacts with the environment, various expressions can be derived depending on the geometry of the tip. A key result from $P(E)$ -theory is [115]:

$$I_S(V) = \frac{\pi e E_J^2}{\hbar} (P(2eV) - P(-2eV)) \quad (2.70)$$

Here the Josephson energy E_J can in the simplest case be defined as $E_J = \frac{\Phi_0 I_C}{2\pi} = \frac{1}{4} \Delta \tau$. As stated before, the $P(E)$ -function describes the effect of sources of decoherence.

2.10 (Multiple) Andreev Reflections

Another phenomenon that becomes apparent at high conductances is the appearance of Andreev reflections. As an illustration, consider a normal electrode (L, left) coupled to a superconductor (R, right). Then the tunneling current can be calculated using the Green's function formalism [60]. The current has several contributions, $I = I_1 + I_2 + I_3 + I_4 + I_A$. The terms are [128]:

$$I_1 \propto t^2 \int_{-\infty}^{\infty} dE |1 + tG_{RL,11}^r(E)|^2 \rho_{LL,11}(E - eV) \rho_{RR,11}(E + eV) \times [f(E - eV) - f(E)] \quad (2.71)$$

$$I_2 \propto t^2 \int_{-\infty}^{\infty} dE \times \text{Re} [tG_{LR,21}^a(E)(1 + tG_{RL,11}^r(E))] \times \rho_{LL,11}(E - eV) \rho_{RR,11}(E + eV) [f(E - eV) - f(E)] \quad (2.72)$$

$$I_3 \propto t^4 \int_{-\infty}^{\infty} dE |G_{RL,12}(E)|^2 \rho_{LL,11}(E - eV) \rho_{RR,22}(E + eV) \times [f(E - eV) - f(E)] \quad (2.73)$$

$$I_A \propto t^4 \int_{-\infty}^{\infty} dE |G_{RR,12}(E)|^2 \rho_{LL,11}(E - eV) \rho_{LL,22}(E + eV) \times [f(E - eV) - f(E + eV)] \quad (2.74)$$

We focus on the term I_A . This equation can be understood intuitively. We multiply the electron density of states in the left electrode ($\rho_{LL,11}$) with the hole density of states in the left electrode ($\rho_{LL,22}$) and take the probability of an electron turning into a hole in the right electrode ($|G_{RR,12}(E)|^2$). In other words, an electron is reflected as a hole, which is called an

Andreev reflection. In this work, the left electrode is usually also superconducting, allowing for multiple Andreev reflections (MARs). For the remainder of this chapter, we therefore focus on SIS junctions.

Figure 2.15(a) shows a first order Andreev reflection which occurs at a bias voltage of $V = \Delta/e$. This is because the whole energy difference between initial and final state is 2Δ , but it is divided into two sections. This process would scale as $\propto \tau^2$. Then next higher Andreev reflection is a double reflection as shown in panel (b). Likewise, the process involving a double reflection contains three charge transfers and scales as $\propto \tau^3$ etc.

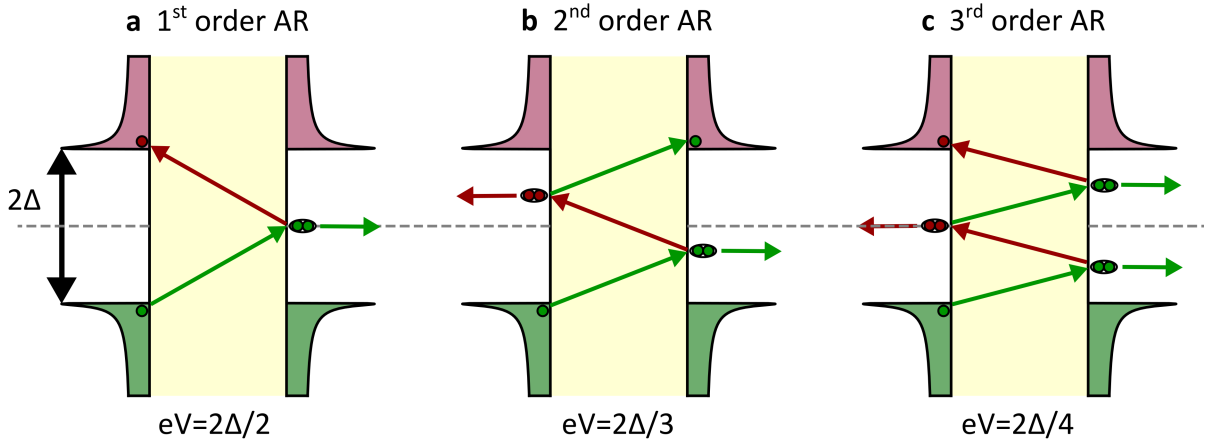


Figure 2.15: Schematic MARs between two superconductors. (a) shows the first order Andreev reflection, (b) a second order AR and (c) a third order AR.

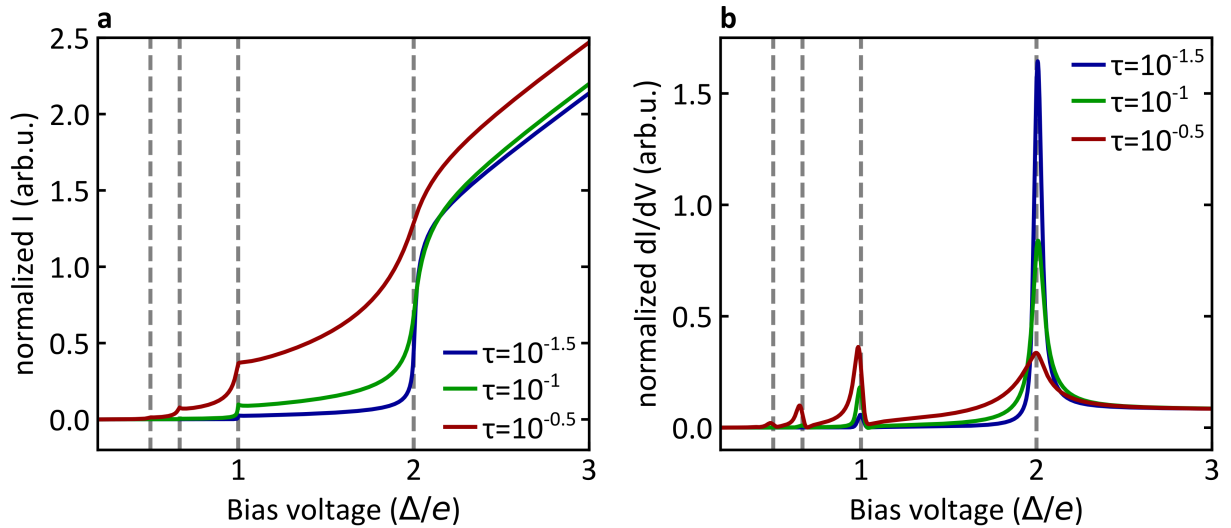


Figure 2.16: Modelling of Andreev reflections. (a) Normalized current in a SC-SC junction at different conductances. (b) Normalized dI/dV . The data was produced using a code by Juan Carlos Cuevas with parameters $\Delta = 1$ meV, $\eta = 0.5$ μ eV, $T = 0.01$ K.

In STM, Andreev reflections can be seen in superconductor-superconductor tunneling. Figure 2.16 shows how the current evolves as a function of conductance according to a Green's function calculation. This does not show the Josephson effect because the code only shows QP tunneling, whereas the Josephson effect is the tunneling of Cooper pairs. This difference in the particle which is tunneling is an important distinction between Andreev reflections and the Josephson effect. The feature that is most prominent at low conductances is the coherence peak at $eV = 2\Delta$ as shown in panels (a) and (b). At higher conductances, multiple Andreev reflections become relevant and contribute to the current. Therefore the step at $eV = 2\Delta$ is smeared out at higher conductances, leading to a broader and lower coherence peak. Once an Andreev reflection is possible, i.e. $eV \geq \frac{2\Delta}{n}$ for $n \geq 2$, there is a new contribution to the current, leading to a step in the current as seen in panel (a). We normalize the current to the conductance τ . One would expect that for large bias voltages, the normalized currents at different conductances would be identical. However, the presence of Andreev reflections leads to an excess current which can clearly be seen in panel (a). This excess current has important consequences for the analysis of experimental spectra. Naively, one would think that the normal state conductance is just the setpoint current divided by the bias voltage, i.e. $G_N = \frac{I_{\text{set}}}{V_{\text{bias}}}$. However, a more precise estimate of the conductance is the slope of the $I - V$ curve, i.e. $G_N = \left(\frac{dI}{dV}\right)_{V \gg 2\Delta}$. We use the latter approach for calculating conductances for the remainder of this thesis.

Figure 2.17(a) shows data measured on a V(100) surface with a superconducting tip at 0.56 K. The spectra were normalized to the normal state conductance. The peaks at $\pm 1.4 \text{ mV} = \pm 2\Delta$ are the coherence peaks. The normalized height of the coherence peaks drops as expected, while the (higher order) subgap features grow with increasing conductance. The peak around zero bias voltage is the Josephson effect which is expected to grow as $\propto \tau^2$. The actual Andreev reflections at $2\Delta/2$ and $2\Delta/3$ are expected to grow as $\propto \tau^2$ and $\propto \tau^3$, respectively. In panel (b), we plot the peak height (the mean of the left and right peak height) as a function of conductance. We add dotted (dashed) lines to the plot, which show the expected $\propto \tau^2$ ($\propto \tau^3$) behavior.

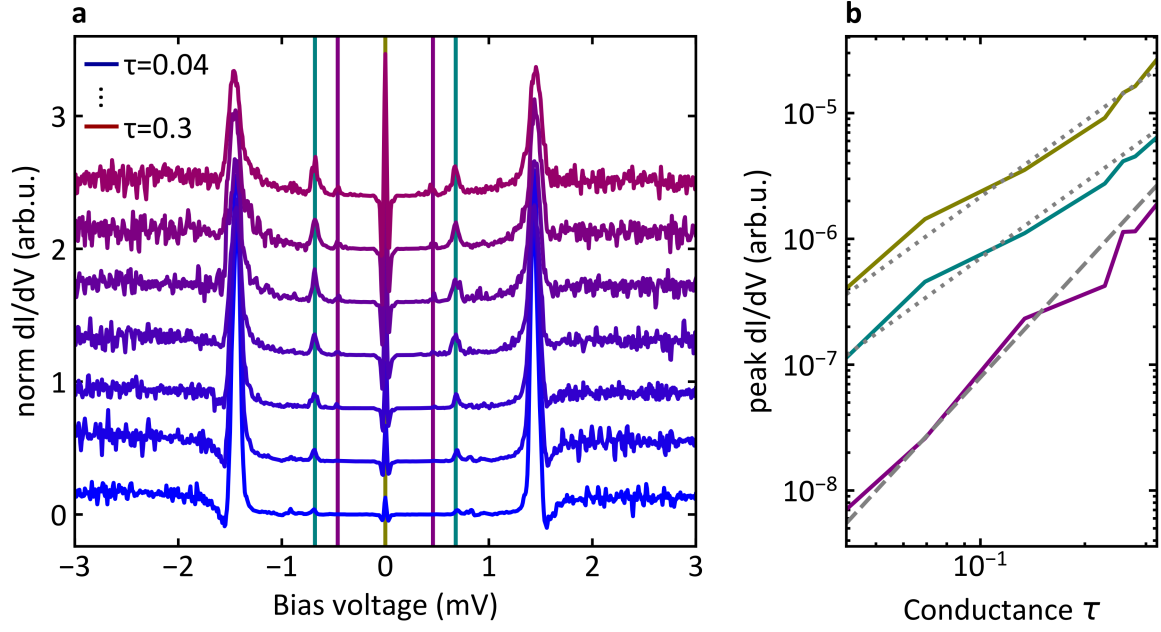


Figure 2.17: Andreev reflections in a SC-SC junction. (a) shows the normalized differential conductance of Andreev reflections measured at 0.56 K with a bias voltage of 3 mV. (b) shows the evolution of the peaks in (a), where dotted lines have a slope of 2 and the dashed line has a slope of 3.

Andreev reflections on both electrodes allow the formation of an Andreev bound state. This subgap state arises purely from Andreev reflections and not – as in the case of YSR states – from some magnetic impurity. Figure 2.18(a) shows a schematic of this bound state and panel (b) shows the energy-phase relation at various conductances, which satisfies the following equation in terms of the phase difference ϕ between the two electrodes:

$$E_B = \Delta \sqrt{1 - \tau \sin^2(\phi/2)} \quad (2.75)$$

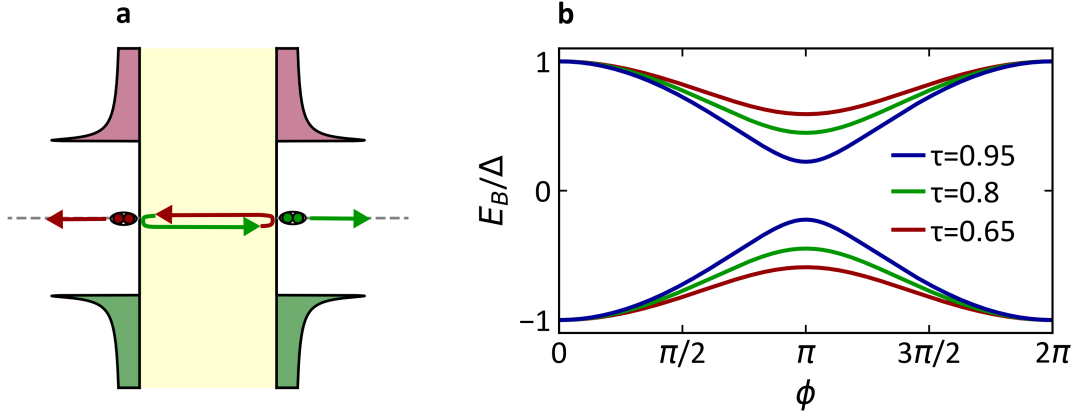


Figure 2.18: Andreev bound state. (a) Schematic of the trapping of quasiparticles due to Andreev reflections. (b) Energy-phase relation of the corresponding bound state.

For higher conductances, the gap between the two branches of E_B becomes smaller because Andreev reflections are more likely. Such Andreev bound states have been seen in nanodevices as for example graphene-based Josephson junctions [129]. Equation 2.75 describes an energy in terms of the phase. However in STM, tunneling is phase-incoherent, such that it is useful to consider the Fourier components of $E(\phi)$:

$$E(\phi) = \sum_{-\infty}^{\infty} E_m e^{im\phi} \quad (2.76)$$

As can be seen from the commutator in equation 2.53, the term $e^{im\phi}$ is a charge transfer operator. Then each component E_m corresponds to the transfer of $2m$ charges. Now the current can be calculated from the following relation [130]:

$$I(\phi) = \frac{2e}{\hbar} \frac{\partial E}{\partial \phi} \quad (2.77)$$

If we apply this equation to Equation 2.75, we find the first Josephson relation (equation 2.66) for $\tau \ll 1$.

A treatment of higher order terms in the context of $P(E)$ theory gives a modified equation for the Josephson effect [131]:

$$I(V) = \frac{2\pi}{\hbar} \sum_{m=1}^{\infty} 2me|E_m|^2 [P_m(2meV) - P_m(-2meV)] \quad (2.78)$$

Here $P_m(E)$ is a modified $P(E)$ function, where the phase correlation gains a prefactor of m^2 . This equation is an extension of the result shown in equation 2.70.

3

Experimental Setup

Having introduced the basic principles of STM, this chapter now shows the implementation of these principles. We provide detailed information about the design of the scan head as well as the electrical connections to explain how the present energy resolution has been achieved. A key tool in this work is an external microwave antenna along with elaborate filtering strategies; we illustrate how this antenna was incorporated in the experimental setup. This is followed by an explanation of the cooling principle and the strategies for vibration isolation. In the end, there is an outlook on how higher frequency radiation sources might be included in the STM.

3.1 Basic Layout

The setup is shown in Figure 3.1. The whole assembly sits on active and passive dampers. The sample can be moved inside the preparation chamber using a manipulator. With the sputter gun and the high voltage filament on the manipulator, we prepare the sample in situ. Then we can transfer it to the STM without breaking the vacuum. The STM is located inside the cryostat which sits on the chamber. Using a wobble stick, the radiation shields may be opened from the side. The electrical feedthroughs are on the top flange of the cryostat. They are then fixed on the pump line interstage before reaching the rack with the measurement controllers (not shown in this figure). To minimise losses in the intensity, the high frequency modules are placed just 30 cm above the top flange.

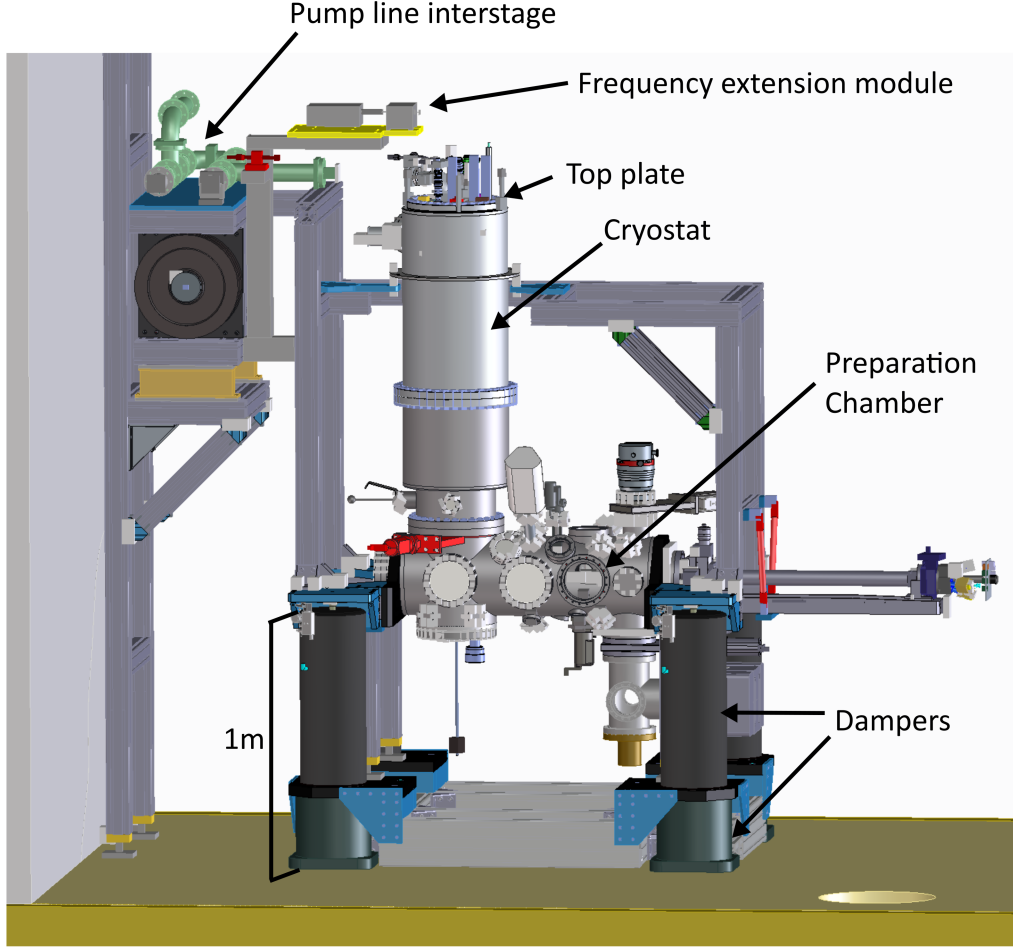


Figure 3.1: 3D drawing of the whole experimental setup. The STM head is located inside the cryostat. All the electrical feedthroughs are located on the top plate.

3.2 Design of the Scan Head

There are various designs for STM heads. All of these designs include a coarse motor, a piezoelectric scanner and some transfer mechanism for the tip and the sample. In this work, we use a scan head design which has already been implemented in the mK-STM at MPI-FKF Stuttgart [10]. The outer shape is a truncated cone for optimal stiffness [132]. This design uses a banana plug for the tip which is directly inserted into the piezo tube. The material is a lead zirconate titanate (PZT), giving a scan range of approximately $(x, y, z) = (1000, 1000, 250)$ nm. The piezo tube sits on the coarse motor (*Attocube ANPz50*).

There is an M20 thread where the sample holder is screwed in. One important difference compared to conventional designs is that ceramics were avoided altogether. All the outer conductors are directly grounded on the STM head. Secondly, instead of a homebuilt coaxial

spring contact, which might have impedance mismatches, we use commercial parts (*Fixtest FK661 and FK652*). We test these and find good mechanical reliability. The final new feature is a hole for the MW antenna which will be the subject of the next section. Figure 3.2 shows a 3D image of the junction including the MW antenna.

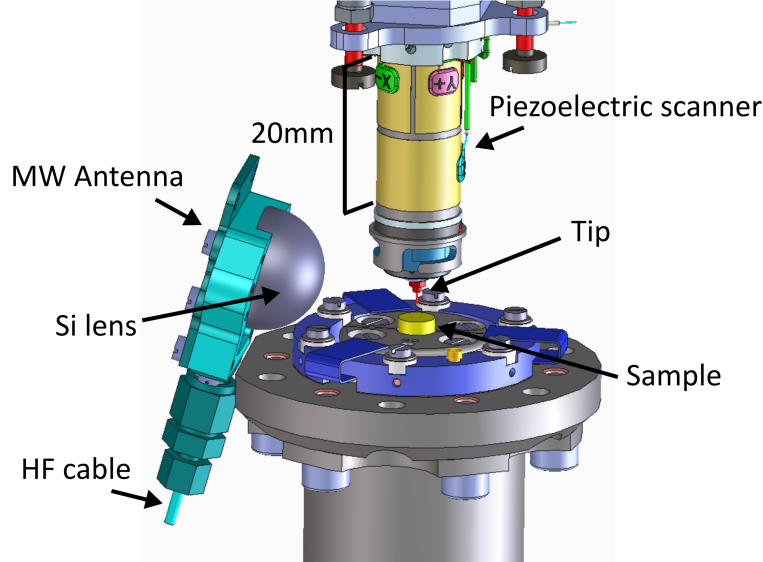


Figure 3.2: 3D drawing of the tunnel junction. The surrounding bronze body is omitted for clarity.

Importantly, the piezo tube should have the z -piezo facing away from the tip (and the x - y piezo closer to the tip). In the first version, we oriented the piezo tube as shown in 3.2 which resulted in significant crosstalk between the z -piezo and the current signal. This crosstalk is greatly reduced as we flipped this piezoelectric tube upside down. Figure 3.3 shows the two versions.

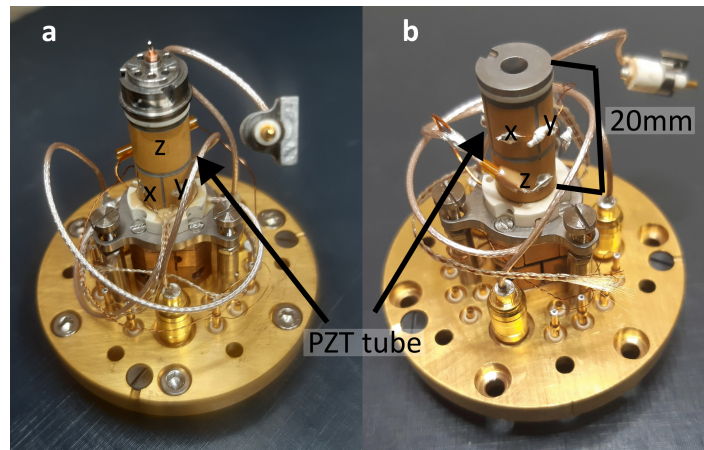


Figure 3.3: Two versions for the orientation of the piezoelectric scanner. In (a) the z electrode is at the top, resulting in significant crosstalk. In (b) the x,y electrodes are at the top. This configuration has low noise and has been used throughout this thesis.

3.3 Electrical Connections

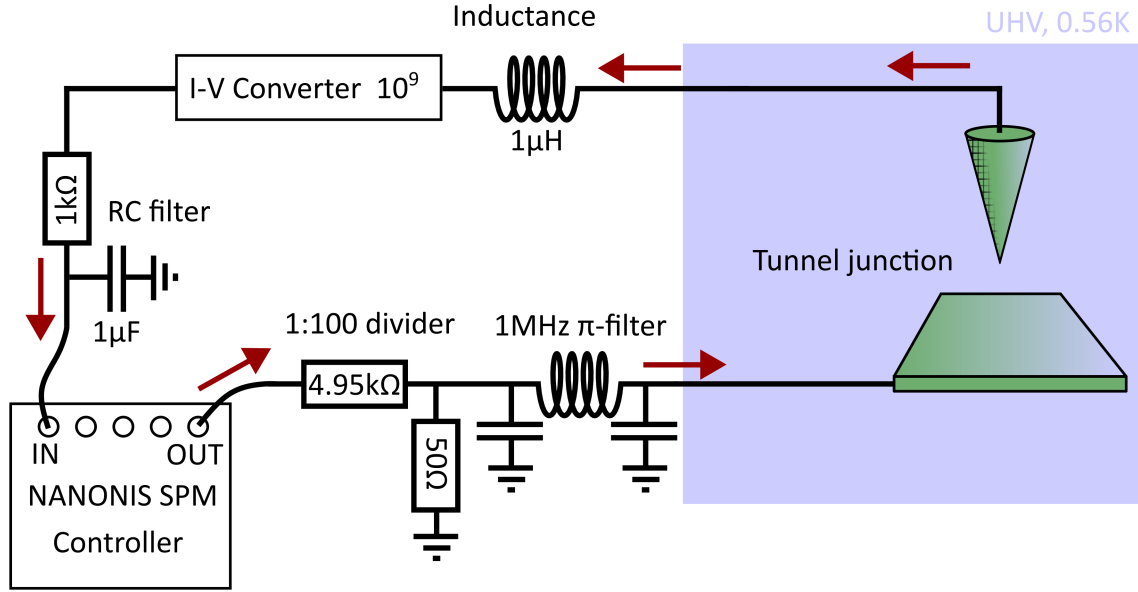


Figure 3.4: Schematic of the measurement lines for the tunneling current. The SPM controller provides a voltage which passes first through a voltage divider and then is filtered by a commercial π -filter (*Api Technologies 1289-004*). After passing through an inductance, the signal is amplified by a commercial $I - V$ converter (FEMTO). Finally the signal passes through another low-pass filter before being read out by the SPM controller.

In figure 3.4, we present the basic filtering techniques used in the experimental setup before the improvements. Starting from the voltage sent by the *NANONIS* software, the bias voltage is divided by a 1 : 100 voltage divider. This helps reduce the input noise by a factor of 100. The voltage divider and a commercial π -filter (*Api Technologies 1289-004*) are incorporated into a low noise housing. Using SMA cables, the bias signal is transferred to 4.2 K stage, where it passes through a superconducting coaxial cable. The resulting tunneling current passes through a 1 μ H inductance at the top flange before reaching the $I - V$ converter with 10⁹ amplification.

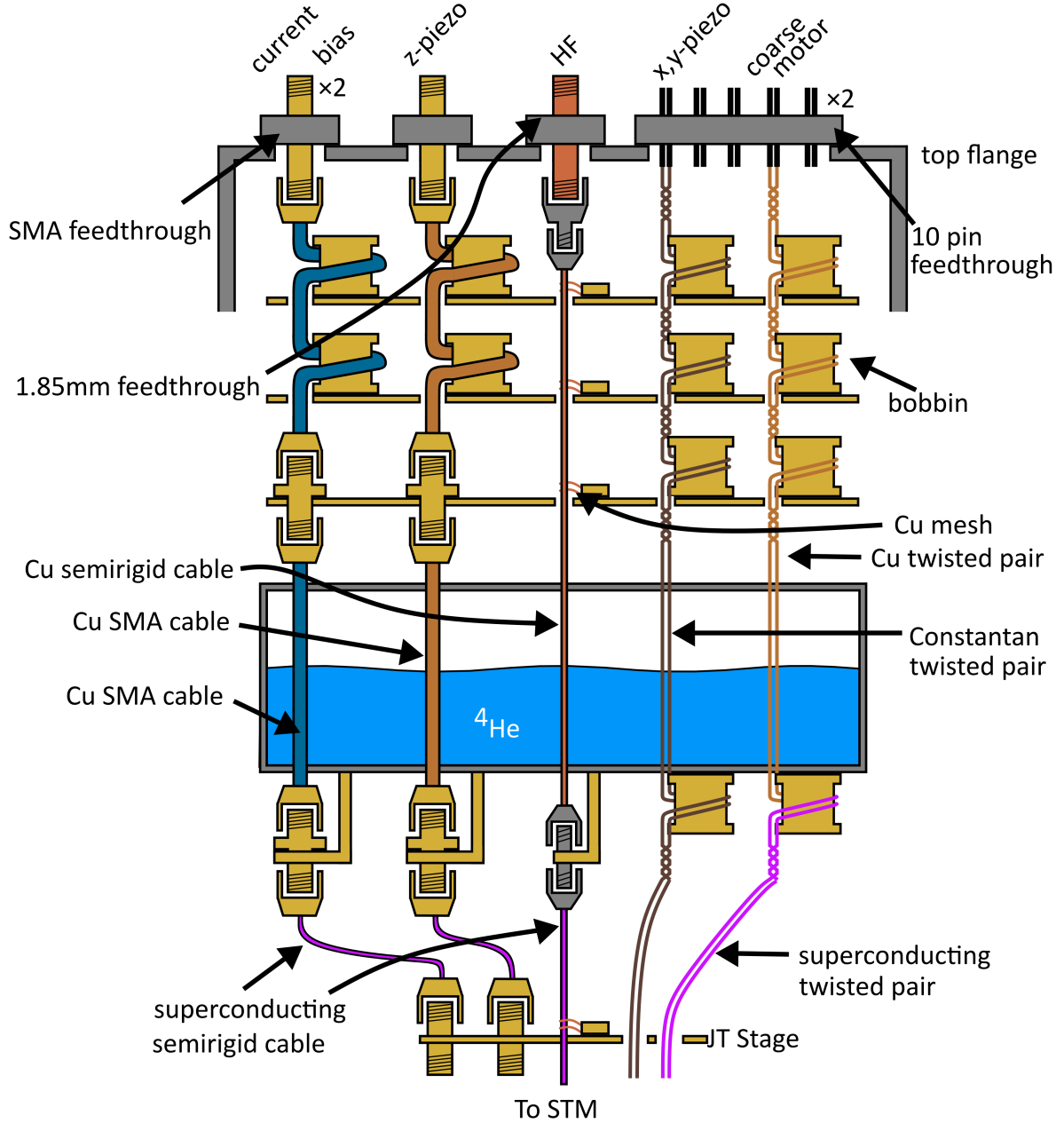


Figure 3.5: Schematic of the cables and thermalization used inside the cryostat. The bias and current line are coaxial SMA cables and switch to superconducting coaxial cables at the base of the helium bath. All the flexible cables are thermalized with bobbins or double-ended adapters.

The specific thermalization strategy and choice of the material for each of the signal lines are shown in figure 3.5. In particular, each line is thermalized at each of the stages of the cryostat. Wherever possible, bobbins are used and the wires are glued around the bobbin using non-conductive epoxy (*EpoTek H77*) or PTFE tape. For semirigid cables, we thermalize the cables using SMA double ended adapters or copper strands which are glued to the outer shield of the cable using conductive epoxy (*EpoTeK H20E*). We chose *EpoTek H20E* for the conductive epoxy due to its high thermal conductivity and low curing time, allowing us to repair cables

in situ. The current and bias lines are implemented as SMA cables (*Stormflex 047*) and then superconducting semirigid cables are used (*Coax Co., Ltd SC-119/50-NbTi-NbTi*). This ensures that the setup remains suitable for potential high-frequency pump-probe measurements. The z -piezo line is similar, except that it uses a lower frequency coaxial cable (*elspec MK5001*) in the normal conducting part. All the other lines are constantan twisted pair (*CMD-Direct 02-32-068*). The thickness of the constantan is $110\text{ }\mu\text{m}$ and the resistance $66\text{ }\Omega/\text{m}$. Constantan (like Manganin) has low thermal conductivity and is therefore ideal for lines which do not carry high currents/ frequencies. A PEEK mesh is used to ensure mechanical robustness and for ease of handling. Regarding the coarse motion (in this case), the stick-slip motion will only operate properly when the frequency is sufficiently high. Therefore copper wires ($\varnothing 90\text{ }\mu\text{m}$, *CMD-Direct 02-32-067*) are used down to the 4.2 K stage and then SC-alloy wires ($\varnothing 100\text{ }\mu\text{m}$, *CMD-Direct 02-32-066*) are employed. The wiring for the antenna is described separately in Section 3.4.

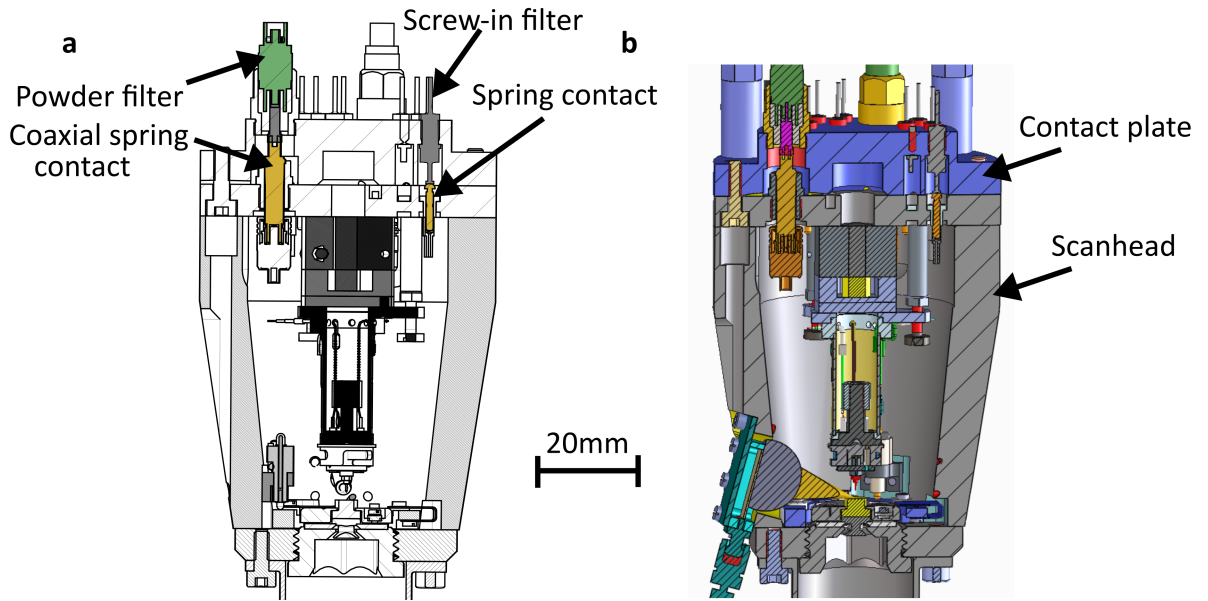


Figure 3.6: Cross-section of the interface. (a) shows the spring contacts used for coaxial and twisted pair cables in color. (b) shows the same cross-section in color.

The STM head can be disconnected readily by virtue of coaxial spring contacts as shown in Figure 3.6. Panel (a) shows the implementation of these contacts. For the coaxial lines, we use a commercial spring contacts (*Fixtest FK661 and FK652*). In this part, both the inner and the outer conductor have spring with a range of motion of roughly 3 mm. In the present design, we aim for a compression of about 1 mm. The part *FK661* has SMB contacts. To connect to the electrodes inside the scan head, we employ SMB connectors. For the connection to the contact plate, we exploit the fact that the non-springy counterpart *FK652* can be mounted inside an MCX connector. Thus we can immediately mount this part (shown in grey in panel (a)) into the powder filter which sits at the base of the contact plate. This design is also flexible in case one

wishes to remove the powder filter for high frequency measurements. The powder filter holder can just be screwed out and replaced by a double-ended female adapter of MCX. As the parts for the coaxial assembly are made out of brass, the STM head is not bakeable. For the twisted pair line, we use the screw-in π -filters (*Api-Technologies 1289-004*) to connect to home-built spring contacts as seen in Figure 3.6(a). With these two designs, the scan head can be disconnected from the contact plate (see panel (b)) in less than one minute, allowing for efficient and reliable maintenance.

3.4 Microwave Antenna

This section is based on paper # 3 of the publication list.

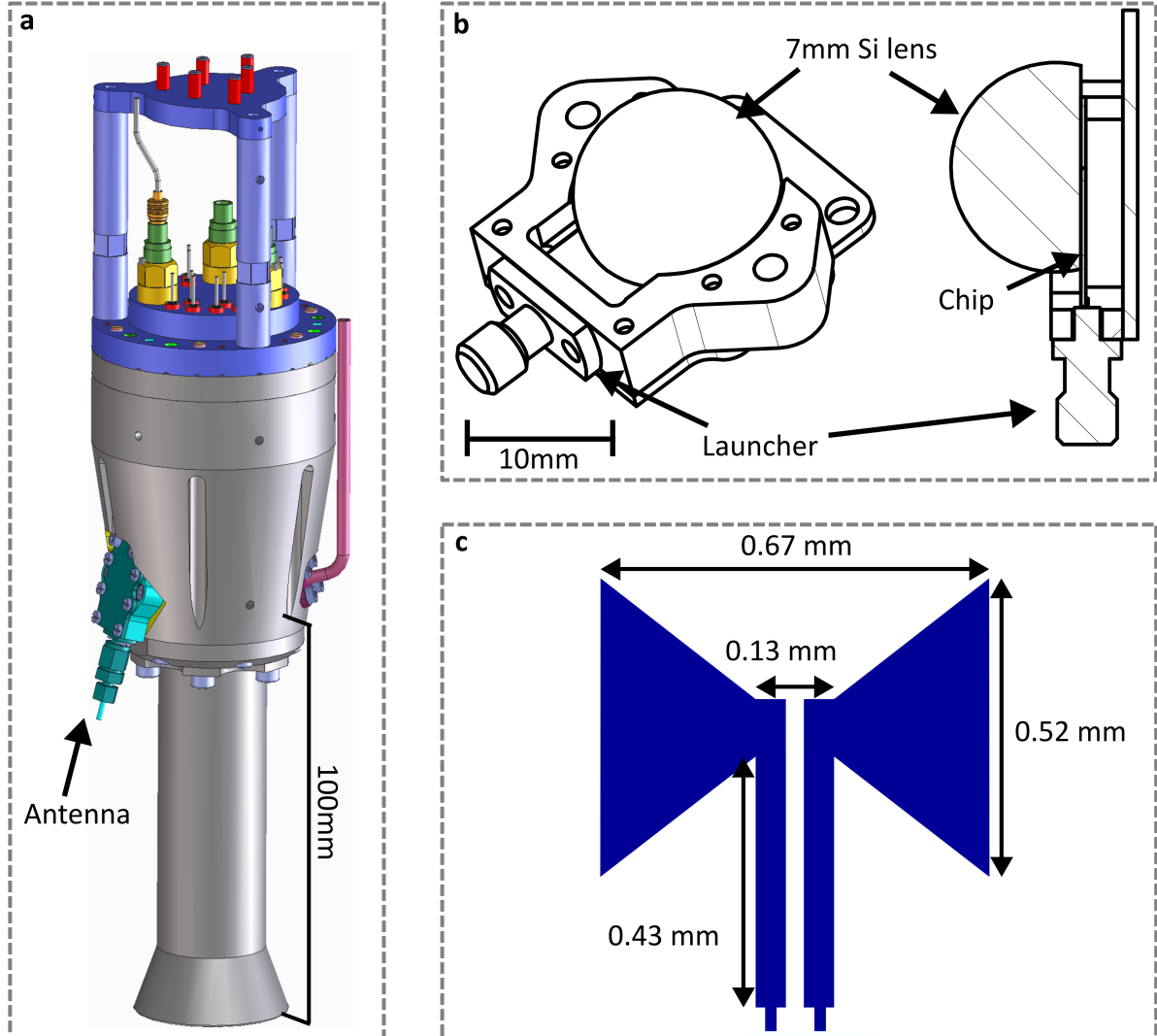


Figure 3.7: Design of the E-Band antenna. (a) shows the antenna mounted on the scan head. (b) is a 3D drawing of the antenna holder. The launcher (Anritsu W1-103F) makes contact to the chip with the antenna. (c) shows the dimensions of the antenna on the chip. Adapted from Drost *et al* [133].

The special feature of this STM is the inclusion of an E-band (60 – 90 GHz) antenna. This antenna is incorporated in the scan head as shown in Figure 3.7(a). While it is still possible to use cables for this frequency, most components will either rely on waveguides (WR12) or chips with appropriately small dimensions. In previous work [133, 134], a bow-tie antenna has been designed to match the desired frequency range. This has the advantage that the regular current and bias lines may still use low-pass filtering – compared to other work where the high frequency is applied directly through the tip. Future work could include a log-spiral antenna

or log-periodic antenna with higher bandwidth [135]. There are currently no commercially available vacuum feedthroughs for this range which means that we resort to a feedthrough which is only specified up to 65 GHz (*KMCO KPC185FFHA*). We use between-series adapters (*CentricRF C8186 1.0mm male to 1.85mm female*) on both ends of the feedthrough to connect to the high frequency cables. These adapters are made of stainless steel and therefore compatible with ultrahigh vacuum. As shown in figure 3.8(a), the losses are comparable to the losses of a 1 mm adapter (*Anritsu 33WFWF50*). We conclude that while the feedthrough *KMCO KPC185FFHA* is not specified up to 90 GHz, it can still be used for this range in practice. The transmission was measured using the setup shown in panel (b). The generator provides the low frequency signal (10 – 15 GHz) via an SMA cable. This signal passes through an extension module which multiplies the incoming frequency by six, reaching 60 – 90 GHz. After passing through an attenuator, the signal is sent through the adapter to be tested. We use a de-multiplier to divide the frequency of the signal by six such that it can be measured by a signal analyzer.

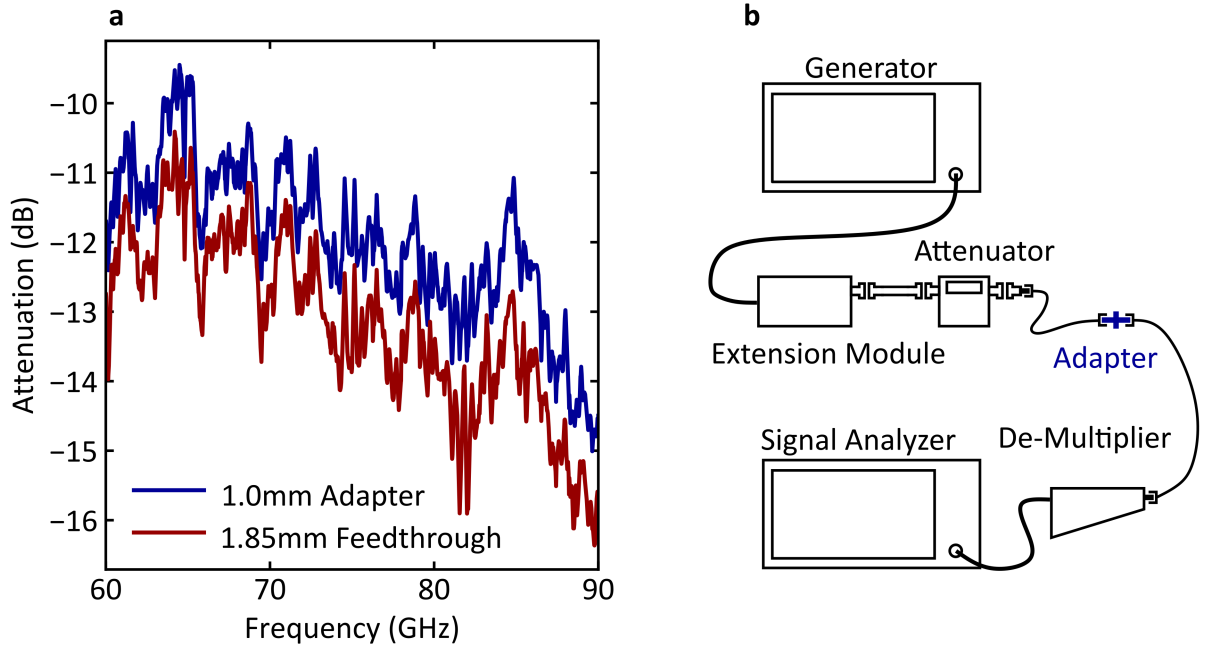


Figure 3.8: Comparison of the two commercial adapters. (a) is a plot of the transmission of the 1.0 mm (*Anritsu 33WFWF50*) and the 1.85 mm adapter (*KMCO KPC185FFHA*). The absolute value of the attenuation includes the attenuation from the two wires connecting two the adapters. These are not exchanged within this measurement as shown in (b).

Figure 3.9(a) shows a view into the scan head with the antenna dismounted. Due to lack in flexibility, only copper strands may be used to thermalize the semi-rigid cable as shown in Figure 3.9(b). This picture also shows how the cables leading to the antenna are installed. Panel (c) is a schematic of the overall cable plan from the generator to the junction. As in the transmission test, we use the extension module (*Virginia Diodes WR12SGX*) to multiply the frequency of the

generator by a factor of six. The attenuator can be used to set the RF amplitude as the extension module supplies a constant output of typically 13 dBm. These two modules are connected by a WR12 waveguide which can be assumed to have negligible losses. From the attenuator, we use a flexible cable (*Stormflex 047*, 35 cm long) to connect to the flange. Inside the cryostat, we resort to copper semirigid cables. We bend the semirigid copper cable in a spiral to give some room for thermal expansion. Once at the 4.2 K stage, there is a female-female adapter (*Anritsu 33WFWF50*) to make a transition to a superconducting semirigid cable made out of NbTi. This cable still needs to be thermalized as losses in the adapters could lead to significant heat-up. In the final section, we connect to the antenna with a short section of flexible cable. In the design of this cryostat, the length of normal conducting semirigid (SR) cable is 75 cm, the superconducting SR cable is 16 cm long, and flexible cable 10 cm.

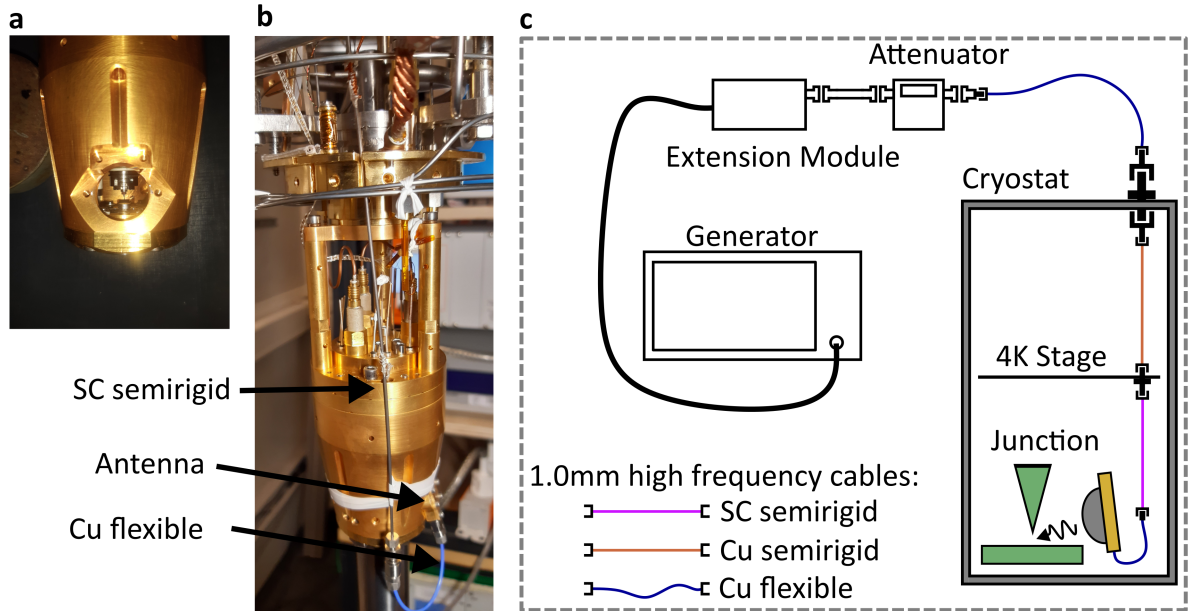


Figure 3.9: Cabling to the antenna. (a) is a picture of the scan head with the antenna dismounted. (b) shows the cabling leading to the antenna. (c) is a schematic of the high frequency connections. The adapters at the cryostat and 4.2 K stage are specified in section 3.3.

3.5 Design of the ^3He Cryostat

The technical details of cryogenic systems can be quite intricate. This chapter just focuses on the main components. For a more rigorous review, the reader may consider a review of different refrigeration techniques [136].

Temperatures down to 4.2 K can be reached using liquid helium. Below that, more refined cooling processes are required. The most common technique to reach 1 K is the use of evaporative

cooling. Liquid helium drops into a pot through a narrow orifice, where it evaporates and the cooling power is simply the latent heat of evaporation times the mass flow. This cooling is not indefinite – according to the Arrhenius equation $p \propto \exp(-L/k_B T)$ [136], i.e. the vapor pressure drops very rapidly at lower temperatures, which means that less helium evaporates. To reach temperatures below 1 K, one has to resort to ^3He . ^3He is a rare isotope which is usually a by-product of nuclear reactions. It is fermionic as opposed to ^4He and therefore has higher vapor pressure, which means that lower temperatures can be achieved. With ^4He , temperatures down to 1.0 K are realistic, whereas with pure ^3He temperatures down to 0.24 K [137] have been reported.

The present system relies on Joule-Thomson refrigeration, which works as follows: when the ^3He is throttled through the orifice and expands, the enthalpy $H = U + pV$ remains constant (ignoring heat exchangers for simplicity). This leads to the definition of the Joule-Thomson coefficient as [136]:

$$\mu_H = \left(\frac{\partial T}{\partial p} \right)_H \quad (3.1)$$

This coefficient is negative for ^3He at 4.2 K, so the temperature of the gas drops and it starts cooling the JT pot. After some time, the temperature drops below the boiling point of ^3He and the ^3He becomes fluid. From this point onwards, evaporative cooling is possible, leading to an increased cooling power.

To reach even lower temperatures, a dilution refrigerator is needed. This technique is not considered here. Table 3.1 lists some of the physical properties of the two varieties of helium [138].

Table 3.1: Comparison of the properties of ^3He and ^4He . We list the vapour pressure, the boiling point at 1 atm and the entropy at 2 K.

Description	Property	^4He	^3He
Vapor pressure at 1 K	$p_{\text{vap},1\text{ K}}$ (mbar)	0.16	11.8
Boiling point at 1 atm	$T_{\text{boil},1\text{ atm}}$ (K)	4.2	3.2
Entropy at 2 K	$S_{2\text{ K}}$ (J/mol)	1.2	13.0
Latent heat at 1 K	$L_{1\text{ K}}$ (J/mol)	80.2	37.5

These physical properties necessitate some technical considerations for realizing the principle of evaporative cooling in practice. Firstly, the high pressure line is required to be extremely thin (about 0.1 mm) in diameter to achieve the target flow rate of ^3He . ^4He becomes superfluid (also called the He-II phase, which is separated from the normal liquid He-I phase by the λ -line) at 2.17 K [138] and can therefore creep up into the capillary. This means that the orifice must be designed as sharp as possible.

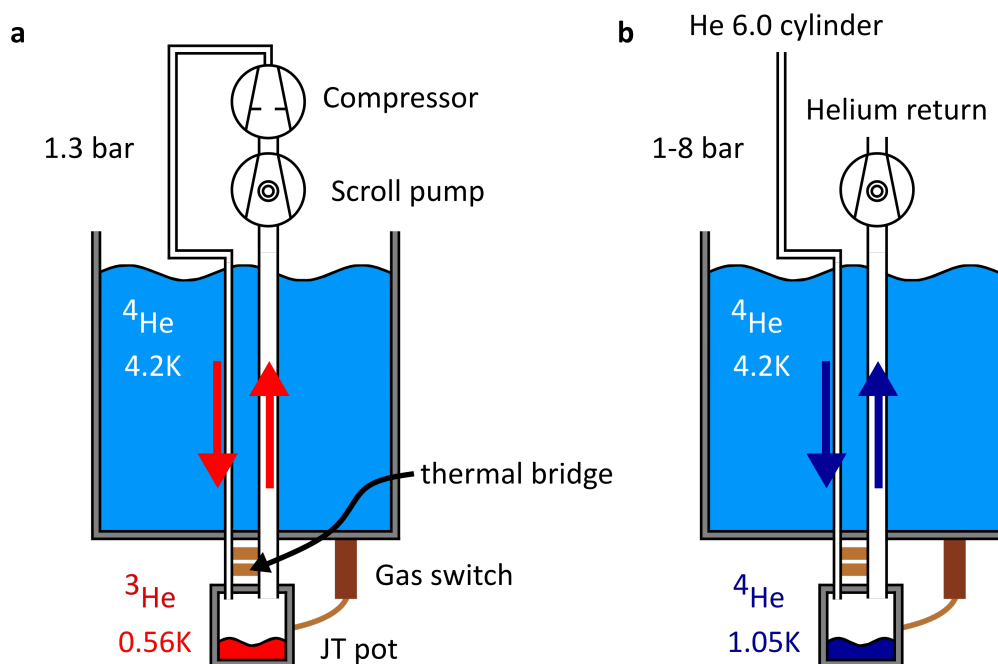


Figure 3.10: Schematic of the two modes of cryostat operation. (a) shows the closed cycle operation with ^3He . (b) shows the open cycle configuration for use with ^4He . In both cases, the gas switch may be used for initial cooling of the JT pot. Cooling shields, valves for gas handling and the STM head are not depicted.

The principle of operation in the present system is shown in Figure 3.10. Panel (a) shows the mode of operation using ^3He . The lines carrying the ^3He pass through the ^4He bath, thereby thermalizing to 4.2K . A combination of scroll pump and compressor drives the cycle. The scroll pump (*Edwards nXDS10i*) pumps on the Joule-Thomson (JT) pot through a thick tube. When ^3He is condensed, the pressure created by the scroll pump is 10^{-1} mbar. However, more important than the final pressure is the mass flow rate out of the JT pot. To maximise this, we use tubing with higher diameter to avoid any bottlenecks in the flow. In operation mode with 4ℓ of ^3He , the high pressure line carries about 1.3 bar, which is achieved using a compressor. The gas then passes through a liquid nitrogen trap to avoid contaminations (not shown here) before being passed through the capillary leading to the JT pot. The high pressure line is inside the pump line to increase the cooling efficiency by heat exchange from the exiting (cold) gas to the incoming (warm) gas. This is illustrated by the thermal bridge drawn in Figure 3.10. For optimized heat transfer to the JT pot (also called Kapitza resistance [139]), there is also a copper mesh at the base of the JT pot. The system may also be operated with ^4He , either in closed cycle (as in panel (a)) or in open cycle (as in panel (b)). In the open cycle configuration, the gas is supplied by a gas cylinder with 99.9999% purity ^4He . In this case it is possible to measure the gas throughput at the outlet, which is 13 ml/min at an inlet pressure of 2 bar ^4He . In the closed cycle configuration, it is also possible to determine the gas throughput by closing a valve to the

scroll pump and then measuring the rate $\frac{\Delta p}{\Delta t}$ at which the pressure in the closed space increases. Since the volume V is known, the flow rate can be determined from $Q = V \frac{\Delta p}{\Delta t \times 1 \text{ atm}}$.

In practice, the helium which is condensed in the JT pot can easily evaporate, for example when a sample is transferred into the cryostat. In that case, we use a gas-gap switch (see Figure 3.10) which we heat using a resistor. This switch contains a charcoal pump. Above 12 K, the helium starts desorbing from the pump, and the gas makes a thermal connection from the helium tank to the JT pot. Once the JT pot is at 4.2 K, the gas-gap switch can be opened and the condensation begins (duration of 30 min for ^4He , 3 h for ^3He in the present system).

3.6 Vibration Isolation

For measuring topographies as well as bias voltage spectroscopies, a good stability of the tunnel junction is critical. Vibrations can be caused by rotating parts such as pumps, by sound, or by moving people in the building, just to name a few examples. Once the measurement system is perturbed by some external vibration, depending on the response function of the internal parts, certain frequencies might resonate with little damping, resulting in vibrations which are detrimental to low-noise measurements. Therefore, most vibration strategies are three-fold: Firstly, the system is decoupled from external sources. This starts by working in a low noise environment. While there are laboratories with huge concrete blocks, the present experiment just uses its own weight for inertia. It is placed inside a sound-proof box and high-quality measurements are performed on weekends when both electrical and mechanical noise due to daily activity in the institute is minimal. In the system here, there is one set of active dampers plus one set of passive dampers. Additionally, the pumps for the gas handling system have been located in a different room to reduce the coupling via sound. Finally, the pumps in the helium return line can couple back to the cryostat causing noise. To eliminate this source of noise, we installed a regulator valve keeping the pressure in the cryostat constant. Secondly, we aim to make the resonance frequencies as high as possible by making the system stiff. Therefore we implement a custom three-pillar design. The whole inner cryostat has three pillars all the way down to the scan head. This should be contrasted with traditional designs where the thermal plates are all mounted to one central rod. In some systems it is necessary to pump on the liquid nitrogen to freeze it and avoid the bubbling. In this system, we do not see a sizeable difference in the spectrum. Most likely this is because the heat load on the nitrogen tank is relatively low and the consumption rate of liquid nitrogen is just 0.23 ℓ/h .

Now for the vibration isolation of the main setup, consider a block of mass m sitting on an air cushion (of heat capacity ratio γ) of area A and height z_0 with pressure p_0 . For adiabatic

compressions, the natural frequency for small perturbations is:

$$\omega_0 = \sqrt{\frac{\gamma p_0 A}{m z_0}} \quad (3.2)$$

This means that the weight should be maximised. With the weight of the present system being about 1.5 t, there is no need for additional weights. On top of that, there are active dampers to counteract external driving. They lead to additional noise at higher frequencies in the noise spectrum there to compensate for the low frequency noise. Figure 3.11 shows a comparison of the vibration spectra as the sensor block is placed on the lab floor, the active dampers or the passive dampers.

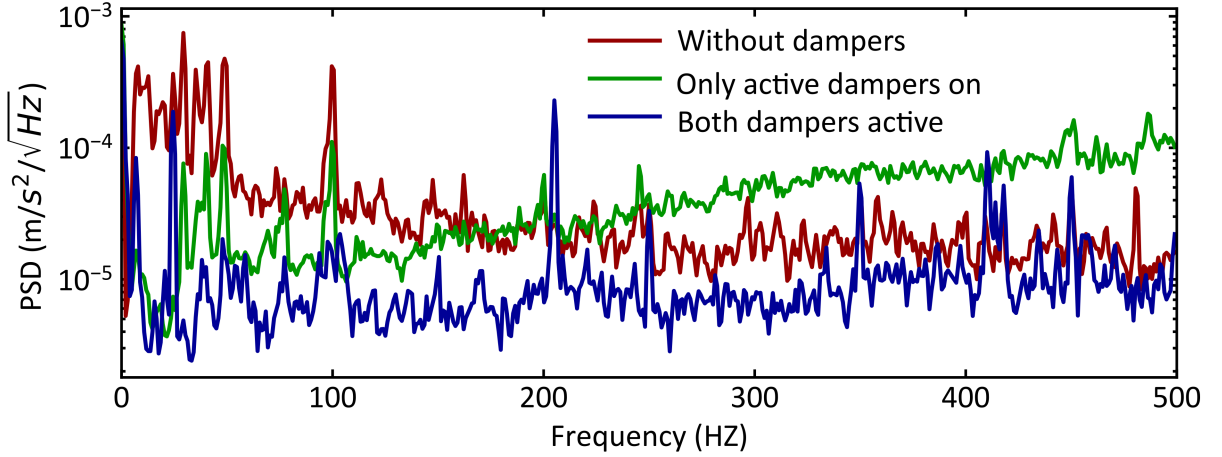


Figure 3.11: Vibration spectra of different damping stages. The spectra without dampers shows large spectral weight at low frequencies. The active dampers filter out these low frequency and the best performance is achieved by a combination of active and passive dampers.

3.7 Outlook: New light sources

While the present microwave range (60 – 90 GHz) is already sufficient to study the excitation of YSR states, higher frequency radiation is required for phenomena with larger energy scales, as for example the quenching of superconductors. Therefore, this outlook presents one possibility of achieving this, which is the use of Josephson Junction arrays [140, 141]. The chips studied in this section have been supplied by Oliver Kieler (PTB Braunschweig).

The present experiments have all been carried out using commercial microwave sources. However, this requires that the generator be placed outside the UHV system which can lead to long cabling distances. It would be beneficial to have the source as close as possible to the sample to minimise losses. To do so, we envision a source at the 4.2 K stage which makes use of the Josephson effect in the following way: on a chip, there are several thousands of small junctions in series. An AC driving voltage leads to a step in the current whenever $V = n \frac{\hbar \omega}{2e}$,

which are so-called Shapiro steps [142]. By adjusting the DC current to the n -th order Shapiro step, we can selectively multiply the incoming radiation by a factor of n .

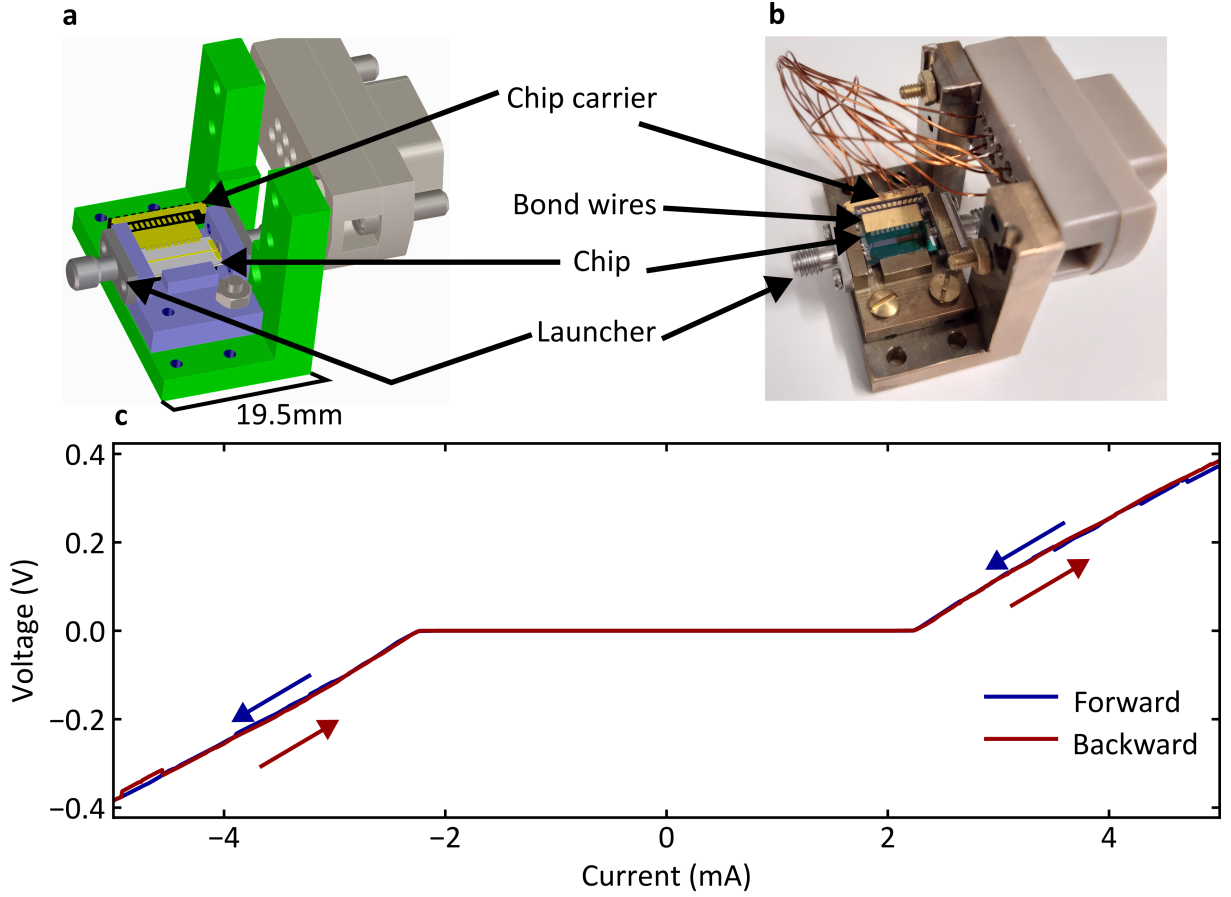


Figure 3.12: Design of the Josephson junction array. (a) is a schematic and (b) is a photograph of the holder where the array is mounted. (c) shows the characteristic IV-curve measured at 4.2 K.

To pick up the radiation, we use a 1.0 mm launcher (*Anritsu W1-103F*) as shown in Figure 3.12(a) and (b). The current and voltage is controlled via pads at the side of the chip. These in turn are connected to the pads of a chip carrier which has been cut to fit beneath the chip. The connection is made by bond wires. From the chip carrier, we make a connection to a sub-D9 adapter made of PEEK. The holder is made of bronze, such that the whole assembly is UHV-compatible.

Figure 3.12(c) shows initial data obtained in a current-biased measurement. As there are 9000 junctions on a chip, the voltage drop is 9000 times higher. To achieve an $I - V$ curve as sharp as shown here, superconducting twisted pair wires are used to connect the sub-D9 jack to the top of the dip stick. The whole assembly can then be dipped in a liquid helium dewar. For application as a microwave source for the STM, we envision placing this assembly at the 4.2 K stage. This means that the distance between the high frequency radiation source and the junction is less than 20 cm, thereby reducing losses due to long cables.

4

Energy Resolution of the New Setup

While the previous chapter already covered some improvements, the present chapter will provide a comparison of the filtering strategies, focusing in particular on the inclusion of metal powder filters at the scan head. We study the Josephson effect to provide a quantitative comparison to other state-of-the-art machines.

4.1 Cold Filters

The basic equation of the cut-off frequency for a π -filter with capacitance L and inductance C is [143]:

$$f_c = \frac{1}{2\pi\sqrt{LC}} \quad (4.1)$$

However, real inductors have a parasitic capacitance (due to coupling between the turns in the coil) [144], which means that π -filters can become transparent at high frequencies. To circumvent this issue, cold filters have been suggested [15]. The grains of the powder surrounding the line lead to Ohmic damping of the skin-effect current at high frequencies. Other designs for low temperature filtering have been suggested, for example filters based on printed circuit boards (PCBs) or lossy coaxial/capillary filters [145].

In the scope of this thesis, we constructed powder filters as shown in Figure 4.1. We start by mixing non-conductive epoxy (*EpoTek H77*) with bronze powder (spherical, $38\text{ }\mu\text{m}$ diameter) in a weight ratio of 1:2. We then cast this epoxy-powder mixture into a cylinder. Even though the core has high metal content, it is still non-conductive. Then we wind insulated copper wire (0.1 mm diameter, 2 m length) around this core and connect it to SMA adapters. Next, we place this assembly inside a bronze cylinder and fill the space with epoxy or an epoxy/powder mixture. Finally we close off the cylinder to the outer conductor of the SMA connector using conductive epoxy (*EpoTek H20E*). Optionally, we place discoidal capacitors inside the SMA plugs to further increase the attenuation at high frequencies.

Figure 4.1(a) shows the attenuation curves of the filters, once in red with capacitors and no powder on the outside, once with powder on both sides (green) and once with powder only on the inside (blue). The capacitors turn this filter into a π -filter which is very effective. In all three curves, there are resonances which have also been seen in literature [15], especially for copper powder as opposed to stainless steel powder. These resonances are most likely due to resonance in the wavelength with the grain size. The measurements were conducted at room temperature. Panel (b) shows a picture of the fully assembled filter (top) and the inner core (bottom). The length of the filter is roughly 6 cm.

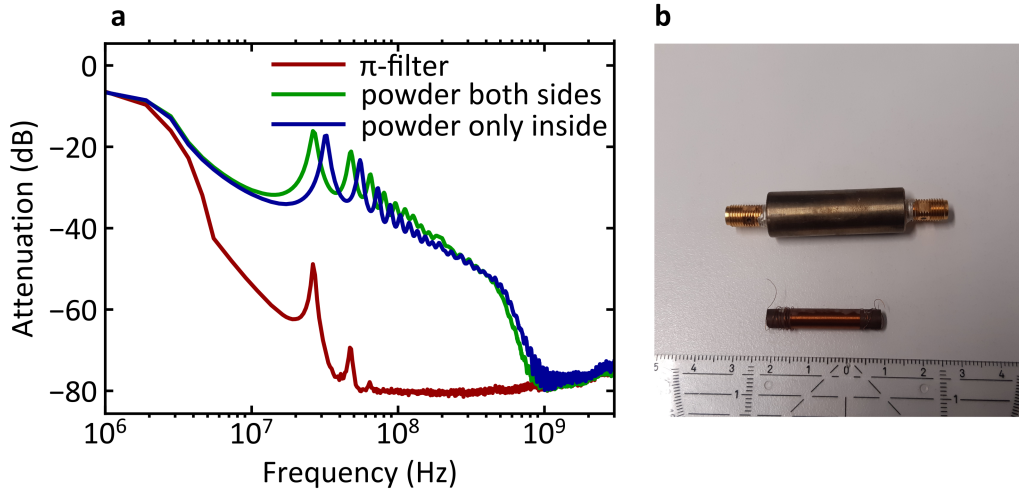


Figure 4.1: Transmission of homebuilt powder filters. (a) shows the transmission at room temperature and (b) is a photograph of the finished filter and the inner core.

After this proof-of-principle, we purchase commercial powder filters provided by *Basel Precision Instruments*. These filters are based on exactly the same principle except that conductive silver epoxy is used to cast the cores [146]. This has the advantage of ensuring high metal content but also poses a risk due to shorts with the wire.

We aim not only to filter the coaxial signal lines, but also the twisted pair wires going into the scan head, i.e. the coarse motor and the x - y motion. We use commercial screw-in filters (*Api-Technologies 1289-004*) which can be mounted on the housing around the junction. This has the advantage that the insulator of the in-built capacitor acts as a ceramic. In previous designs, a ceramic was required to insulate the wires carrying some signal from the grounded housing. To ensure proper performance of the commercial filters, we measured the attenuation at different temperatures. As seen in Figure 4.2(a), there is a loss in performance at lower temperature. This is likely due to a change in capacitance with temperature. However, even at 4.2 K, the filters show an attenuation of more than 20 dB above 10 MHz, which is acceptable for this experiment. Figure 4.2(b) shows the housing of the filters when used at ambient conditions. The assembly is placed inside a home-made copper housing to ensure a low-noise environment.

A cable can be installed at the screw seen in the picture, giving low resistance to ground. The part shown at the bottom is the screw-in filter.

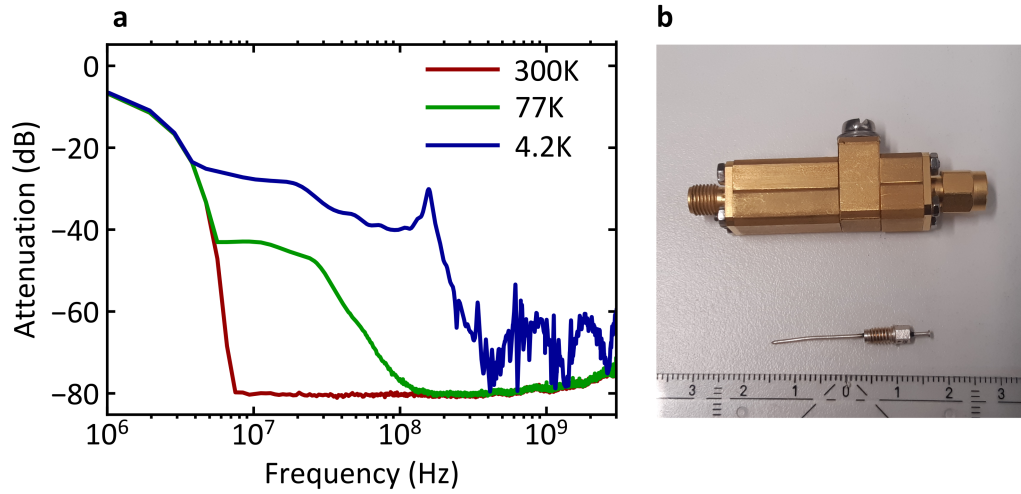


Figure 4.2: Transmission of commercial π -filters at low temperatures. (a) shows the curves measured at different temperatures and (b) is a picture of the housing and the screw-in filter (*Api Technologies 1289-004*).

Figure 4.3 illustrates the new low-noise setup. In comparison to the previous setup, there are two main differences. Firstly, we use another amplifier (*Basel Precision Instruments IF3602*). Apart from that, we use powder filters (*Basel Precision Instruments MFT100Cu2.5Ag*) at the scan head to filter the bias voltage, current and z -piezo line.

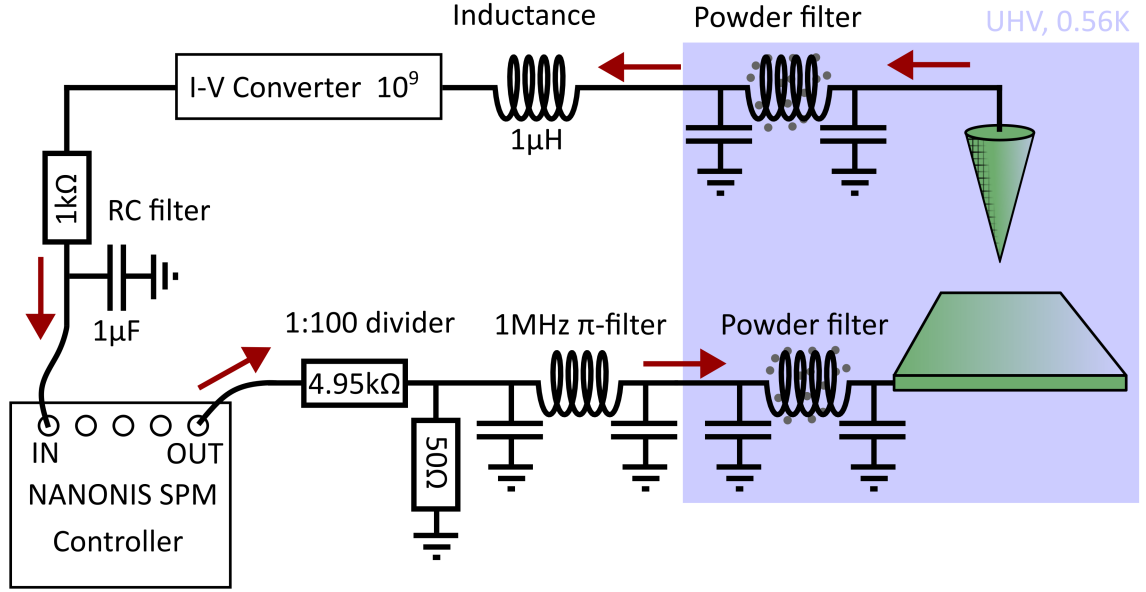


Figure 4.3: Schematic of the improved setup. The SPM controller provides a voltage which is filtered first by a voltage divider and then by a commercial π -filter (*Api Technologies 1289-004*) as well as a commercial powder filter (*Basel Precision Instruments MFT100Cu2.5Ag*). After passing through another powder filter and then an inductance, the signal is amplified by a commercial $I - V$ converter (*Basel Precision Instruments IF3602*). Finally the signal passes through another low-pass filter before being read out by the SPM controller.

4.2 Noise Reduction Strategies

STM measures currents on the order of pA. This means that any ground loops could easily falsify the measurement. In this experiment, we implement a star-like grounding strategy: there is a copper plate on the top of the cryostat which connects to the ground of the institute. All the devices connected to the setup are floating and receive their ground from this plate. To ensure that this is possible, we use isolation transformers such that all the devices required during measurement do not introduce ground loops. Additionally, the high and low pressure ^3He lines are insulated electrically by using plastic KF or Swagelok 6 mm connections. Another component influencing the energy resolution is the $I - V$ converter. We replace our amplifier (*FEMTO*) with a recently developed amplifier (*Basel Precision Instruments IF3602*).

Apart from the Josephson effect, which is presented in the next section, the frequency spectrum of the current gives a good idea about the noise present in the system. When the tip is withdrawn, mainly electrical noise is picked up, whereas when the tip is in contact, also factors such as quality of the tunnel junction and z -stability are important. Figure 4.4 shows a typical noise spectrum. Panel (a) shows the performance of the old setup which shows a very low baseline of about $7 \text{ fA}/\sqrt{\text{Hz}}$ when the tip is withdrawn. When the tip is in contact, the spectrum is

largely affected by the quality of the tunneling contact which may either be due to an unstable tip or vibrations in the z -direction. At a setpoint current of 100 pA, we find a power spectral density which is on average at $100 \text{ fA}/\sqrt{\text{Hz}}$. In contrast to that, panel (b) shows the noise spectra when the powder filter and the new amplifier are included. The baseline has now increased to $14 \text{ fA}/\sqrt{\text{Hz}}$, which might sound surprising at first. However, it should be noted that this is due to having an increased capacitance at the input of the $I - V$ converter. When the tip is in contact, the noise spectrum is similar to the spectrum measured without the filters, indicating that the z -stability did not change. In conclusion, we see that the noise spectra do not fully capture the improvement in energy resolution. The next section presents a more reliable indicator, namely the Josephson effect.

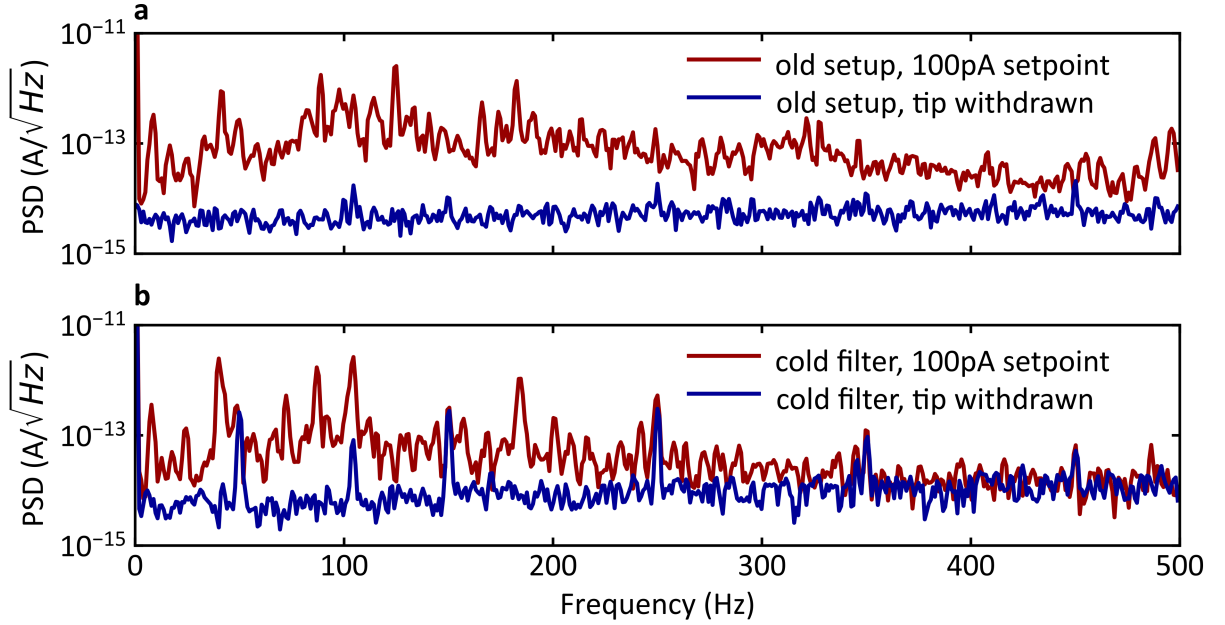


Figure 4.4: Power spectral density of the setup (a) before and (b) after the improvements. The blue lines show the spectrum when the tip is withdrawn and the red lines show it when the tip is in contact at a setpoint of 100 pA. The spectra in (a) were measured with the *FEMTO* amplifier and in (b) with *Basel Precision Instruments IF3602*.

4.3 Josephson Effect Data

As seen in section 2.9, the Josephson effect is a direct measure of the $P(E)$ function, or to put it more generally, it is extremely sensitive to external electronic noise. Therefore the Josephson effect can be used to benchmark the performance of a measurement setup. There are three main indicators which can be used: firstly the peak separation, secondly the peak height and thirdly the prominence of resonances.

We measured the Josephson effect during the various stages of optimization. As described in

section 2.9, the Josephson effect is a second order process, meaning that it can only be seen at high conductances. We do not apply any lock-in modulation to avoid any broadening effects. Figure 4.5(a) shows the Josephson effect measured before the improvements including the cold filters and panel (b) shows the Josephson effect after the improvements. The width drops from $96\ \mu\text{V}$ to $12\ \mu\text{V}$, which is an improvement by a factor of eight.

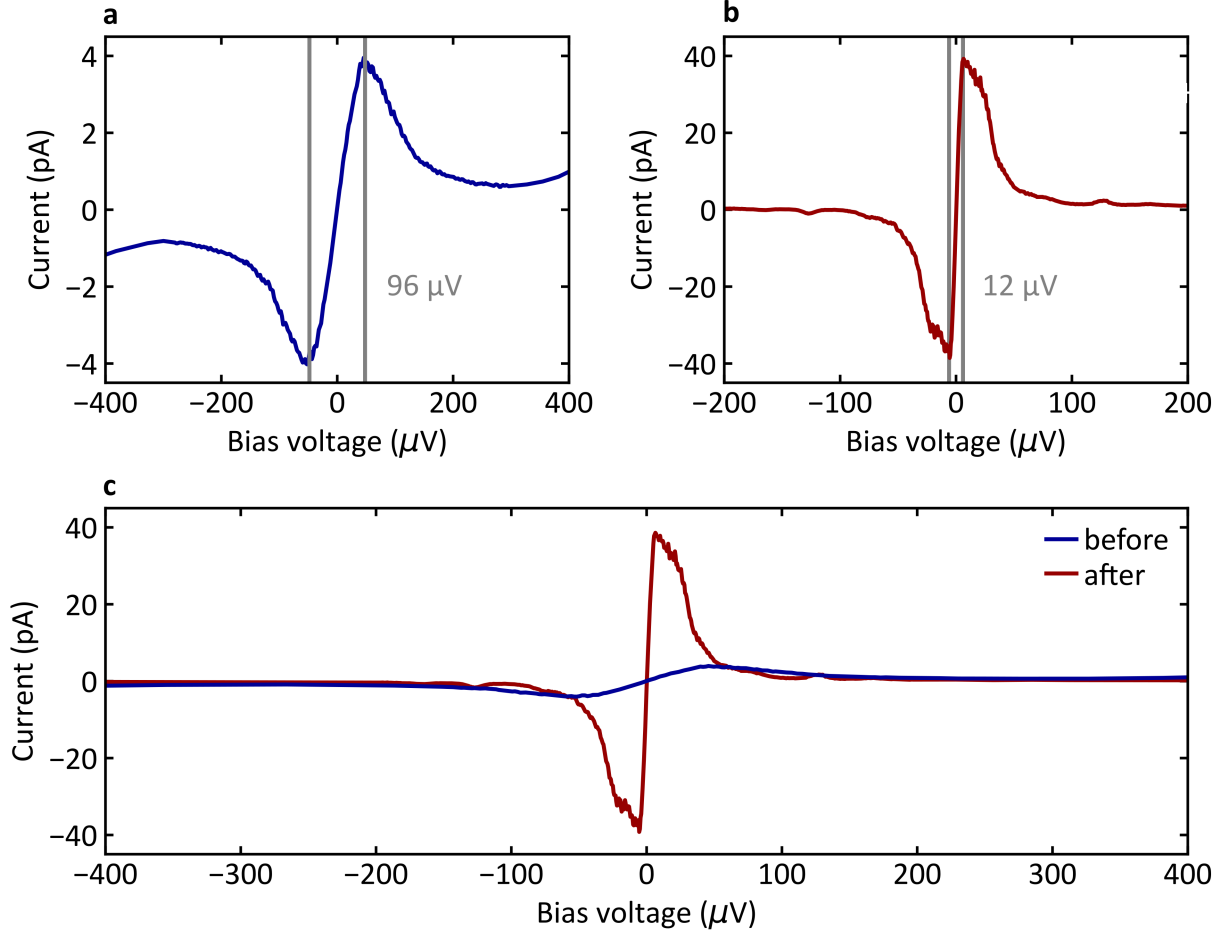


Figure 4.5: Josephson effect (a) before and (b) after improvements. The data was measured at a setpoint of 8 nA and a voltage of 3 mV. The width changes from $96\ \mu\text{V}$ to $12\ \mu\text{V}$, as illustrated in (c).

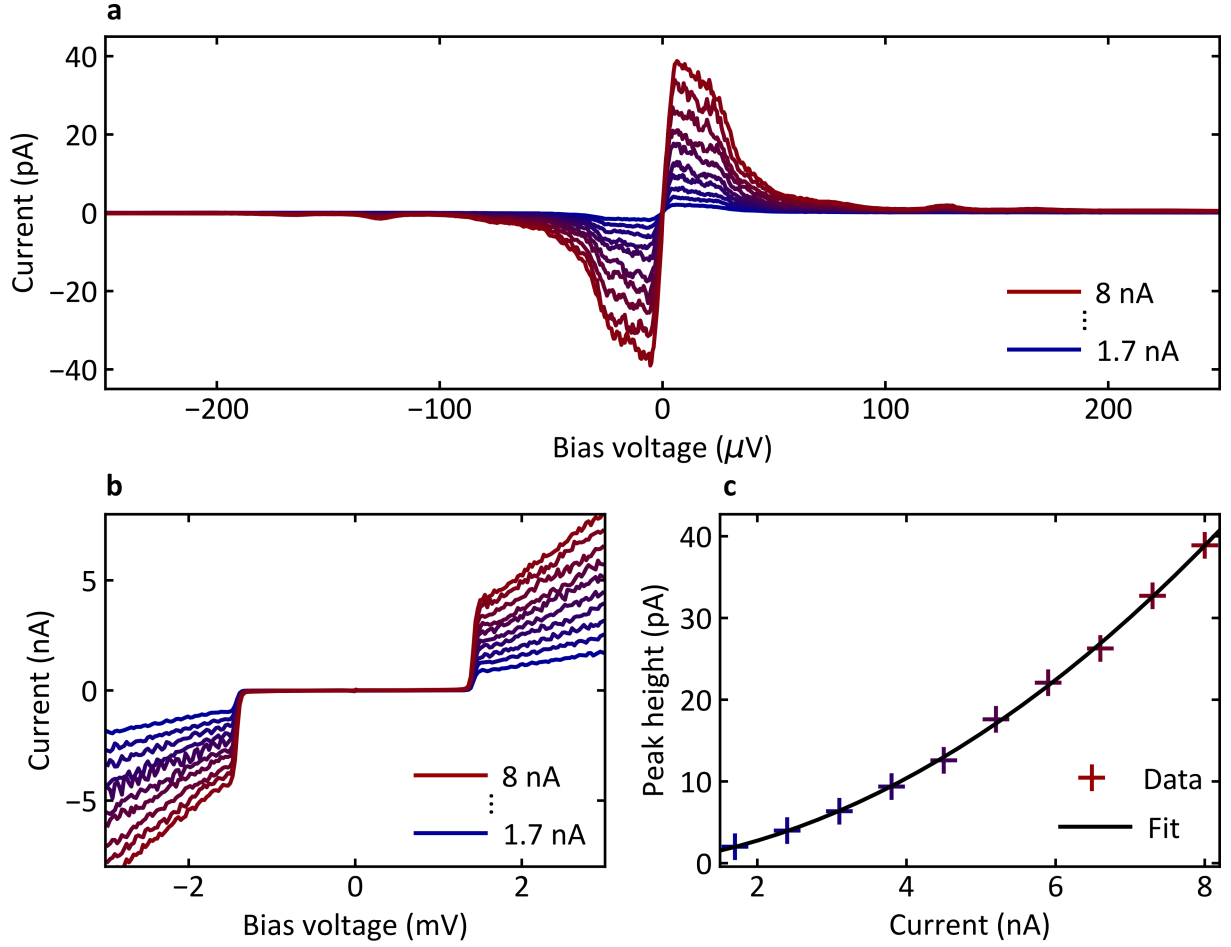


Figure 4.6: Josephson effect as a function of conductance. The data was measured at a bias voltage of 3 mV without lock-in modulation. (a) shows a zoom in onto the region around 0 V of (b). (c) presents the peak height (measured from the maximum current of each curve in panel (a)) as a function of current along with a quadratic fit.

Figure 4.6(a) displays $I - V$ curves at different setpoint currents. The curves show characteristic resonances (for example around 120 μV), indicating that the measurement is so sensitive to external conditions that factors like the geometry of the tip and how it interacts with the environment become relevant [7, 13]. Panel (b) shows a zoom-out of panel (b) to illustrate that the normal state conductance is increasing linearly. From the quadratic dependence of the peaks in the Josephson effect in Figure 4.6(c) we know that the observed feature is indeed a second order process. To put these results into context, current state-of-the-art machines achieve a width of 24 μV (Stuttgart [13]), 9 μV (Maryland [7]) and $\sim 14 \mu\text{V}$ (Madrid [14]). However, these machines operate at mK temperatures, whereas the present system is at 0.56 K, uses an old version of *NANONIS*, namely *RC4*, and is located on the 4th floor. This indicates that there is still room for improvement in other machines and that the limit of energy resolution is not yet reached. Additionally, the observed resonances in the Josephson effect indicate that a broader tip could lead to a further reduction of the width of the Josephson effect, as reported in similar

work [13]. Finally being able to observe the Josephson effect at lower conductances means that this energy resolution will be beneficial for measurements of the Josephson effect with YSR states because high currents can easily destroy YSR states.

4.4 Height of Coherence Peaks

Another indicator of the performance of a setup is the sharpness of features in the dI/dV spectrum, as for example the coherence peaks of a SIS junction. Of course, the coherence peak have an innate broadening such that the width of coherence peaks is not as reliable of an indicator of noise as the Josephson effect. Figure 4.7(a) shows the spectra taken with a vanadium tip on a vanadium surface at 0.56 K. The broadening due to lock-in becomes negligible below an amplitude of $20 \mu\text{V}$. We observe that the coherence peak is increased by a factor of 16 compared to the normal conducting region. Panel (b) shows one of the peaks to illustrate the width of the coherence peaks typically seen in our experiments, which is $70 \mu\text{V}$. In a YSR-BCS junction, we expect a smaller width, as the YSR peak is basically a δ -function. In panel (b) we show a spectrum measured at a lock-in amplitude of $20 \mu\text{V}$. Once we zoom in onto the YSR peak (see panel(d)), we can see width of $40 \mu\text{V}$ in the spectrum.

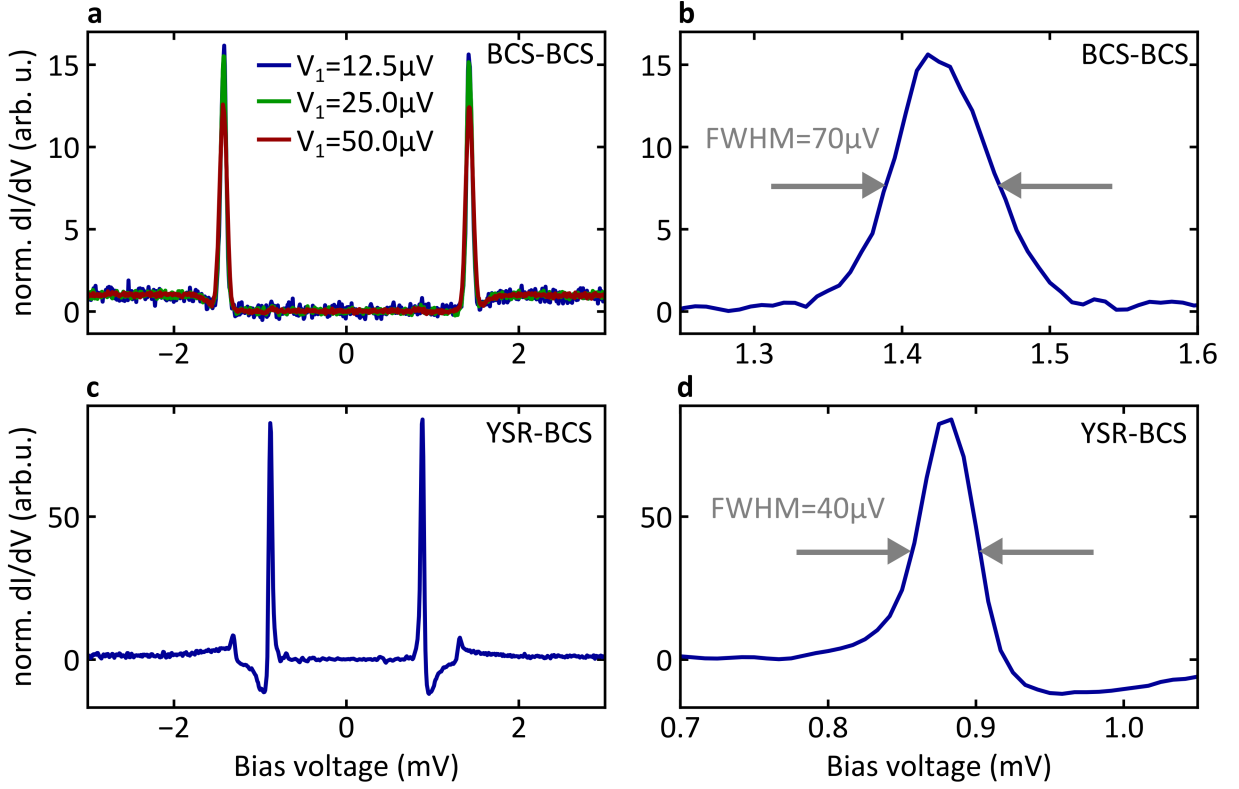


Figure 4.7: Superconductor- superconductor spectra. The setpoint current is 100 pA and the voltage 3 mV. The Lock-in frequency is 781 Hz (a) shows the normalized conductance at different lock-in amplitudes. (b) shows a zoom-in onto the coherence peak to illustrate the width. (c) shows a YSR-BCS spectrum measured at a setpoint current of 500 pA, a bias voltage of 5 mV and a lock-in amplitude of $20 \mu\text{V}$. (d) is a zoom-in of the same spectrum.

4.5 Outlook

This chapter presented improvements which included cold powder filters at the scan head, leading to an improvement in the width of the Josephson effect from $96 \mu\text{V}$ to $12 \mu\text{V}$. This brings the energy resolution of this machine in the region of some of the best low-noise STMs in the world operating at mK temperatures. If these machines were to be equipped with the modifications proposed here, this could push the limits of energy resolution possible with STM. In future, technical improvements such as amplifiers or even better decoupling from external noise sources could lead to further advances in the energy resolution of STMs. At some point, the only limiting factor would be the interaction with the environment as in the context of $P(E)$ -theory.

With this new energy resolution in the Josephson effect, we propose to re-visit the microwave-assisted study of the Josephson effect that has been reported so far [96, 119]. The enhanced sharpness would mean that lower setpoint currents are required. Therefore, the relative height of the Josephson effect compared to multiple Andreev reflections could be made very high by

choosing a lower setpoint current. This would then imply that there are fewer peaks within the gaps such that replicas of the Josephson effect can be tracked more accurately.

5

Microwave Excitation of YSR States

The results of this chapter will be published in paper # 1 of the publication list.

In this chapter, we will firstly present the system to be studied, i.e. YSR states on a vanadium tip in contact with a V(100) surface. We present methods for obtaining this system and for characterizing the transfer function, i.e. the frequency dependent transmission of the cabling and the antenna. Then we present the findings, most notably the appearance of anomalous peaks. We proceed to model these results using a full Green's function approach and find good agreement. We then develop a simplified approach based on the lowest order approximation of the Green's function approach to gain an intuitive understanding of the underlying processes. With this knowledge we are finally able to disentangle the two families of tunneling processes.

5.1 YSR states on a Vanadium tip

Vanadium is notoriously difficult to clean as it has a number of impurities including oxygen, carbon and sulphur [31, 147, 148]. Such impurities can give rise to YSR states. Additionally, we have observed that by continuously dipping the tip, a plethora of YSR states can be generated. The energy of the resulting states is highly variable, which means it can be matched to the input frequency of the microwave setup, thereby making vanadium an ideal system for studying resonant phenomena where energies need to be matched. Furthermore, having the YSR state on the tip avoids problems such as drift in the x - y direction. In fact, recent work [43] has suggested to use a YSR tip as a tool to measure a number of different phenomena. Here we restrict ourselves to a YSR tip in contact with a superconducting sample.

5.2 Sample and Tip Preparation

We clean the V(100) crystal by repeated cycles of sputtering in with Ar ions and annealing to 700°C. While preparation at higher temperatures lead to a flat surface, the relatively low preparation temperature leads to a surface dominated by oxygen reconstruction, leading to square terraces of typical height 180 pm. Figure 5.1(a) shows a typical scan taken at a setpoint current of 100 pA and a bias voltage of 3 mV. The oxygen reconstruction in panel (b) can only be seen with a very sharp tip. The bright spots in the topography could be oxygen vacancies [149]. However, it is the subject of further studies to find out if and how the topography correlated with YSR states being present in the sample.

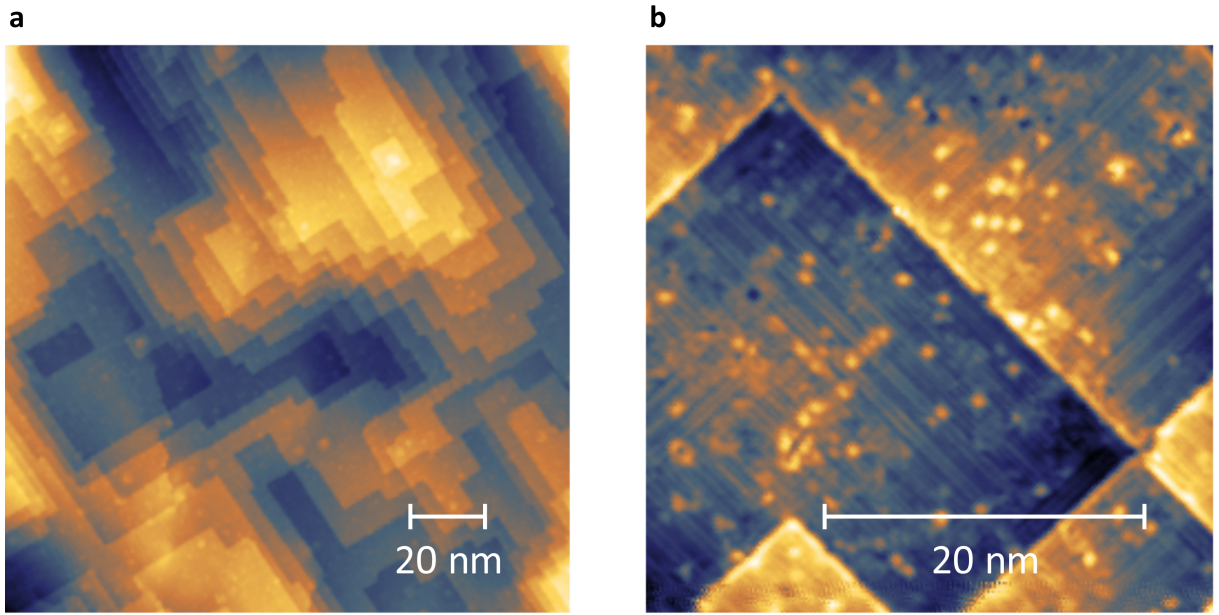


Figure 5.1: Topographies of a V(100) surface. The maps were taken at a bias voltage of 3 mV and a setpoint of 100 pA. A quadratic background has been subtracted for better visibility. Panel (a) shows the general appearance of the terraces. In Panel (b), the oxygen reconstruction can be seen.

We use Vanadium tips cut from 99.98% purity Vanadium wire of 0.25 mm diameter. We obtain a superconducting tip by field emission on a clean surface at 40 V and currents of 20 μ A. The YSR tip is produced by iteratively dipping the tip as shown in Figure 5.2. It typically takes about 1000 dips to find a YSR state with sufficient intensity. Some YSR states are very unstable and spontaneously disappear, particularly at high currents. To select the most stable YSR states, the algorithm routinely checks whether the state survives at high conductances and under microwave irradiation.

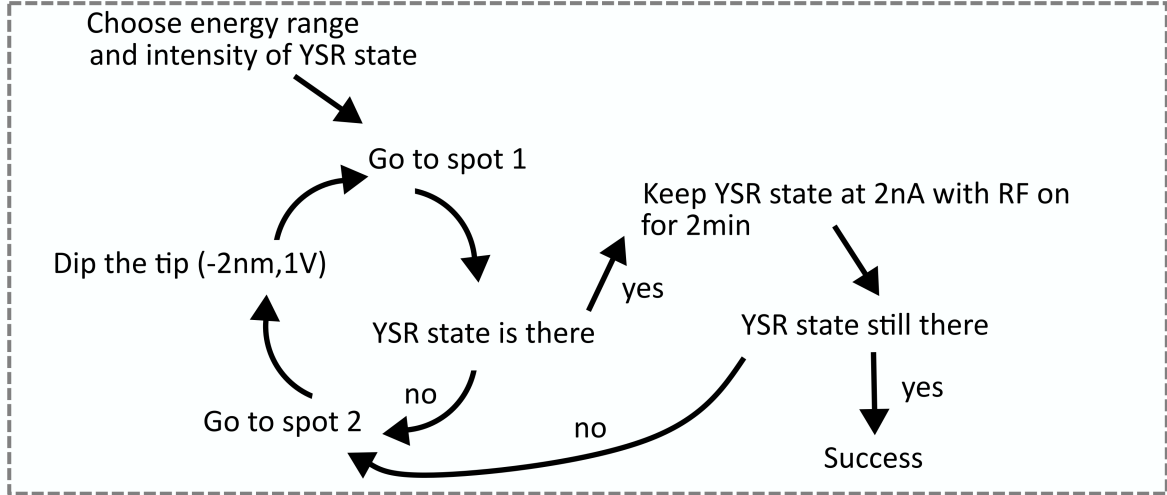


Figure 5.2: Algorithm for generating a YSR state on the tip. The tip is moved between a dipping spot and a measurement spot. Before terminating, the algorithm checks the stability of the YSR state at higher conductances.

YSR states in vanadium vary in energy and intensity as can be seen in Figure 5.3. This should be contrasted with other work (e.g. Mn on Pb(111) [76]), where the YSR state is always at the same energy. Possibly, the large variance in YSR energy in vanadium is due to different configurations of vanadium atoms and oxygen vacancies. There are YSR states with a strong BCS channel (see Figure 5.3(e)), but for the purposes of this work, we try to keep the BCS channel as small as possible. This means that spectra like in Figure 5.3(d) are desirable to see purely the effect of superconductor-YSR tunneling without the influence of the superconductor-superconductor tunneling. Finally, it has been observed that YSR states on vanadium sometimes move with transparency due to a change in the impurity-substrate coupling – sometimes even across a quantum phase transition (QPT) [87]. In this work, the focus lies on the interaction of YSR states with microwaves, such that we select YSR states which do not move with transparency.

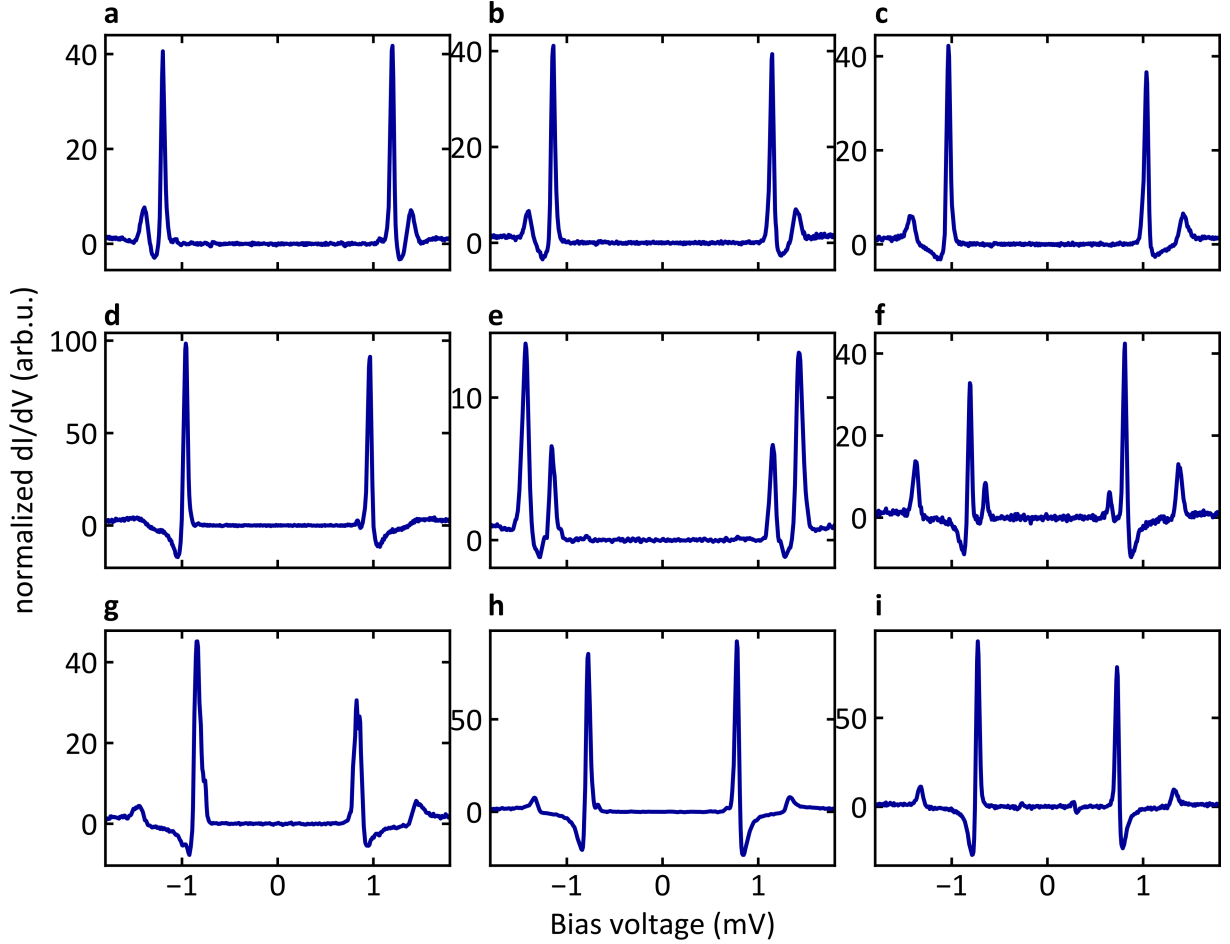


Figure 5.3: Normalized dI/dV curves of various YSR states. YSR states differ in energy and intensity. Panel (f) has a YSR state so close to zero such that the excited state is thermally occupied, giving rise to two extra peaks.

5.3 Observation of Anomalous Peaks

Given that we have a stable YSR state, one immediate question is whether – and if so, how – the microwaves can drive the YSR state. Previous experimental work [96] and theoretical work [23] has shown that at conductances around $\tau \sim 10^{-2}$, there are significant deviations from Tien-Gordon theory (see Section 2.8 for the basic theory). This led to the observation of asymmetric peaks which were accounted for by considering Andreev processes through the YSR state. Here, we re-visit this experiment and perform experiments at constant frequency where we sweep the dimensionless microwave amplitude $\alpha = \frac{eV_{ac}}{\hbar\omega}$. In comparison to previous experiments, we have two advantages: firstly the improved energy resolution, leading to sharper peaks, and secondly the fact that YSR states on vanadium have a wide range of energies. This means that we can tune the YSR energy to our frequency range to explore possible resonances.

We start with a continuous wave application of microwaves and sweep the dimensionless

amplitude. As expected from Tien-Gordon theory, higher order replicas are accessible with increasing α and we can illustrate these findings in a false color plot of the conductance. A striking feature is the appearance of anomalous peaks which are not covered by standard Tien-Gordon theory [116]. Figure 5.4(a) shows this finding. We compare this with basic Tien-Gordon theory, which should hold in the tunneling regime only. We take the spectrum without microwaves ($\alpha = 0$) and then apply the Tien-Gordon equation (equation 2.62) to this spectrum to create a false color plot of the dI/dV as shown in Figure 5.4(b). From now on, we refer to the peaks not predicted by Tien-Gordon theory (panel (b)) as anomalous peaks. Later we will show that these peaks correspond to a tunneling process which excites the YSR state.

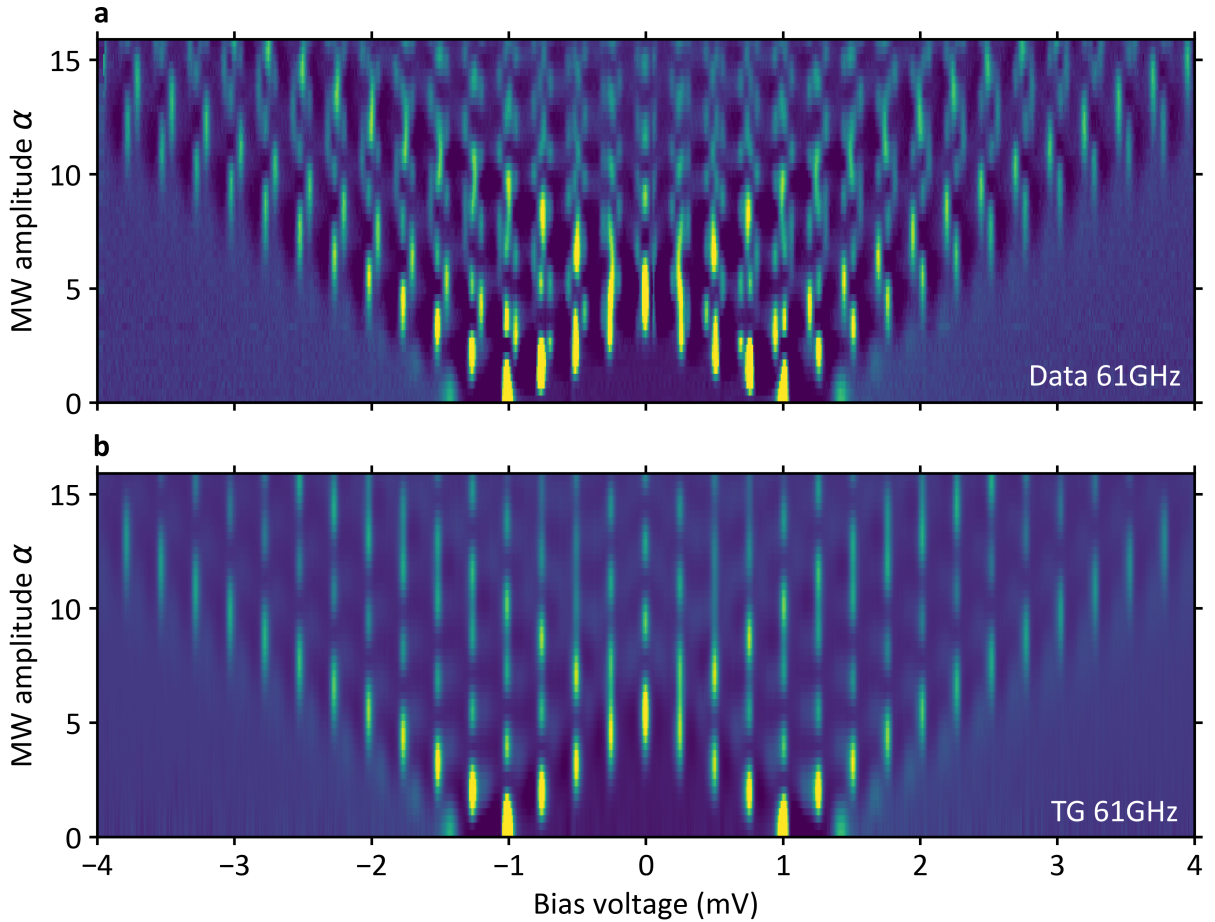


Figure 5.4: False color plots of spectra as a function of MW intensity at 61 GHz. (a) shows the data and (b) shows the expectation when Tien-Gordon theory is applied on the $\alpha = 0$ spectrum of figure (a). The setpoint was 500 pA and the voltage 3 mV.

To prove that this effect is reproducible, we measure another conductance map at 89.2 GHz. The replicas move because the frequency has changed. But the anomalous peaks are still present. Combined with the fact that we observe additional peaks also for other YSR states, we can conclude that the peaks reported here are real and not some artifact of the measurement.

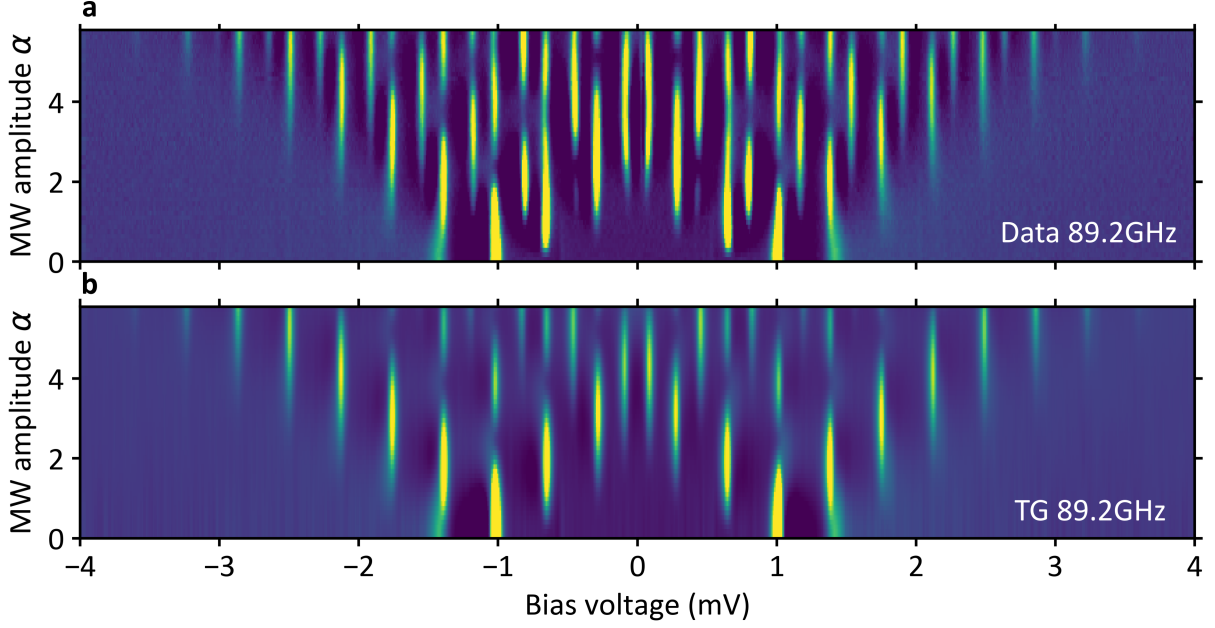


Figure 5.5: False color plots of spectra as a function of MW intensity at 89.2 GHz. (a) shows the data and (b) shows the expectation when Tien-Gordon theory is applied on the $\alpha = 0$ spectrum of figure (a). The setpoint was 500 pA and the voltage 3 mV.

5.4 Frequency-Dependent Measurements

To identify the origin of the anomalous peaks seen in Section 5.3, we conduct frequency-dependent measurements. For a given n -th order replica of a feature at E_0 , its position evolves according to the following equation if we assume single quasiparticle tunneling:

$$E = E_0 + n\hbar\omega \quad (5.1)$$

That means that frequency-dependent maps can be used to trace zero-order replicas by identifying vertical lines. In this section, we apply this method to the microwave-assisted tunneling into YSR states. First we present how we can keep the RF amplitude constant using a transfer function. Secondly, we present the results and observe that there are precisely two families of processes.

5.4.1 Transfer Function

Especially for high-frequency cabling, the transmission is strongly dependent on the frequency of the signal. This requires a careful determination of the transmission at each frequency before running a frequency-dependent measurement.

The transfer function can be measured on any non-linear feature in the dI/dV -curve using the rectification of the RF signal [53].

Depending on the width of the feature compared to the microwave frequency, there are two methods of determining the transfer function. Firstly, for the regime where the feature in the system is much larger than the microwave energy, i.e. $\Delta E_{\text{system}} \gg \hbar\omega$, Tien-Gordon theory converges to a classical description. As seen in equation 2.6 for the broadening due to lock-in modulation, the resulting dI/dV curve is smeared out with the inverse semicircular distribution, allowing to deduce the voltage at the junction V_{AC} from the change in the gradient of a non-linear feature [150].

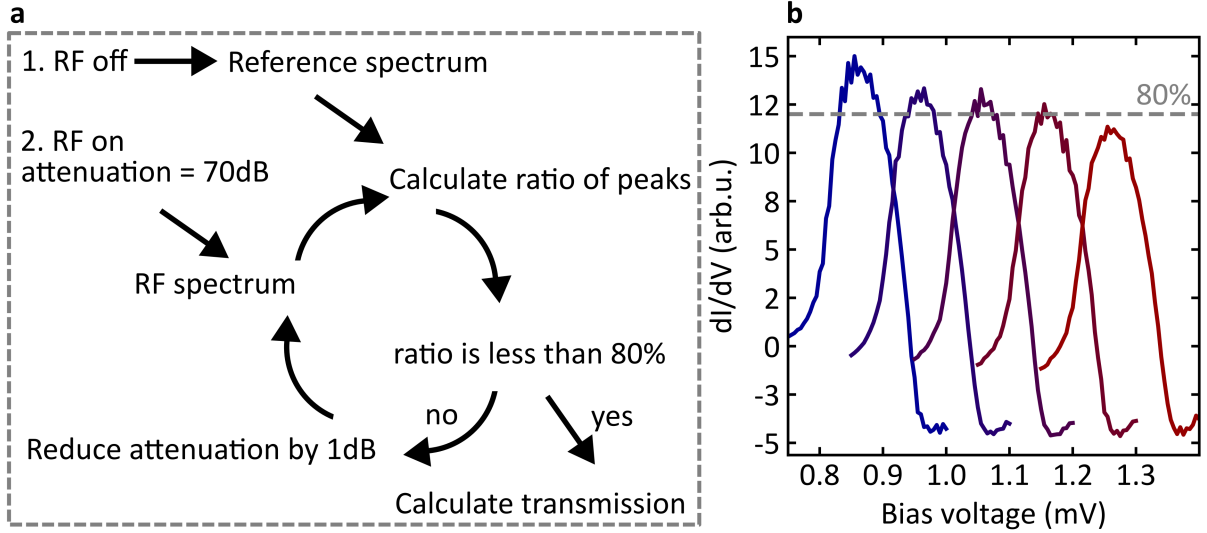


Figure 5.6: Illustration of the transfer function feedback algorithm. (a) is a diagram of the algorithm and (b) shows the peaks measured during this process. The peaks are offset for better visibility. The bias voltage is 3 mV with a lock-in modulation of 70 μV and the setpoint current is 100 pA

In the present experiment, the microwave frequency is large compared to the typical width of features, i.e. $\hbar\omega \gg \Delta E_{\text{system}}$. This means that the height of replicas can be used to extract the AC voltage at the junction, simply by inverting $J_n^2(\frac{eV_{\text{AC}}}{\hbar\omega})$ for the n -th order replica. During the preparation of YSR states, the surface is superconducting for most of the time. This means that sharp peaks (coherence peaks or YSR states) are available. With the width being about 50 μV , the overlap between replicas is very low because the frequency range 60 – 90 GHz corresponds to a voltage range of 248 – 372 μV . The inversion of a Bessel function $J_0(\alpha)$ is only possible in the range where $J_0(\alpha)$ is one-to-one (where $c = J_0(\alpha)$ has only one solution), i.e. for low AC amplitudes. To ensure that this condition is met, we adopt a feedback mechanism as shown in Figure 5.6(a). Starting at maximum attenuation (70 dB here), we reduce the attenuation in steps of typically 3 dB and measure a quick spectrum of the peak each time. The algorithm stops once the peaks drops below a set threshold (80% here) and then we can invert $J_0^2(\alpha)$ to determine the amplitude. Panel (b) shows five successive peaks measured during this process. We apply a large lock-in modulation of 70 μV to artificially broaden the peaks and thus avoid drift effects in the bias voltage and improve the signal-to-noise ratio. To calculate the actual loss, we reference

the AC voltage at the junction to the input voltage. The maximal available voltage is the value of V_{AC} at 0 dB attenuation. Figure 5.7 displays the result of measurements taken ten days apart. The transfer function does not change significantly. However, for a precise measurement, the transfer function should be measured immediately before the measurement.

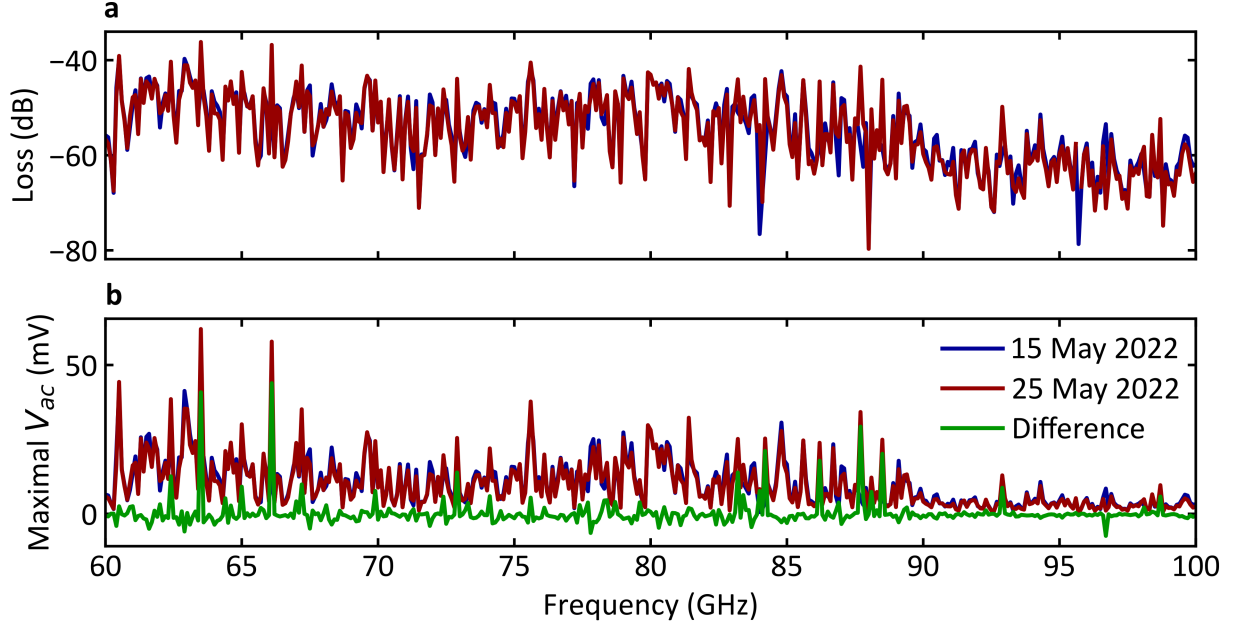


Figure 5.7: Plots of the transfer function. (a) shows the calculated loss in dB referenced to the input power of 16 dBm and (b) shows the maximum available AC voltage at the junction.

5.4.2 Constant Amplitude Sweeps

To perform constant amplitude sweeps, we first create a YSR state, then measure the transfer function and immediately after that conduct the measurement to keep the effect of variations in the transfer function to a minimum. We limit the attenuation (see setup in) to 12 dB to avoid excessive heat up of the junction, leading to an unstable tunneling contact.

Figure 5.8(a) shows the result of this measurement. We identify vertical lines (corresponding to the zeroth order replica) at ± 1.04 mV and ± 0.41 mV and indicate them by a line connecting panels (a) and (b). Panel (b) shows where replicas of these two zeroth order lines are expected. This simple assumption that there are two families of peaks each with $E_n = E_0 + n\hbar\omega$ reproduces all the features seen in panel (a). Panel (c) shows the original spectrum (without microwave irradiation) where the anomalous peaks have been added by hand at the corresponding positions.

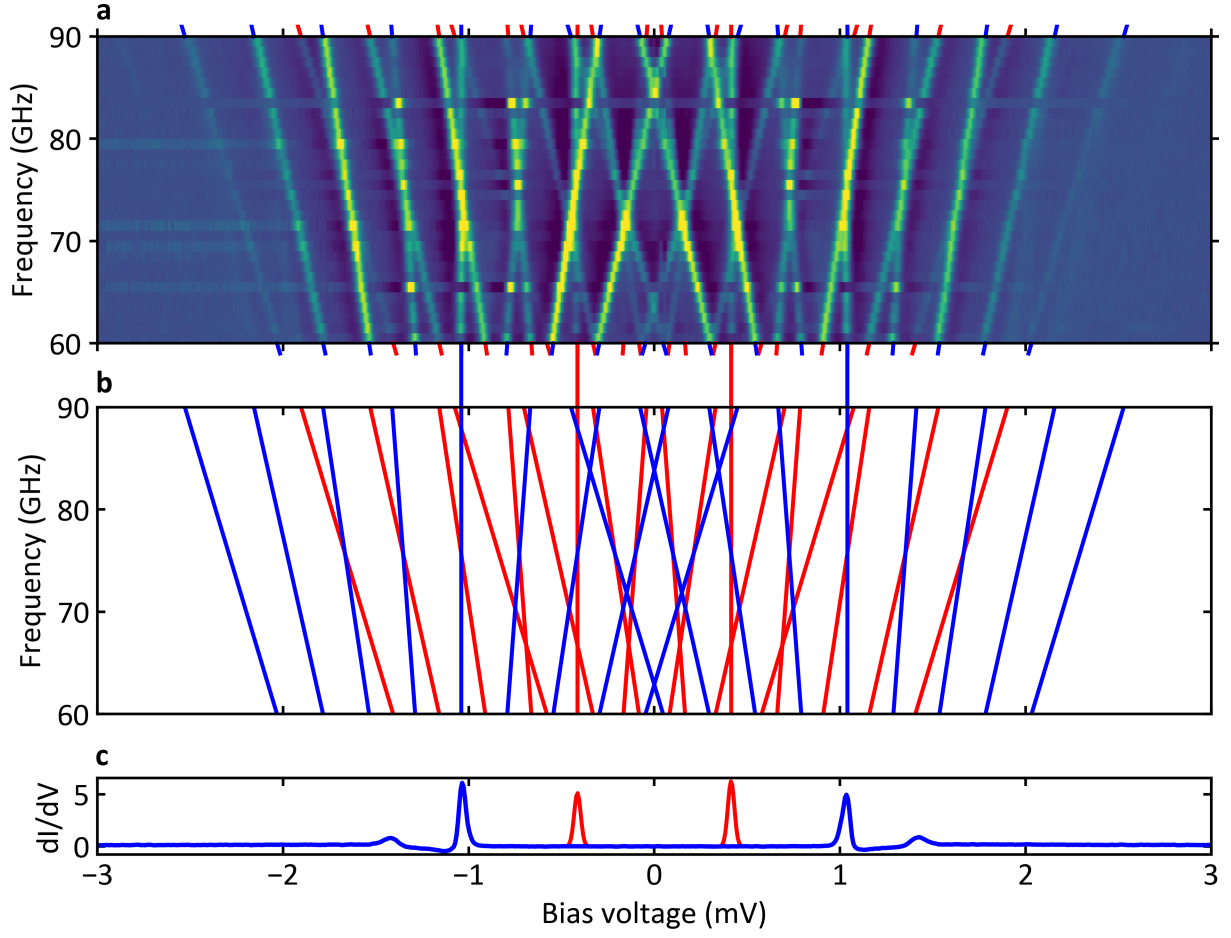


Figure 5.8: Frequency dependent RF spectra. (a) Shows the data measured at a setpoint current of 500 pA, bias voltage of 3 mV and constant dimensionless amplitude $\alpha = 3.0$. (b) shows the two families giving rise to the data in (a). (c) shows the spectrum without microwaves (in blue) and Gaussian peaks added at the zeroth order replica (in red).

Based on this data, we draw two conclusions:

1. There is a process which creates replicas of a peak which is not seen in the spectrum without microwaves.
2. Since the replicas evolve as $\hbar\omega$ (as opposed to $\hbar\omega/2$), it must be one quasiparticle tunneling or successive incoherent tunneling events.

The next subsection develops a physical picture which explains the origin of these two families.

5.4.3 Physical Picture

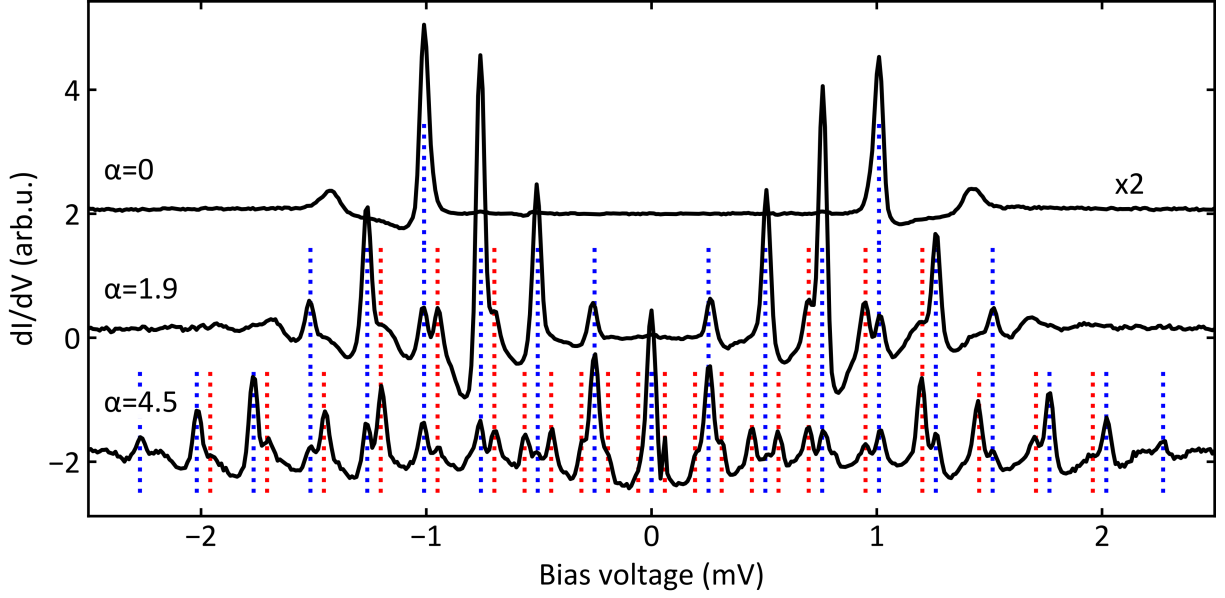


Figure 5.9: YSR spectra with microwaves. Blue dashed lines have a spacing of $\frac{\hbar\omega}{e}$ and indicate where we expect peaks from Tien-Gordon theory. The red dashed lines (also spaced by $\frac{\hbar\omega}{e}$) indicate the anomalous peaks.

As in the frequency-dependent measurement, we can now select three slices of the map in Figure 5.4 and color-code the individual peaks, located at:

- $eV = \pm(\Delta + \epsilon) \pm \hbar\omega$ (blue)
- $eV = \pm(\Delta - \epsilon) \pm \hbar\omega$ (red)

To understand the origin of the different peaks seen in Figure 5.9, we present schematics of the underlying tunneling processes in Figure 5.10.

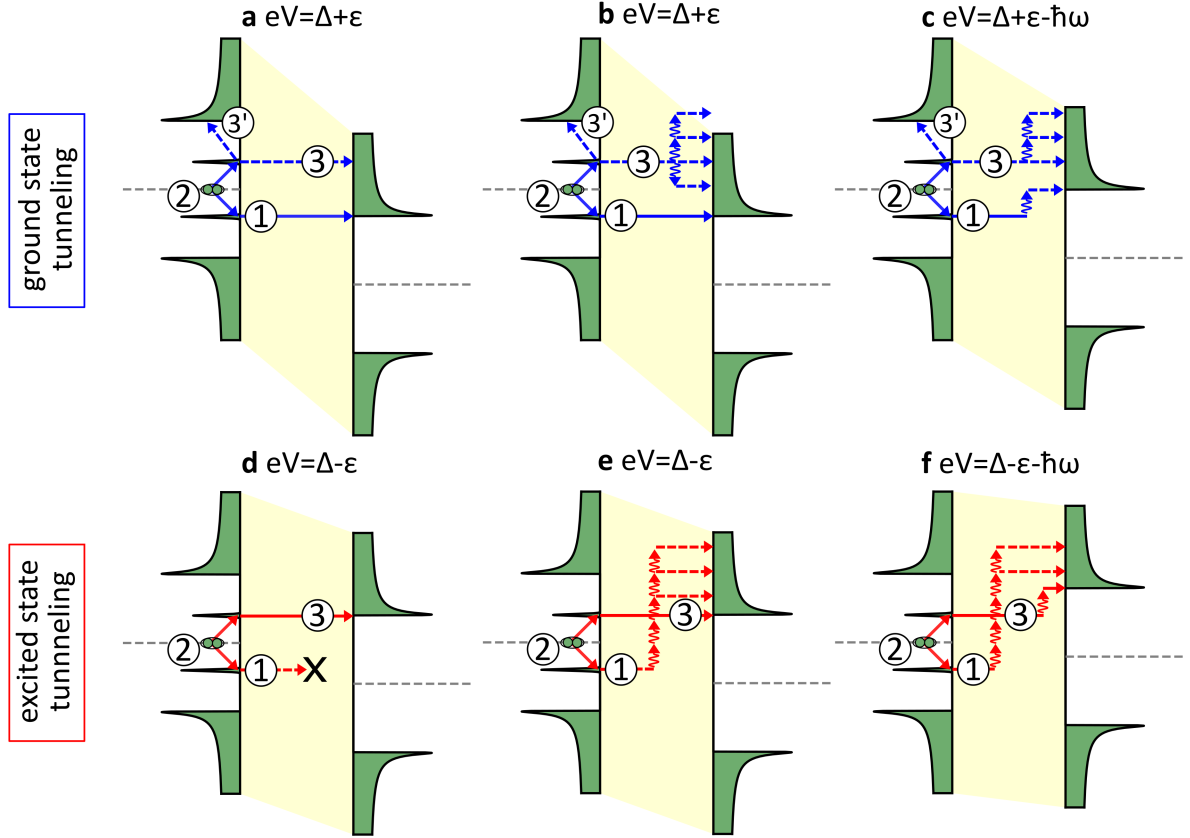


Figure 5.10: Schematic of the ground state and excited state tunneling processes. (a) shows tunneling without microwaves, where the excited YSR state can either relax by another tunneling event (indicated by ③) or into the continuum (indicated by ③'). (b) and (c) show how energy quanta can be absorbed during the relaxation process. (d) shows a forbidden process where the excited state is in resonance. With microwaves, this process is allowed, as shown in (e) and (f).

Any tunneling process involves the transfer of at least one charge from an occupied to an unoccupied state. The elementary excitations of a superconductor, i.e. Bogoliubov quasiparticles (QP), are gapped. This means that to align the occupied YSR state on the tip with the unoccupied coherence peak of the sample, we have to shift the chemical potential. We do this by applying a bias voltage of $eV = \Delta + \epsilon$ as shown in Figure 5.10(a). To understand the mechanism of YSR-BCS tunneling, we divide the process into three steps, which we illustrate using the density of states picture. While quasiparticles are a superposition of electrons and holes, this picture is still adequate with some basic precautions. In the first step (process ①), an electron tunnels across, leading to a splitting of a Cooper pair (process ②), which leaves the YSR state excited. The excess QP can then relax to the continuum (process ③') or also tunnel across the junction (process ③). This process leads to a peak indicated by a blue arrow in panel (a). At low transparencies, the relaxation into the continuum (process ③') dominates, whereas at higher conductances, the main contribution to the current comes from process ③. In Chapter 6, we

will demonstrate that the present experiments are carried out in a regime where process ③ is dominant.

The process involving a second tunneling event (process ③) can be described as a resonant Andreev process [80, 96, 151] because two charges are transferred through a real level. In contrast to that, Andreev reflections are subgap processes through a virtual level [40].

Once we switch on the microwaves, the basic tunneling events remain unchanged, except that the microwave field can lead to absorption/emission of quanta of $\hbar\omega$ during the tunneling process, as indicated by the wavy arrows in Figure 5.10(e). If quanta are absorbed during process ① (see panel (c) for example), peaks appear at $eV = \pm(\Delta + \epsilon) + n\hbar\omega$, as indicated by the dashed blue lines in Figure 5.9. The position of the replica in Figure 5.10(c) is determined by the number of energy quanta absorbed or emitted in process ①. They appear at $eV = \pm(\Delta + \epsilon) + n\hbar\omega$ in the spectrum, where n is an integer. The exchange of energy quanta during process ③ renormalizes the peak height, but does not shift the peak position in the spectrum. Other than that, the process is analogous to the tunneling without microwaves (i.e. Figure 5.10(a)). In the following, we refer to this family of peaks as *ground state tunneling*.

There is another process where the YSR state is excited and can then relax to the coherence peak of the sample. This process is shown in Figure 5.10(d). This process would occur at a bias voltage of $eV = \Delta - \epsilon$, for example due to thermal excitation. However in this experiment, the Boltzmann factor $\exp(-\frac{\epsilon}{k_B T})$ for a YSR state of energy $\epsilon = 280 \mu\text{V}$ at a temperature of 0.56 K is just 0.03 % and thermal excitation is strongly suppressed. Instead, we make this process possible by microwave excitation as shown in Figure 5.10(e). If the electron absorbs enough quanta (process ①) to reach the continuum, it can initiate a process where the relaxation ③ is in resonance with the coherence peak of the sample. If quanta are absorbed during process ③ (see panel (f) for example), this leads to the family of peaks marked by the red dashed lines in Figure 5.9, at bias voltages $eV = \pm(\Delta - \epsilon) + n\hbar\omega$. All the peaks of this family have in common that the excited state is in resonance with the coherence peak modulo an integer number of energy quanta $\hbar\omega$, prompting us to call these processes *excited state tunneling (EST)*.

It should be noted that the observation of a new family of peaks is entirely due to the way tunneling with YSR states works. For example, in similar experiments with free electrons [152] or superconducting point contacts [153], this effect cannot be seen. Additionally, one would require a microwave frequency $\hbar\omega > \Delta + \epsilon$ to excite the YSR state on its own. The tunneling junction makes an excitation possible below this threshold.

To draw a connection to related work [23, 80, 96], we note that an electron travelling forwards is equivalent to an hole tunneling backwards. This equivalence is shown in Figure 5.11 and in the end, these are just two different representations of the same picture. We choose the electron picture here to emphasize the sequential nature of this tunneling process.

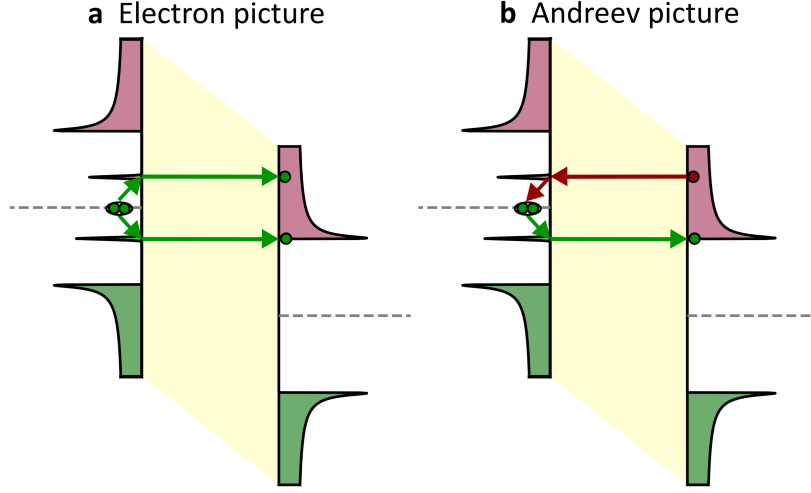


Figure 5.11: Comparison of the electron and Andreev picture. (a) represents the process as two electrons tunneling forwards, whereas in (b), one hole is reflected as an electron.

5.5 Derivation of a Modified Tien-Gordon Equation

5.5.1 Full Green's Function Approach

We follow the approach presented by Cuevas *et al* [154] which relies on a full Green's function theory. In particular, this theory calculates the Fourier components I_n^m , where:

$$I(t) = \sum_{n,m} I_n^m \exp [i (n\phi_0 + 2neVt/\hbar + m\omega t)], \quad (5.2)$$

These components can be calculated from a T -matrix approach, where terms like $\hat{T}_{RL,ij}^{kl,a}$ satisfy a set of algebraic equations. Here $\hat{T}_{nm}^{kl}(E) \equiv \hat{T}(E + neV + k\hbar\omega, E + meV + l\hbar\omega_r)$, R and L denote the right and left electrode and the index a (r) refers to the advanced (retarded) Green's function. This then gives [154]:

$$I_n^m = \frac{e}{h} \int dE \sum_{i,k} \text{Tr} \left[\hat{\tau}_3 \left(\hat{T}_{LR,0i}^{rk} \hat{g}_{R,i}^{+-} \hat{T}_{RL,in}^{km} \hat{g}_{L,n}^a - \hat{g}_{L,0}^r \hat{T}_{LR,0i}^{rk} \hat{g}_{R,i}^{+-} \hat{T}_{RL,in}^{km} \right. \right. \\ \left. \left. + \hat{g}_{R,0}^r \hat{T}_{RL,0i}^{rk} \hat{g}_{L,i}^{+-} \hat{T}_{LR,in}^{km} - \hat{T}_{RL,0i}^{rk} \hat{g}_{L,i}^{+-} \hat{T}_{LR,in}^{km} \hat{g}_{R,n}^a \right) \right] \quad (5.3)$$

This can be extended to a YSR state simply by changing the Green's function of one of the electrodes. However, the parameters must be carefully chosen to match the experimental conditions. Too low microwave energy, too low lifetime or commensurate frequencies could lead to the anomalous peaks being overlooked. One key consideration for the peak shape

is the competition between Gaussian broadening and Dynes broadening [66]. We include the broadening parameter σ as a phenomenological parameter to model external noise which according to the central limit theorem can be approximated by a Gaussian distribution [155]:

$$f_\sigma(V) = \frac{1}{\sqrt{2\pi\sigma^2}} e^{-\frac{1}{2} \frac{V^2}{\sigma^2}} \quad (5.4)$$

In contrast to that, the Dynes parameter η is related to the lifetime of quasiparticles [66]. Figure 5.12(a) shows the effect of increasing the Dynes parameter η while keeping the Gaussian broadening constant. It can be seen that at higher η the peak becomes more asymmetric. Therefore, if we try to compensate for the higher η by reducing the Gaussian broadening σ as shown in panel (b), we see two main differences in the peaks:

1. The shoulder at low bias voltage is more pronounced for high η .
2. The dip with negative differential conductance is stronger at high η if we choose σ to match the peak height in the positive differential conductance.

Based on these two observations, the shape of the peak measured in experiment gives information about the relation of η and σ , whereas the width is the result of a combination of η and σ .

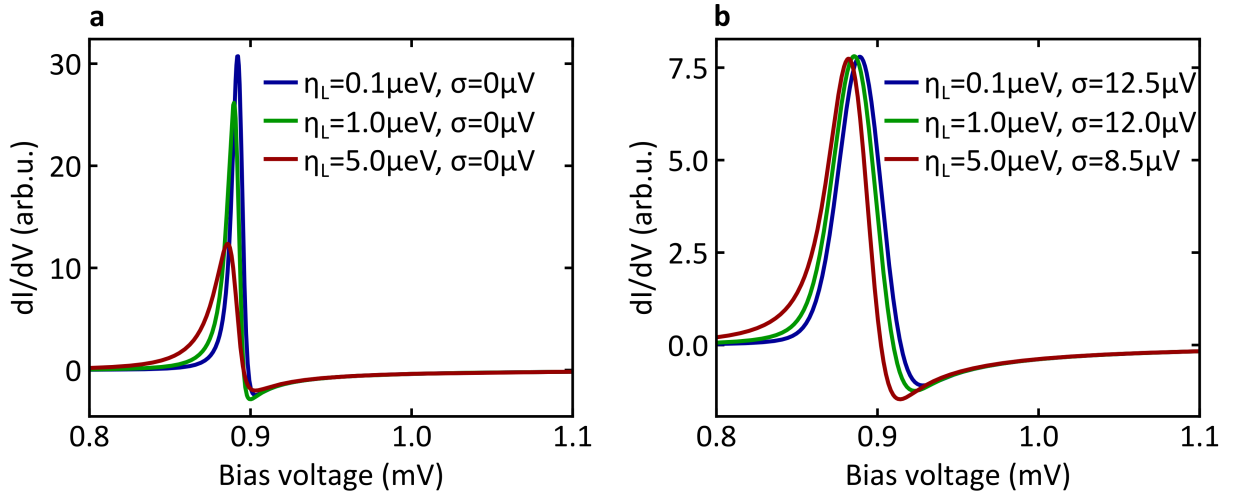


Figure 5.12: Comparison of Gaussian and Dynes broadening. The parameters are (in meV): $\Delta_L = 0.724$, $\Delta_R = 0.59$, $J = 75.5$, $U = 0$, $\Gamma_R = 100$, $\Gamma_L = 0.04$, $\eta_R = 10^{-4}$. (a) is a spectrum without Gaussian broadening. (b) shows the same results convolved with a Gaussian chosen such that all three spectra have the same peak height.

In general, we first fit the spectrum without microwaves to determine the key parameters (see Section 6.1 for a detailed description). Based on that, the spectrum under microwave irradiation can be calculated without introducing any new parameters if the dimensionless amplitude α is known. Figure 5.13(a) shows such a spectrum for a YSR state. We can define the transmission

as the sum of the transmission through the YSR channel τ_{YSR} and the BCS channel τ_{BCS} . Using the parameters J , Γ_S , Γ_T from the Anderson impurity model and a percentage p we can write [81]:

$$\tau = \tau_{\text{YSR}} + \tau_{\text{BCS}} = p \frac{4\Gamma_S\Gamma_T}{(\Gamma_S + \Gamma_T)^2 + J^2} + (1 - p) \frac{4\Gamma_S\Gamma_T}{(\Gamma_S + \Gamma_T)^2} \quad (5.5)$$

In the data presented here, $p = 0.88$. We apply regular Tien-Gordon theory to the coherence peak of the BCS channel. For higher conductances, this approximation breaks down due to Andreev reflections between the superconductors and Andreev reflections from the YSR state to the superconductor and then into the BCS channel of the tip. Figure 5.13(b) compares the model with the data when the microwave is switched on and shows excellent agreement.

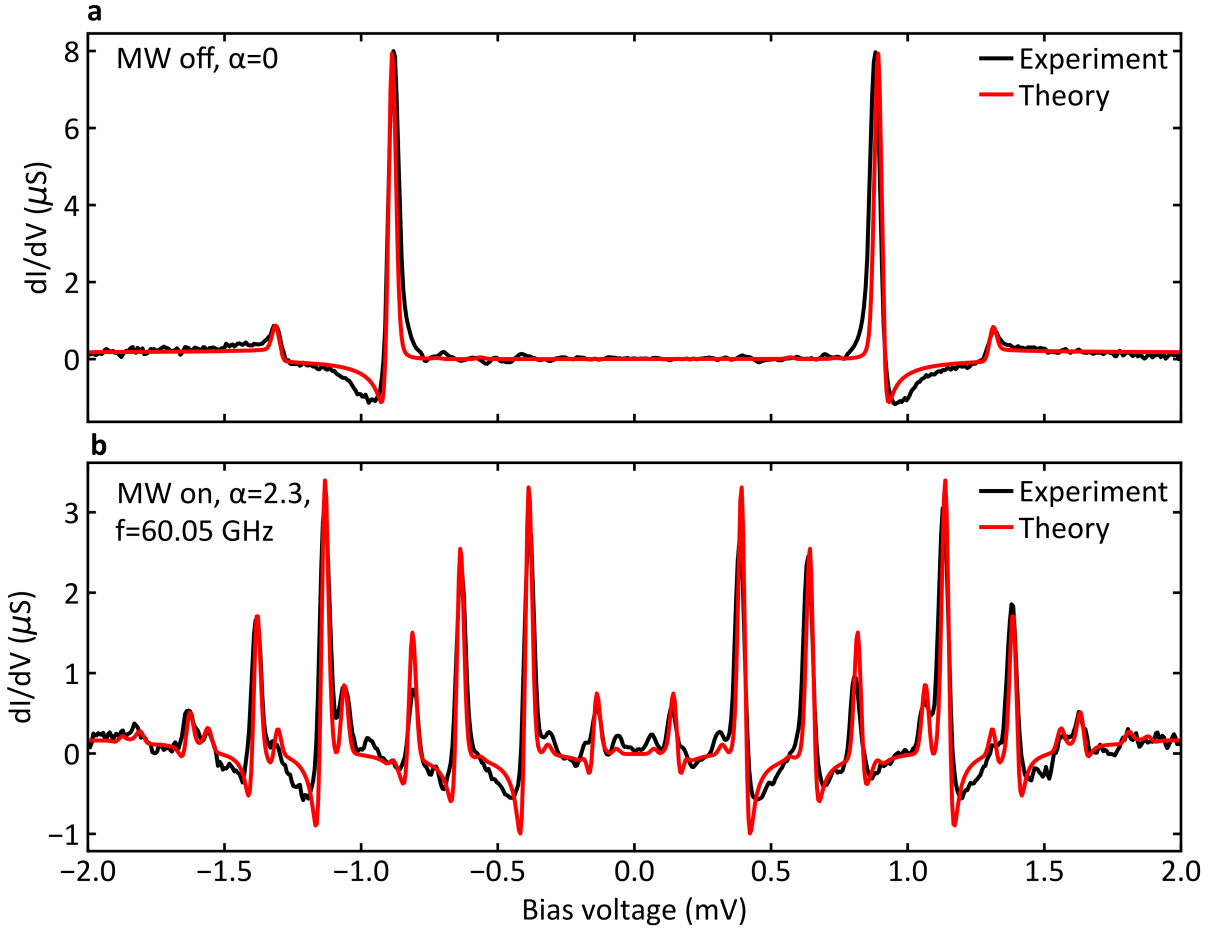


Figure 5.13: Fitting using the full approach. The parameters are (in meV) $\Delta_L = 0.73$, $\Delta_R = 0.59$, $J = 75.5$, $U = 0$, $\Gamma_S = 100$, $\eta_{L,R} = 10^{-4}$, $\sigma_{\text{Gauss}} = 12.5 \times 10^{-3}$ with conductances: $\tau_{\text{YSR}} = 1.7 \times 10^{-3}$, $\tau_{\text{BCS}} = 3.7 \times 10^{-4}$. (a) shows the spectrum without microwaves. (b) shows the spectrum with microwaves at amplitude $\alpha = 2.3$ and frequency 60.05 GHz.

Once the correct parameters are determined, we can also model the microwave-dependent data presented in section 5.3. It should be noted that false color plots can easily hide deviations in the color scale such that individual spectra as in Figure 5.13 give a better estimate of the quality

of the fit. Once these fits are available, the dimensionless amplitude α may be varied to create a false color plot. Figure 5.14(a) shows experimental data measured at a setpoint current of 500 pA and a bias voltage of 5 mV. We sweep the microwave amplitude α while keeping the frequency constant at $f = 60.45$ GHz. Panel (b) shows the fit using the full model. All the replicas seen in experiment are reproduced by the model.

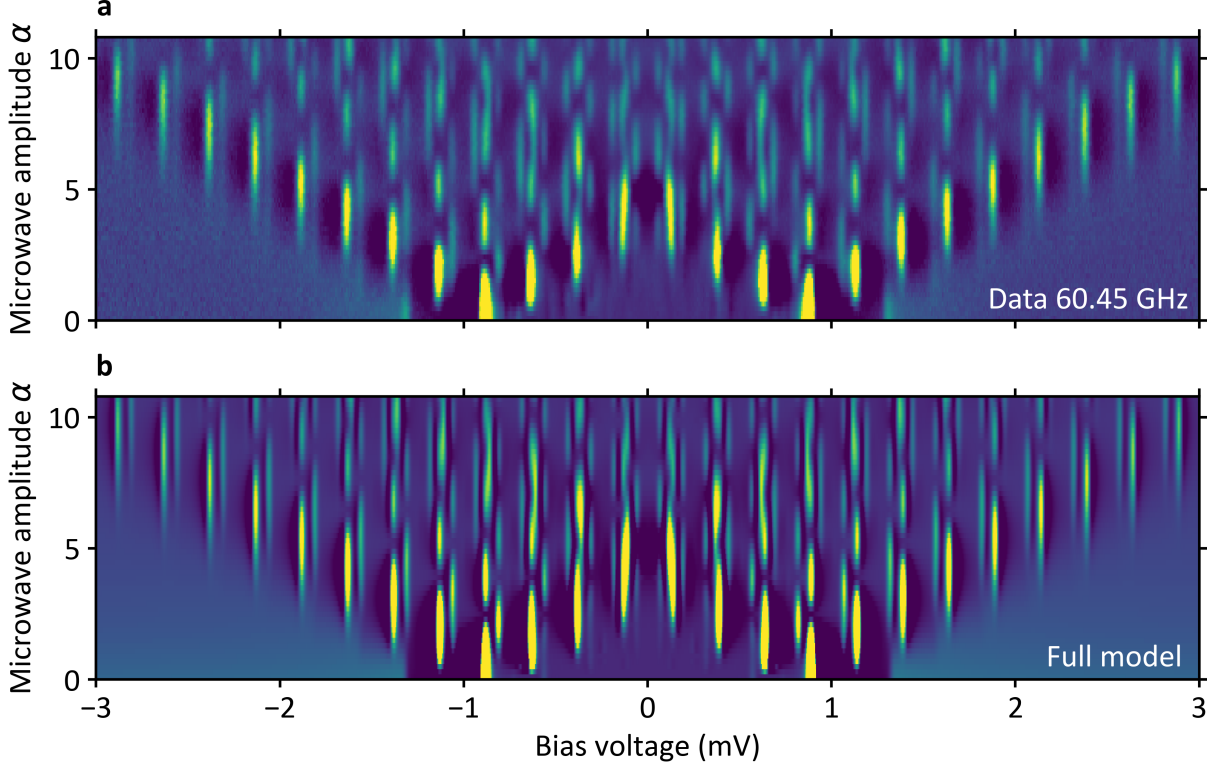


Figure 5.14: Fitting of amplitude-dependent maps. The parameters are: $\Delta_L = 0.73$, $\Delta_R = 0.59$, $J = 75.5$, $U = 0$, $\Gamma_S = 100$, $\eta_{L,R} = 10^{-4}$, $\sigma_{\text{Gauss}} = 12.5 \times 10^{-3}$ with conductance $\tau_{\text{YSR}} = 1.0 \times 10^{-3}$. (a) displays the experimental data measured at a setpoint of 5 mV and 500 pA. (b) shows the simulated false color plot.

Finally, we can also model the frequency-dependent measurements. Figure 5.15(a) shows another set of data with frequency dependent measurements where we kept the microwave amplitude constant at $\alpha = 2.8$ by compensating for the transfer function. Panel (b) shows the corresponding modeling using the Green's function code to first order. All the replicas seen in experiment are reproduced, albeit with slightly different peak amplitudes. Panel (c) shows the harp-like arrangement of the peak positions and panel (d) shows the original spectrum (without microwaves) with EST peaks at $\Delta - \epsilon$ added by hand.

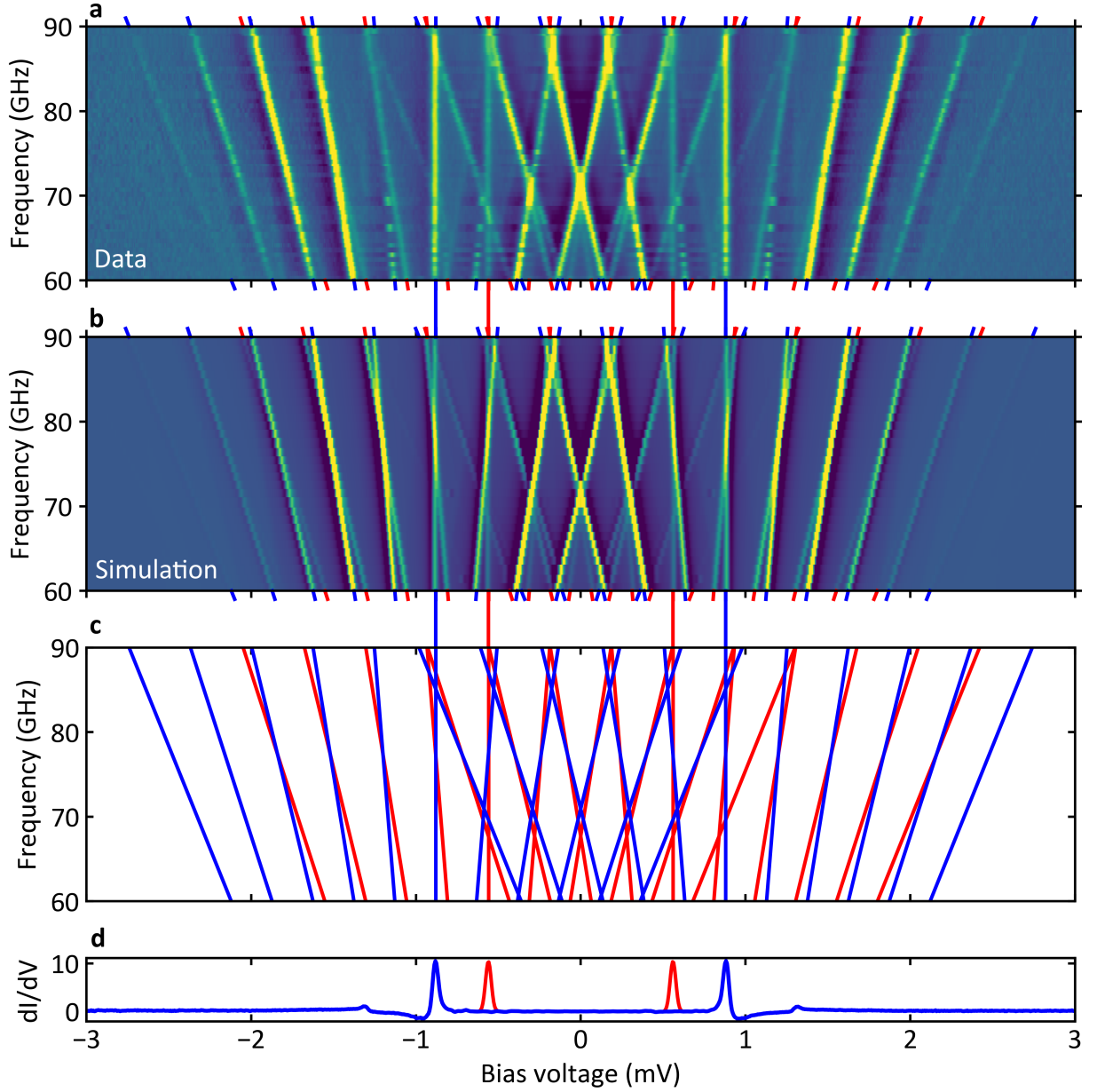


Figure 5.15: Modelling the frequency-dependent measurements. (a) shows the experimental data measured at a setpoint of 500 pA and bias voltage of 3 mV with constant RF amplitude set to $\alpha = 2.8$. (b) shows the corresponding fit. The parameters are: $\Delta_L = 0.73$, $\Delta_R = 0.59$, $J = 75.5$, $U = 0$, $\Gamma_S = 100$, $\eta_{L,R} = 10^{-4}$, $\sigma_{\text{Gauss}} = 12.5 \times 10^{-3}$ with conductance $\tau_{\text{YSR}} = 1.7 \times 10^{-3}$. (c) shows the expected location of the peaks and (d) shows the spectrum without microwave with added EST peaks in red.

In summary, we see that the Green's function approach predicts the formation of anomalous peaks as observed in section 5.3. In particular, the model can be used to fit individual spectra, amplitude-dependent maps, or frequency-dependent maps.

5.5.2 Simplified Model

Frequently, the full theory is not required and it turns out that the key properties of the experimental results are covered by a lowest order approximation. Starting from the lowest order term for the Andreev current, we can make further approximations to quantify the physical picture developed in subsection 5.4.3.

Consider the following equation which has been derived from the full theory [154] by Juan Carlos Cuevas. Here I_{AR} refers to the term corresponding to the Andreev process and $\Gamma_{e,h}$ are hole and electron parts of the density of states:

$$I_{\text{AR}} \approx \frac{2e}{h} \sum_{k,l} J_k^2(\alpha) J_l^2(\alpha) \times \int_{-\infty}^{\infty} \frac{\Gamma_e(E - eV - k\hbar\omega) \Gamma_h(E + eV + l\hbar\omega)}{(E - \epsilon)^2 + \eta_S^2} \times \\ \times [f(E - eV - k\hbar\omega) - f(E + eV + l\hbar\omega)] dE. \quad (5.6)$$

In the following, we will derive a simplified model to highlight the roles of the replicas in step ① and step ③ of ground state and excited state tunneling (see Figure 5.10). We simplify the tunneling and focus on the interplay of the Bessel functions and exchange of energy quanta. We start with equation 5.6. In the case of long-lived YSR states, i.e. very small η_S , we can approximate the Lorentzian of the YSR state by a Dirac delta-function $\frac{1}{(E - \epsilon)^2 + \eta_S^2} \approx \frac{\pi}{\eta_S} \delta(E - \epsilon)$. This step solves the integral in equation 5.6 and the Andreev current becomes:

$$I_{\text{AR}} \approx \frac{e}{\hbar\eta_S} \sum_{k,l} J_k^2(\alpha) J_l^2(\alpha) \Gamma_e(\epsilon - eV - k\hbar\omega_r) \Gamma_h(\epsilon + eV + l\hbar\omega_r) \\ \times [f(\epsilon - eV - k\hbar\omega_r) - f(\epsilon + eV + l\hbar\omega_r)] \quad (5.7)$$

Each tunneling rate $\Gamma_{e,h}$ has two peaks at $\pm\Delta$, such that we have a total of four peaks in the spectrum. To separate out these peaks, we use the Heaviside step function $\theta(E)$ to define $\Gamma_{e,h}^{\pm}(E) = \theta(\pm E) \Gamma_{e,h}(E)$ so that we can split $\Gamma_{e,h}(E)$ into:

$$\Gamma_{e,h}(E) = \Gamma_{e,h}^+(E) + \Gamma_{e,h}^-(E). \quad (5.8)$$

Without microwaves, the four principal peaks correspond to two ground state and two excited state tunneling peaks at $eV = \pm(\Delta + \epsilon)$ and $eV = \pm(\Delta - \epsilon)$, respectively. The derivations for all of these four peaks are very similar, so that in the following we derive the behavior for one peak, which can be easily extended to the other peaks.

Derivation for the Excited State Tunneling Electron Peak

These peaks are located at bias voltages of $eV = -(\Delta - \epsilon) - k\hbar\omega_r$, i.e. at the bias voltage where $\Gamma_e^+(E)$ is resonant. We assume that $k_B T \ll \epsilon$, such that the Fermi function can be approximated by a step function. In order to observe this peak, the following conditions have to be fulfilled:

1. The tunneling rate $\Gamma_e^+(E)$ is resonant, i.e. $eV = -(\Delta - \epsilon) - k\hbar\omega_r$
2. The other tunneling rate $\Gamma_h(E)$ is nonzero, i.e. $|\epsilon + eV + l\hbar\omega_r| > \Delta$.
3. The difference in Fermi functions is nonzero, i.e. $|f(\epsilon - eV - k\hbar\omega_r) - f(\epsilon + eV + l\hbar\omega_r)| = 1$.

Combining the first condition with the other two conditions yields:

$$k > \frac{2\epsilon}{\hbar\omega_r} + l \quad (5.9)$$

Owing to the second condition, we approximate $\Gamma_h(E)$ by a constant, i.e. $\langle \Gamma_h \rangle = \Gamma_h(E \gg \Delta)$. Applying these conditions to equation 5.7, we find for the excited state electron tunneling current:

$$I_{\text{ex,e}}(V) = -\frac{e}{\hbar\eta_S} \sum_{l=-\infty}^{\infty} \sum_{k > \frac{2\epsilon}{\hbar\omega_r} + l} J_k^2(\alpha) J_l^2(\alpha) \Gamma_e^+(\epsilon - eV - k\hbar\omega_r) \langle \Gamma_h \rangle \quad (5.10)$$

In analogy to the Tien-Gordon model, we define a bare tunneling current which does not involve the modulation by the microwaves $I_{\text{ex,e}}^0(V) = -\frac{e}{\eta_S \hbar} \langle \Gamma_h \rangle \Gamma_e^+(\epsilon - eV)$. Equation 5.10 simplifies to:

$$I_{\text{ex,e}}(V) = \sum_k w(\alpha, k) J_k^2(\alpha) I_{\text{ex,e}}^0(V + k\hbar\omega_r/e), \quad (5.11)$$

where we have defined the weight function $w(\alpha, k)$ as:

$$w(\alpha, k) = \sum_{m > m_0 - k} J_m^2(\alpha) \quad (5.12)$$

and where $m_0 = \lceil \frac{2\epsilon}{\hbar\omega} \rceil$, where $\lceil \cdot \rceil$ is the ceiling function ($\lceil x \rceil$ is defined as x rounded to the next larger integer). The weight function does not change the position nor the number of the replicas. It only modifies the amplitude of the peak. This nicely explains the appearance of replica at integer multiples of $\hbar\omega/e$ instead of $\hbar\omega/2e$. The weight function also introduces a threshold through the condition $m > m_0 - k$, which means that m_0 quanta of $\hbar\omega$ have to be absorbed from the microwave in order to excite the YSR state. The leading edge of the weight function determining the onset of the peak as function of microwave intensity is given by the lowest order Bessel function $J_{m_0-k}^2(\alpha)$. This means in particular that the bare tunneling current $I_{\text{ex,e}}^0(V)$ as defined above cannot be observed when the microwave is turned off.

Simplified Tunneling Equations for Ground State and Excited State Tunneling

We can straightforwardly extend the above derivation for all four peaks. We find for the bare tunneling currents:

$$I_{\text{ex,e}}^0(V) = -\frac{e}{\eta_s \hbar} \Gamma_e^+ (\epsilon - eV) \langle \Gamma_h \rangle, \quad (5.13)$$

$$I_{\text{ex,h}}^0(V) = +\frac{e}{\eta_s \hbar} \langle \Gamma_e \rangle \Gamma_h^+ (\epsilon + eV), \quad (5.14)$$

$$I_{\text{gr,e}}^0(V) = +\frac{e}{\eta_s \hbar} \Gamma_e^- (\epsilon - eV) \langle \Gamma_h \rangle, \quad (5.15)$$

$$I_{\text{gr,h}}^0(V) = -\frac{e}{\eta_s \hbar} \langle \Gamma_e \rangle \Gamma_h^- (\epsilon + eV), \quad (5.16)$$

where the first index (gr,ex) refers to ground state and excited state tunneling and the second index (e,h) refers to electron and hole tunneling, respectively. From these bare tunneling currents, which have one peak each, we find the following equations to calculate the spectra with microwaves:

$$I_{\text{ex,e}}(V) \approx \sum_k w(\alpha, k) J_k^2(\alpha) I_{\text{ex,e}}^0(V + k\hbar\omega_r/e), \quad (5.17)$$

$$I_{\text{ex,h}}(V) \approx \sum_k w(\alpha, k) J_k^2(\alpha) I_{\text{ex,h}}^0(V - k\hbar\omega_r/e), \quad (5.18)$$

$$I_{\text{gr,e}}(V) \approx \sum_k \tilde{w}(\alpha, k) J_k^2(\alpha) I_{\text{gr,e}}^0(V - k\hbar\omega_r/e), \quad (5.19)$$

$$I_{\text{gr,h}}(V) \approx \sum_k \tilde{w}(\alpha, k) J_k^2(\alpha) I_{\text{gr,h}}^0(V + k\hbar\omega_r/e), \quad (5.20)$$

where the weight functions are defined as:

$$w(\alpha, k) = \sum_{m \geq m_0 - k} J_m^2(\alpha) \quad (5.21)$$

$$\tilde{w}(\alpha, k) = \sum_{m \geq -m_0 - k} J_m^2(\alpha). \quad (5.22)$$

where $m_0 = \left\lceil \frac{2\epsilon}{\hbar\omega_r} \right\rceil$ is the minimum number of quanta needed to excite the YSR state. Interestingly, we find that for ground state tunneling the weight function $\tilde{w}(\alpha, k)$ does not impose a threshold for the activation of the tunneling process, because the condition $m \geq -m_0$ (for $k = 0$) always includes the zeroth order Bessel function, such that resonant Andreev processes are always possible without microwaves as has been discussed before [76].

Figure 5.16 illustrates how this modelling can be performed in practice:

1. Take the base spectrum and add peaks at $\pm(\Delta - \epsilon)$ (panel (a)).
2. Apply the Tien-Gordon equation to this spectrum. Inside the grey region, there are replicas which are forbidden because of the weight function (panel (b)).

3. Apply the appropriate weight function for each of the peaks. The color map now looks very similar to the experiment (panel (c)).
4. Different contributions can now be disentangled and color coded (panel (d)).

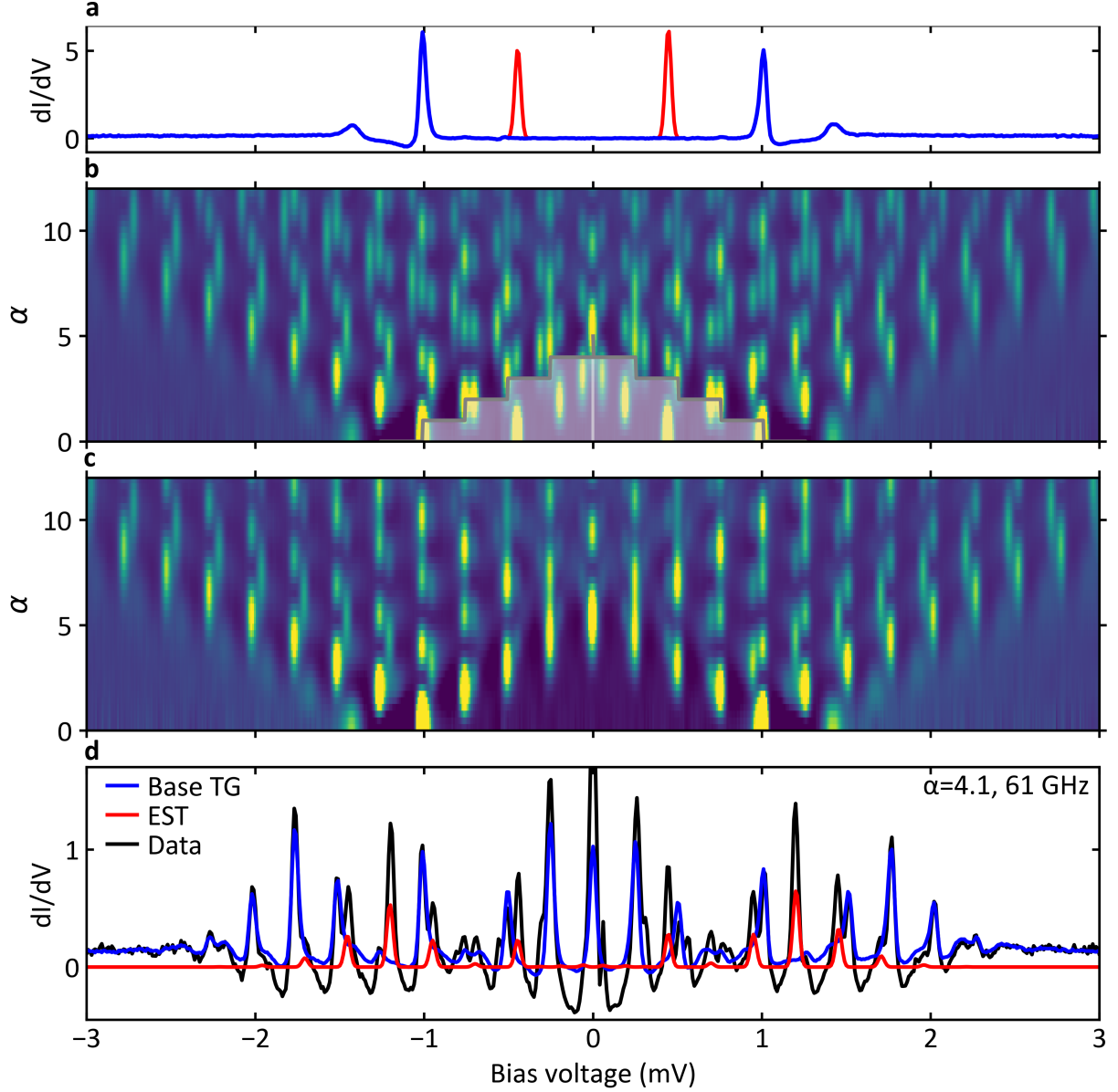


Figure 5.16: Illustration of the algorithm related to the modified TG equation. (a) shows the original spectrum (blue) with peaks at $\Delta - \epsilon$ added by hand (red). (b) shows the TG spectrum without the weight function and (c) shows the spectrum when the weight function is included. (d) shows the data in black and the contribution due to ground state tunneling (blue) as well as the contribution from excited state tunneling (red – labelled EST).

The leading edge of the threshold function is in general defined by the first Bessel function in the

sum (equation 5.21), i.e. $J_{m_0}(\alpha)$, leading to the grey region shown in Figure 5.17. In panel (a), we show a calculation based on the simplified model. We pick three slices, namely $n = -1, 0, 1$ and compare this modelling with the experimental data shown in Figure 5.4. Panel (b) shows the corresponding weight function $w(\alpha, n)$. Panel (c) shows firstly the bare Tien-Gordon result without the weight function (i.e. Figure 5.16(b)) in a grey dashed lines. Once the weight function is included (grey solid line), there is excellent agreement with the experimental data. In particular, if we consider the $n = 1$ line, we see that the expected peak is cut off right in the middle due to the threshold function.

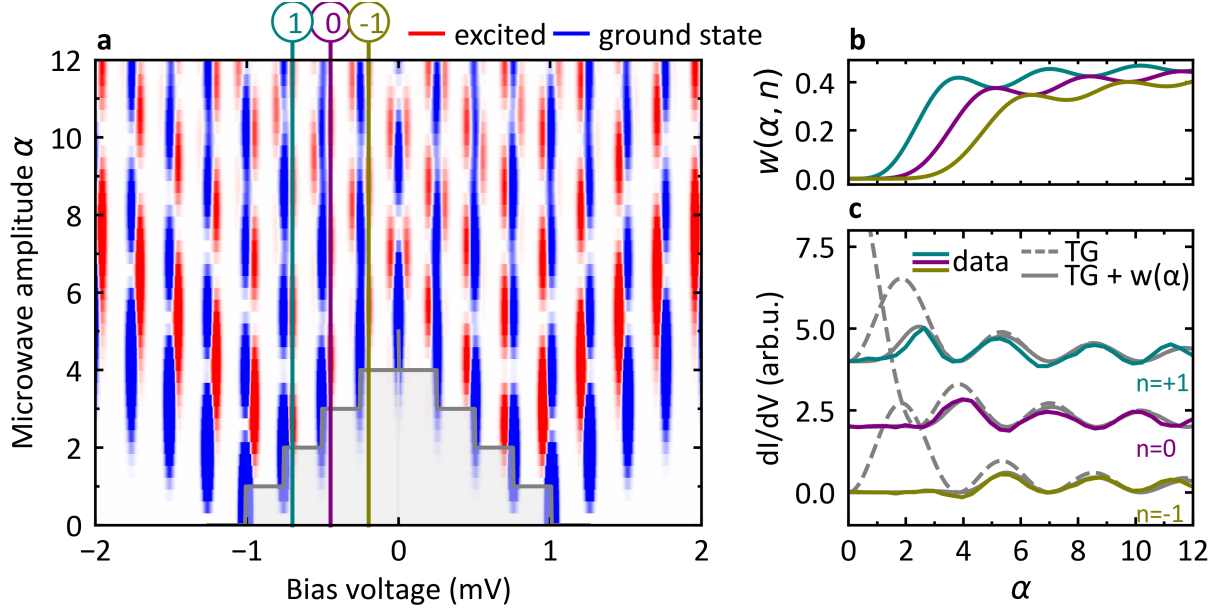


Figure 5.17: Analysis of the evolution of excited state tunneling with the dimensionless amplitude α . (a) shows a color coded fan calculated with the simplified model. For color coding, the sign of the excited state tunneling peaks has been inverted. (b) shows the weight function for $n = -1, 0, 1$. (c) shows the data at selected bias voltages in (a) along with the expected TG behavior (grey dashed) and the TG behavior including a weight function (grey solid).

We conclude this chapter by presenting the experimental data once again in Figure 5.18(a). Panel (b) shows the simulation using the simplified model. For visibility, we color code the replicas corresponding to *excited state tunneling* in red and the replicas of *ground state tunneling* in blue. The weight function imposes an additional constraint which is most visible in the region marked in grey. The staircase marks the amplitude where enough microwave quanta can be observed to make *excited state tunneling* possible. As with normal Tien-Gordon theory [116], this cut-off is not sharp, indicating, as elucidated in Section 2.8, that we are dealing with a quantum process and there is a smooth decay into the classically forbidden region.

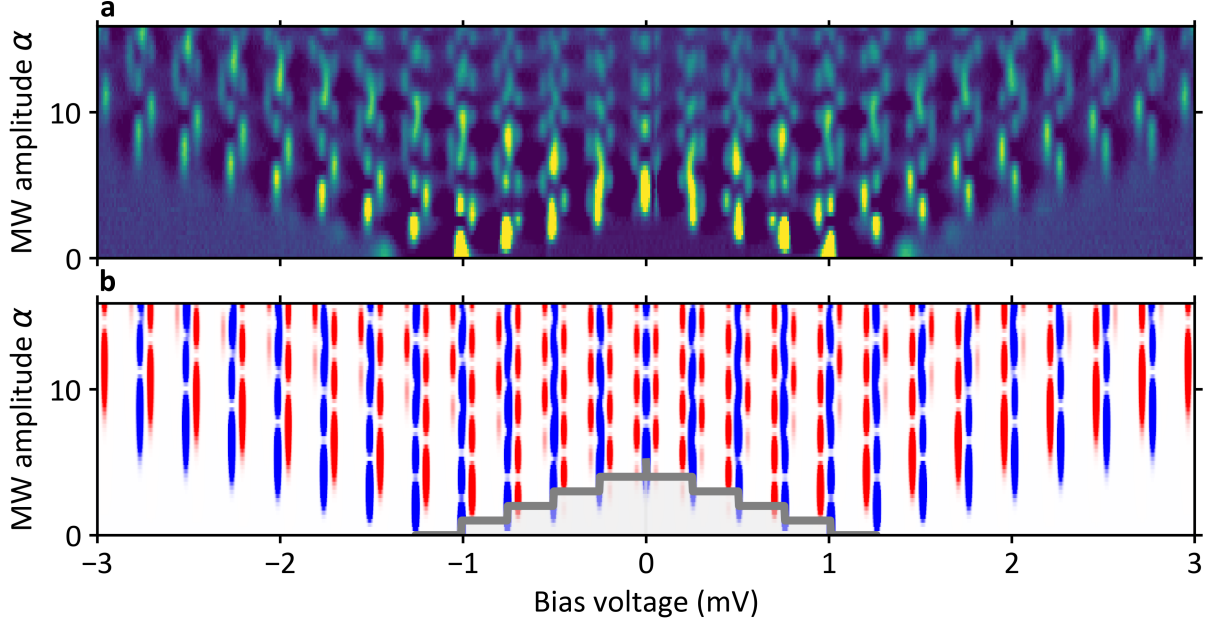


Figure 5.18: Color coding of experimental data. (a) presents the data measured at 61 GHz and (b) shows the simplified modeling with the region where the threshold function is active being marked in grey.

5.6 Outlook

This chapter presented the observation of a family of peaks seen in microwave-assisted tunneling in a YSR-BCS junction. We developed a simple physical picture explaining the process which we label as *excited state tunneling* in terms of a two-electron process. In this process, the microwaves excite the YSR state to the continuum and its relaxation is in resonance.

The height of the peaks corresponding to excited state tunneling is strongly dependent on the lifetime of the YSR state. The following chapter analyzes the dependence on the conductance τ and the lifetime $\propto \eta^{-1}$ in detail. However, such an analysis can only give information about the associated lifetimes indirectly. Pulse schemes would provide a direct measurement of this process. As a first attempt, we apply pulses to a YSR state using the in-built pulse function of the signal generator. We expect that for some critical pulse length τ_c , which has the same order of magnitude as the lifetime of the YSR state, the system should behave differently, similar to experiments on stochastic resonance [49], where a synchronization of the system with the drive leads to an increase in current. For long pulse times $\tau \gg \tau_c$, the YSR state can relax many times within one cycle, which means that effectively, the resulting spectrum is a superposition of the spectra when the microwaves are on and when the microwaves are off. The overall spectrum is just the sum, i.e. if the pulse period is T and the time the microwave is switched on is τ , then

the resulting spectrum is just the classical result:

$$I'_{\text{pulse}}(V) = \frac{\tau}{T} I'_{\text{MWon}}(V) + \frac{T - \tau}{T} I'_{\text{MWoff}}(V) \quad (5.23)$$

Here, $I'_{\text{MWon}}(V)$ and $I'_{\text{MWoff}}(V)$ are the spectra obtained when the microwaves are switched on or off, respectively, in continuous wave mode. On the other hand, when $\tau \ll \tau_c$, the system has no time to relax and the resulting spectrum will just be the spectrum without microwaves. Finally, when the pulse length is comparable to the lifetime of the YSR state – or more precisely, one tunneling cycle of the YSR state – then one might expect some synchronization effects, although the exact details will be the subject of further experimental and theoretical studies.

In experiment, the frequency extension module limits the pulse duration to a minimum of 140 ns. Below that, it acts as a filter and no radiation is transmitted to the junction. Figure 5.19 shows the measurement and this minimal pulse duration. First we measure the curves with microwaves off (blue line) and microwaves on (red line). Then we apply the pulses (green line). We see that the result obeys exactly the relationship in equation 5.23, which means that the pulses are still too long, i.e., that the lifetime of the YSR state is likely lower than 140 ns. We aim to find new methods of applying shorter pulses to possibly tune the pulse length to the lifetime of the YSR state.

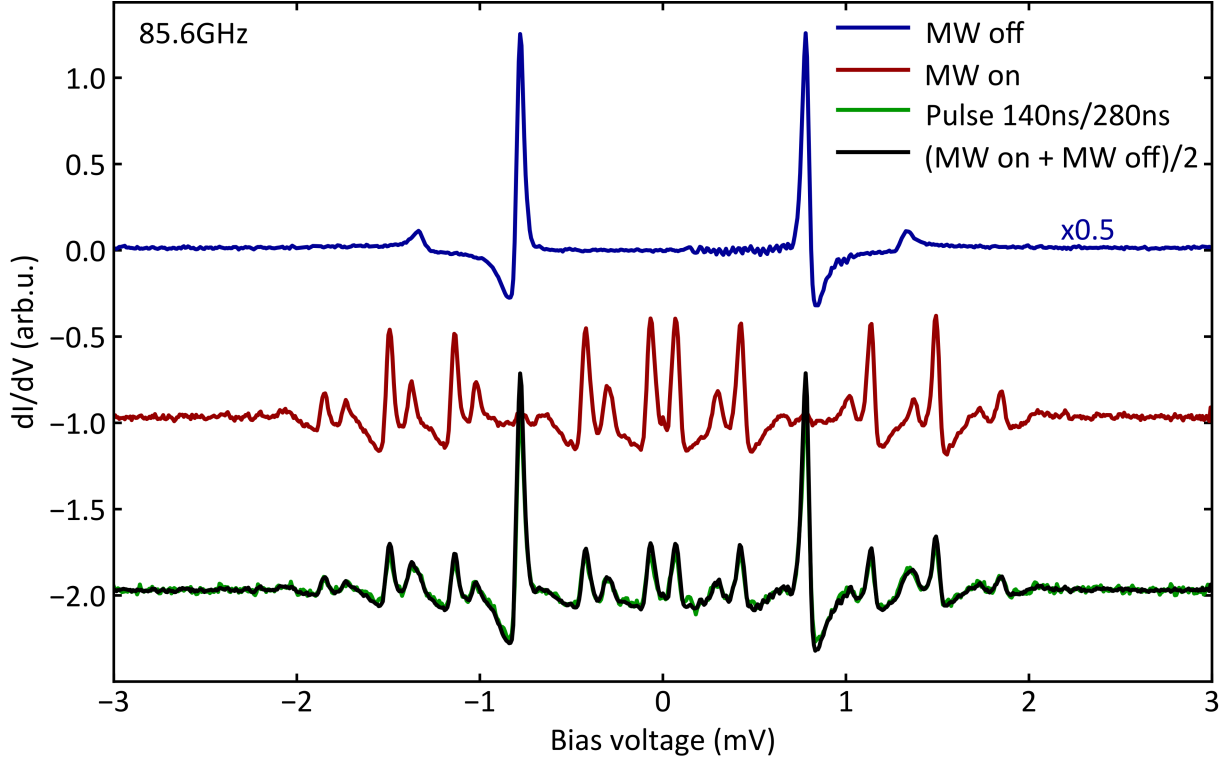


Figure 5.19: Spectra with pulsed microwaves. The curves are offset vertically for clarity. The blue spectrum shows a YSR state on the tip without microwaves. The red spectrum shows the measurement at 85 GHz and $\alpha = 3$. The green line shows the result of pulsing the microwaves with a period of 280 ns and a length of 140 ns. The black lines shows the sum of the blue and red line divided by two.

Apart from just pulsing the microwave signal, true pump-probe schemes [53] could be used to directly measure the lifetime of YSR states. This is the subject of further projects.

6

Modeling the Conductance Dependence

The results of this chapter will be published in paper # 1 of the publication list.

Having presented experimental data, mostly at constant transparency τ , the next logical step is to analyse how these observations vary with conductance. This is particularly important because in the modelling, we portray excited state tunneling (EST) as a two-electron process. This means that the height of the EST peaks should grow with the square of the conductance. We start by examining the effect of the lifetime on the height of peaks in the spectrum and find that EST peaks are particularly pronounced for long lifetimes. Then we compare various approximations with the full code to estimate at which transparencies τ these approximations are valid. Finally we show conductance-dependent data with corresponding fits and conclude that the early onset of resonances in microwave-assisted tunneling leads to a complex evolution of the peak heights, which needs to be treated with the full model.

6.1 Model and Parameters

The model for microwave-assisted tunneling has been developed by Juan Carlos Cuevas who also provided the FORTRAN code for the calculations presented here. The model is based on the theory of subsection 5.5.1. As a technical detail, the coupling is placed into a renormalization of the tunneling element. This gives a recursive algorithm calculating the higher order contributions step by step. The main parameters are presented in Figure 6.1(a).

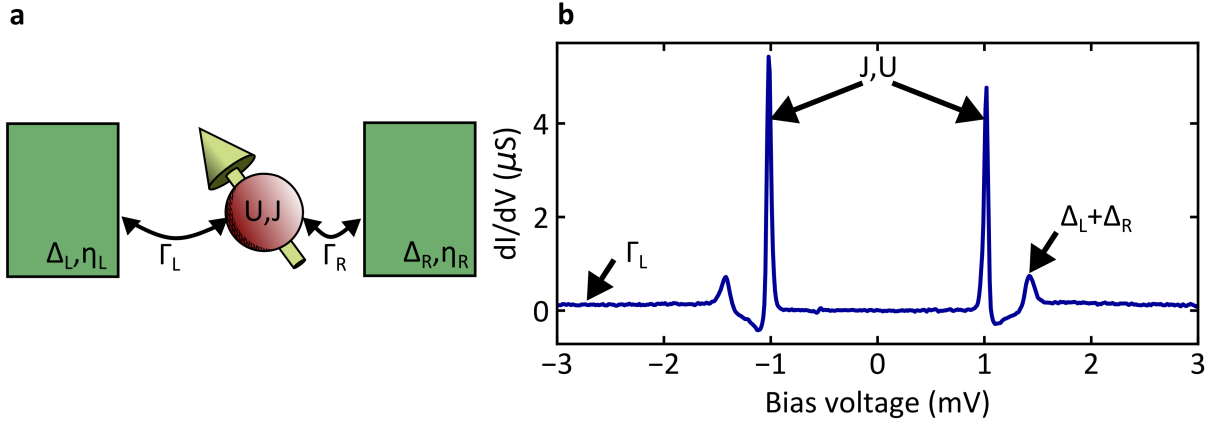


Figure 6.1: Extraction of the parameters for the model. (a) shows a sketch of the key parameters. (b) shows from which feature in an experimental spectrum these may be obtained.

To model an experimental spectrum without microwaves, we first fix the parameters directly accessible in experiment:

1. The temperature T is accessible from the thermometer reading, which was 0.56 K for all the experiments in the scope of this work.
2. The sum of the gaps $\Delta_L + \Delta_R$ can be extracted from the location of the coherence peaks in the spectrum. By considering possible thermal peaks, the individual values can also be identified. For example if a thermally excited YSR peak is seen, then we know that Δ_R is just halfway between the normal and thermal peak.
3. Once the gap is known, the YSR energy can be calculated from $E_{\text{peak}} = \Delta_L + \epsilon$. From this, the parameter J can be extracted.
4. Finally, the parameter U can be found by looking at the asymmetry of the YSR peaks. For large U , adjustments in J need to be made to keep the YSR energy ϵ constant.
5. The coupling Γ_L can be extracted by matching the transmission τ to the experimental transmission, which we extract from the slope of the $I - V$ curve in the normal conducting region. We keep $\Gamma_S = 100$ meV constant, as this is just a scaling factor for the other parameters [81].

Once the microwaves are switched on, no extra parameters are needed in theory. This is because the microwave frequency is an input in the experiment and the dimensionless amplitude can be calculated from the transfer function. In practice it is sometimes necessary to consider α as a fit parameter due to changes in the transfer function.

We add the Gaussian broadening by hand after performing the calculations. Strictly speaking, the multiple Andreev reflections should be treated in the context of $P(E)$ -theory. As this

is not part of the present theory, for the scope of this work, we subsume all external noise effects under a Gaussian broadening. It should be noted that the Gaussian broadening and the Dynes broadening are not the same (see Section 5.5.2). While the Gaussian broadening does not change the underlying physics and is a measure of the experimental broadening, the Dynes parameter contains information about the lifetime of quasiparticles. Figure 6.2(a) shows a spectrum calculated for different values of η and panel (b) shows the evolution of the peaks. It should be noted that this plot should be treated with care. It seems counter-intuitive that the ground state tunneling (GST) peak height should drop with decreasing η . This is because the Gaussian broadening is kept constant, leading to a smearing out of the sharp peaks. The main conclusion from this analysis is that the relative height of GST and excited state tunneling (EST) peaks can be tuned by changing η , i.e. the lifetime.

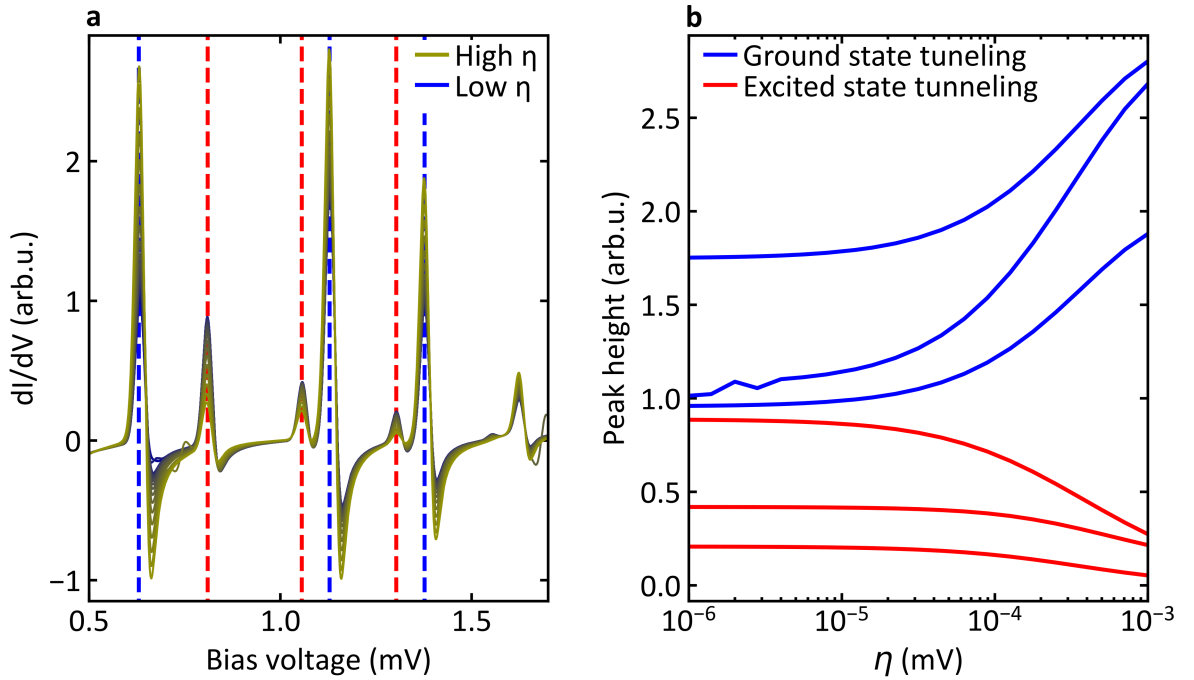


Figure 6.2: Dependence of peaks on the lifetime of the YSR state. The parameters are (in meV): $\Delta_L = 0.724$, $\Delta_R = 0.59$, $J = 75.5$, $U = 0$, $\Gamma_R = 100$, $\eta_L = 10^{-4}$, $\sigma_{\text{Gauss}} = 12.5 \times 10^{-3}$. The frequency is 60.05 GHz, $\alpha = 2.4$ and $\tau = 1.7 \times 10^{-3}$. (a) shows different spectra at different lifetime of the YSR state η_R . (b) shows the corresponding peak heights for normal and excited state tunneling.

6.2 Validity of the Models

In the Dyson equation, one has to define a cut-off in the recursive scheme at some point. This cut-off essentially determines the maximum order of the processes that are being considered.

For example, consider the Taylor expansion:

$$I(\tau) = I_1\tau + \frac{1}{2}I_2\tau^2 + \frac{1}{6}I_3\tau^3 + O(\tau^4) \quad (6.1)$$

Now for example the first and second order term become comparable when $\tau_c = O(2I_1/I_2)$. However, if I_2 contains some term which can be resonant, then this resonance will lead to a reduction in the cut-off transparency τ_c . This means that as soon as resonances are involved, the approximations tend to fail at lower transparencies.

We observe this behaviour in the modelling of YSR states under microwave irradiation. Here we compare three models:

1. Full Green's functions code (black)
2. Green's function code to first order (blue)
3. Regularized Andreev approximation (red)

For the first order approximation we stop the code at $n = \pm 1$. Specifically, this means that the transfer coefficients in equation 5.3 are only calculated to first order in the recursive relation [154]. Finally, the regularized code is the expression in equation 5.6 with corrections in the denominator. The full equations, which have been derived by Juan Carlos Cuevas, read:

$$I_{\text{qp}}^{(\text{reg})} \approx \frac{4e\pi^2|t|^2}{h} \sum_k J_k^2(\alpha) \int_{-\infty}^{\infty} dE \left\{ \frac{\rho_t(E + eV + k\hbar\omega) \rho_{\text{imp},1}(E)}{|1 - |t|^2 J_k^2(\alpha) (g_{L,-1}^k)^a (g_{R,0}^a)_{11}|^2} \times \right. \\ \times [f(E - eV + l\hbar\omega) - f(E)] - \\ \left. - \frac{\rho_t(E + eV + k\hbar\omega) \rho_{\text{imp},2}(E)}{|1 - |t|^2 J_k^2(\alpha) (g_{L,1}^k)^a (g_{R,0}^a)_{22}|^2} [f(E + eV + l\hbar\omega) - f(E)] \right\} \quad (6.2)$$

$$I_{\text{AR}}^{(\text{reg})} \approx \frac{8e\pi^2|t|^4}{h} \sum_{k,l} J_k^2(\alpha) J_l^2(\alpha) \int_{-\infty}^{\infty} dE \times \\ \times \frac{\rho_t(E - eV + k\hbar\omega) \rho_t(E + eV + l\hbar\omega) |(g_R)_{12}(E)|^2}{\left| \left[1 - |t|^2 J_k^2(\alpha) (g_{L,-1}^k)^a (g_{R,0}^a)_{11} \right] \left[1 - |t|^2 J_l^2(\alpha) (g_{L,1}^l)^a (g_{R,0}^a)_{22} \right] \right|^2} \times \\ \times [f(E - eV + k\hbar\omega) - f(E + eV + l\hbar\omega)]. \quad (6.3)$$

Here $\rho_{\text{imp},i}(E) = (1/\pi) \text{Im} \left\{ (g_{R,0}^a)_{ii} \right\}$ ($i = 1, 2$) and $[\rho_{\text{imp}}(E) = \rho_{\text{imp},1}(E) + \rho_{\text{imp},2}(-E)]$. The term $I_{\text{AR}}^{(\text{reg})}$ was obtained by picking out just the resonant term from all the two-particle processes.

To assess the agreement of model A referenced to model B with functions $f_A(x)$ and $f_B(x)$, we evaluate the mean squared deviation referenced to the mean squared deviation from zero:

$$\chi^2 = \int (f_B(x) - f_A(x))^2 dx / \left(\int (f_B(x))^2 dx \right) \quad (6.4)$$

We start by plotting the evolution of the spectrum without microwaves as a function of conductance in Figure 6.3(a). We normalized every spectrum by the conductance. For each spectrum, we calculated the deviation referenced to the full Green's function code and plot this in panel (b). The regularized Andreev model deviates by more than 5% from the full calculation at a transparency of $\tau_{c,AR} = 4 \times 10^{-2}$, whereas the deviations of the first order code become relevant at $\tau_{c,1st} = 10^{-1}$.

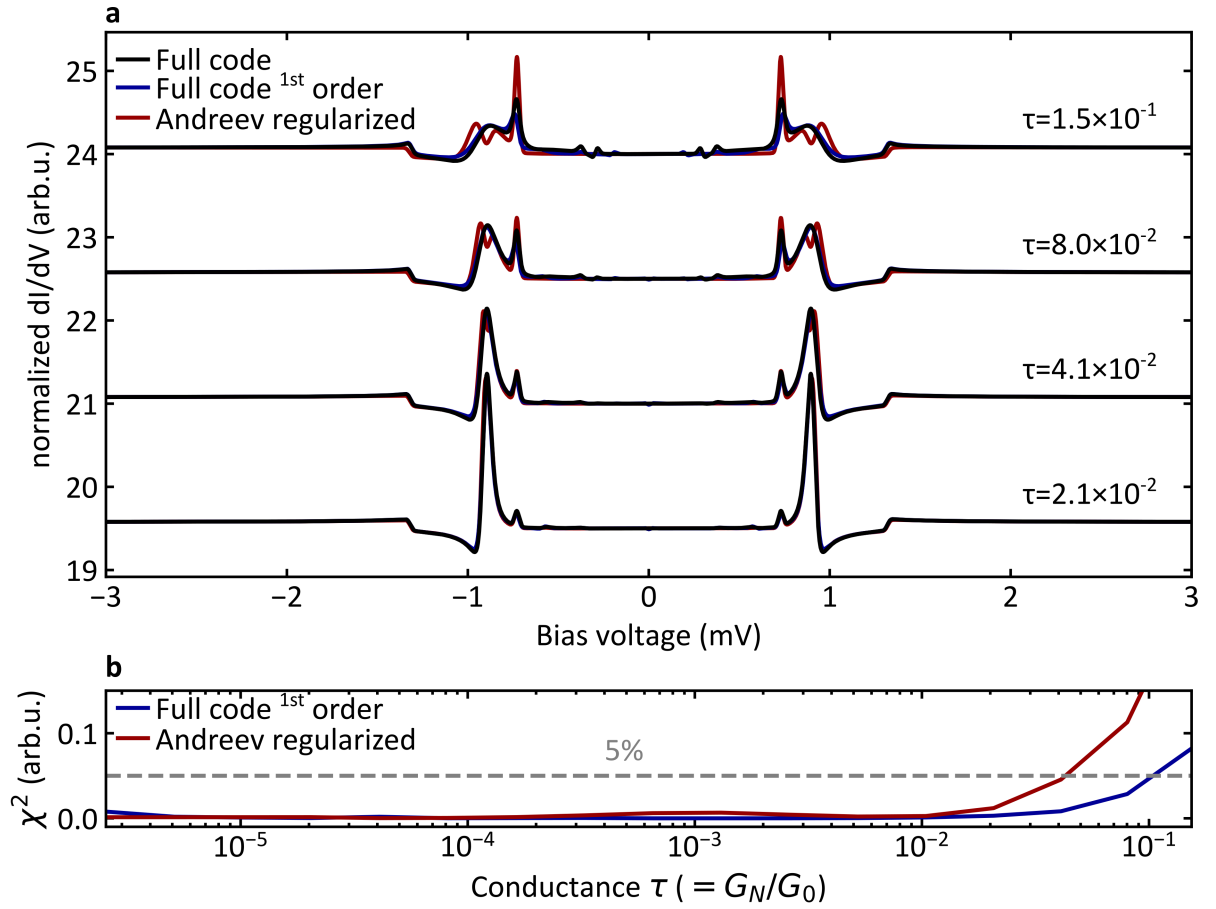


Figure 6.3: Evolution of calculated spectra with conductance. (a) shows example spectra at four conductances. (b) illustrates the deviation of the two models from the full model. The parameters are (in meV): $\Delta_L = 0.73$, $\Delta_R = 0.59$, $J = 75.3$, $U = 0$, $\Gamma_R = 100$, $\eta_R = 6 \times 10^{-4}$, $\eta_L = 10^{-4}$, $\sigma_{\text{Gauss}} = 12.5 \times 10^{-3}$.

In contrast to that, once the microwaves are included, the three models become inconsistent much faster. Figure 6.4(a) shows four spectra calculated at different conductances. At the highest

conductance, the regularized Andreev model shows deviations in peak height, amplitude and even position. This means that the interference of higher order processes is crucial to describe the spectrum under microwave irradiation. Panel (b) shows the deviations which start about two orders of magnitude sooner.

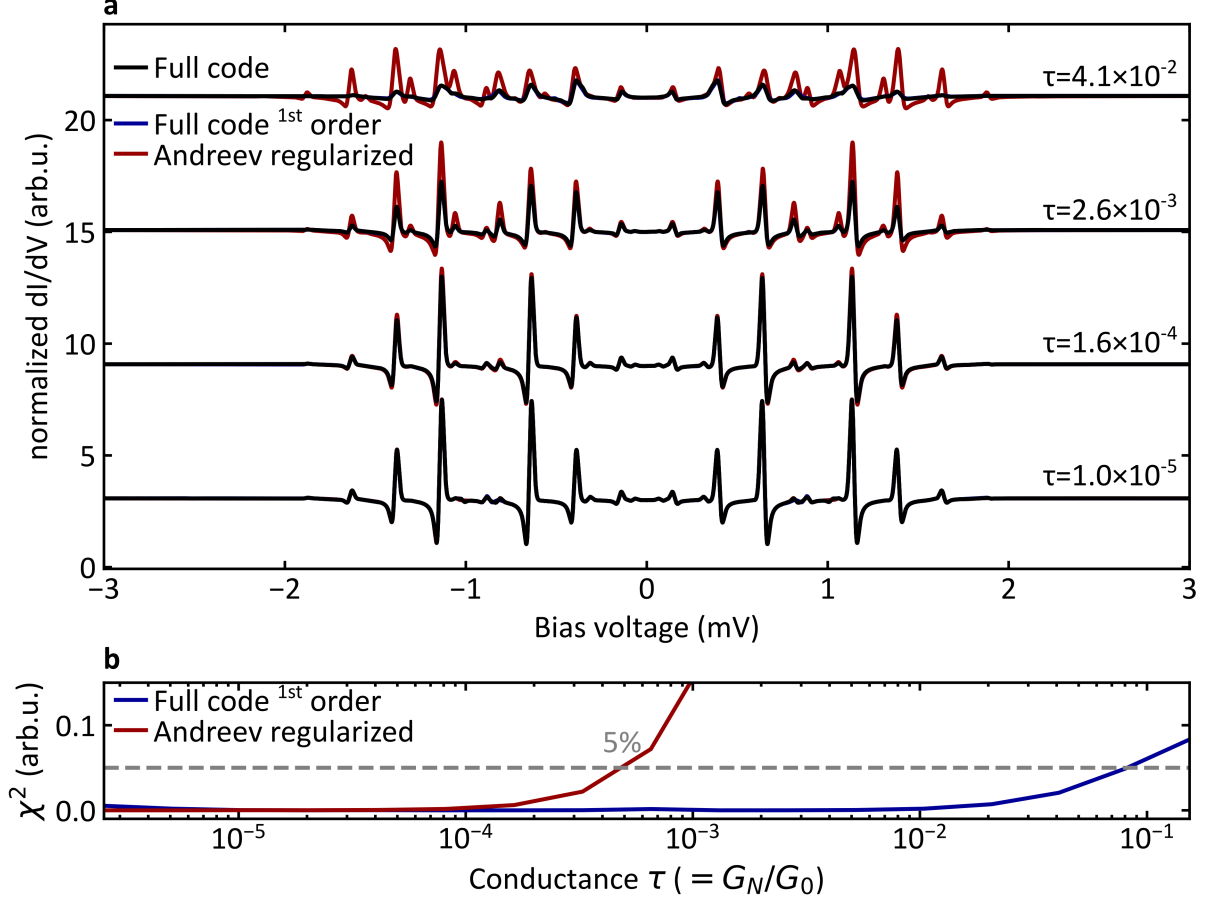


Figure 6.4: Evolution of calculated microwave spectra with conductance. (a) shows example spectra at four conductances. (b) illustrates the deviation of the two models from the full model. The parameters are (in meV): $\Delta_L = 0.73$, $\Delta_R = 0.59$, $J = 75.3$, $U = 0$, $\Gamma_R = 100$, $\eta_R = 6 \times 10^{-4}$, $\eta_L = 10^{-4}$, $\sigma_{\text{Gauss}} = 12.5 \times 10^{-3}$. The frequency is 60.05 GHz, $\alpha = 2.2$.

The comparison of the behaviour with and without microwaves leads to an important conclusion for the experimental data. Firstly, for measurements without microwaves, the three models remain consistent up to $\tau = 4 \times 10^{-2}$ which, for a bias voltage of 4 mV, corresponds to roughly 12 nA. This means that for typical setpoint currents of $O(100 \text{ pA})$, higher order contributions are not relevant. In contrast to that, the regularized Andreev model with microwaves shows significant disagreement already at $\tau_{\text{c,AR,MW}} = 5 \times 10^{-4}$, corresponding to roughly 150 pA. This means that for typical measurements with microwaves and YSR states, a higher order Green's function approach is necessary. The resonances due to interaction with the quanta $\hbar\omega$

lead to a failure of the lowest order approximation.

6.3 Peak Evolution with Conductance

In Chapter 5, we have already introduced the simplified model. While it provides a good understanding for the underlying physics, it is a strong approximation and cannot be used for fitting. However, it is possible to determine the transparencies at which the model breaks down. This is the subject of this chapter. Consider an expression for the current where we assume that we can apply a Taylor expansion in the conductance:

$$I(\tau) = I_1\tau + \frac{1}{2}I_2\tau^2 + \frac{1}{6}I_3\tau^3 + O(\tau^4) \quad (6.5)$$

It is tempting to claim that I_1 would be due to quasiparticle tunneling, I_2 due to a first order Andreev reflection, etc. If that were true, one would expect a transition from the linear to a quadratic regime etc. However, it is important to keep in mind that there is also a second order QP term for example [128]. This means that different contributions cannot be disentangled based on their dependence on the conductance. It is precisely for this reason that we see the complex evolution of the peak height in experiment. We measure microwave spectra at various transparencies while keeping the RF amplitude constant to $\alpha = 2.4$. We do this by changing the setpoint current from 40 pA to 4 nA. The parameter $\alpha = 2.4$ is chosen to facilitate the analysis of the peak height. Usually the EST peaks are smaller than the GST peaks. We chose this microwave amplitude to ensure that there are two EST peaks which are maximal. Figure 6.5(a) shows the spectra normalized by the conductance. Some of the peaks will be due to ground state tunneling (GST) and some of the peaks due to excited state tunneling (EST). The red (blue) line between the two panels shows the GST (EST) which we will analyze in detail in the following section. Figure 6.5(b) shows the corresponding modeling using the full Green's function code. The parameters were chosen such that the low-conductance spectra match. We see that in experiment, all the peaks reduce with conductance. The only difference between GST and EST is that the normalized EST peaks do not drop as fast with increasing conductance. In the simulation, the normalized EST peaks actually increase with conductance, reflecting the fact that a second order process (scaling as τ^2) gives the main contribution to EST. The normalized GST peaks drop with conductance due to Andreev reflections.

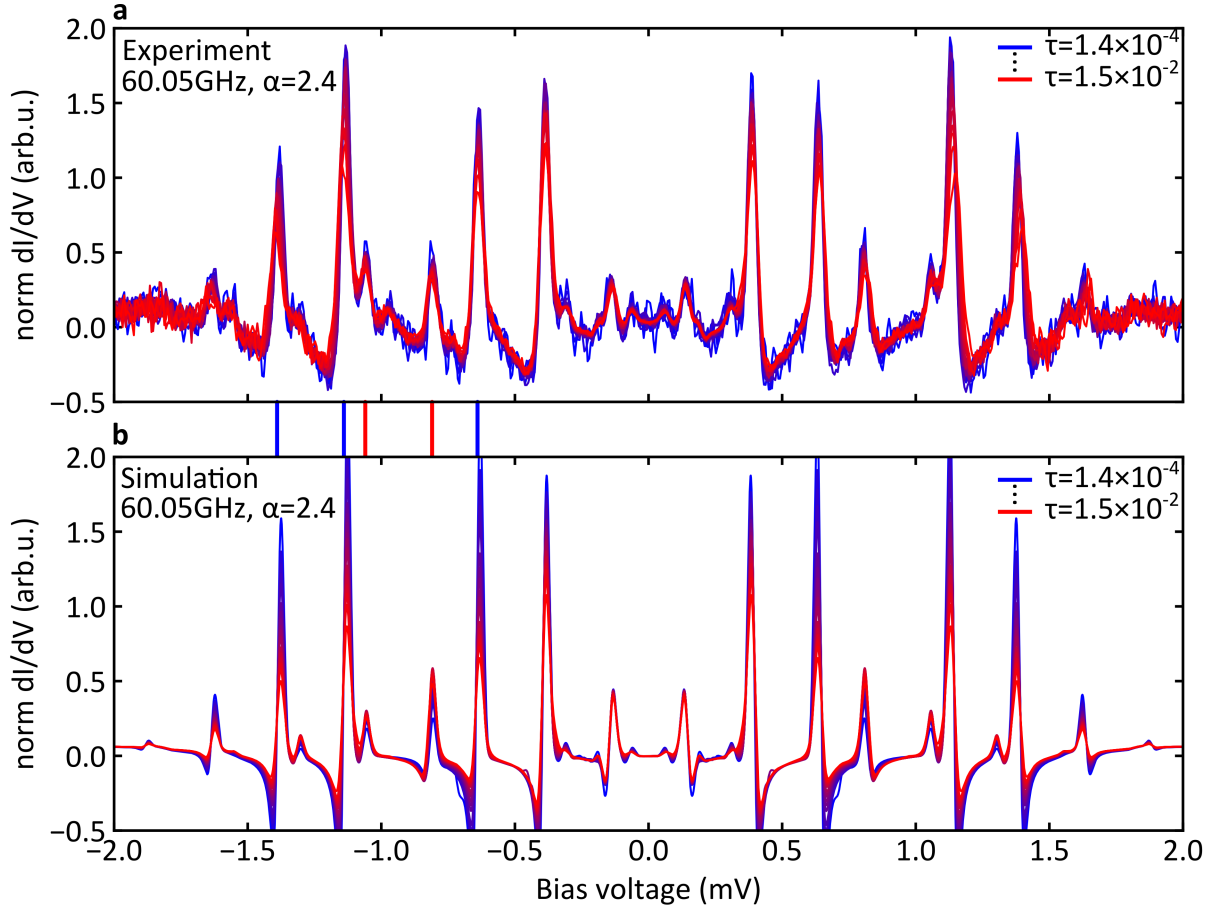


Figure 6.5: Evolution of experimental spectra with conductance. (a) shows the experimental spectra measured at a bias voltage of 3 mV and current setpoints ranging from 40 pA to 4 nA. (b) shows the corresponding modelling. The parameters are (in meV) $\Delta_L = 0.724$, $\Delta_R = 0.59$, $J = 75.5$, $U = 0$, $\Gamma_R = 100$, $\eta_{L,R} = 10^{-4}$, $\sigma_{\text{Gauss}} = 12.5 \times 10^{-3}$. The frequency is 60.05 GHz, $\alpha = 2.4$.

Figure 6.6 illustrates the peak evolution of the spectra labelled by red and blue lines connecting the panels in Figure 6.5. We show grey dashed lines to give a comparison to a fully linear process (i.e. $dI/dV_{\text{peak}} \propto \tau$). Panel (a) shows the experimental data. Both families of peaks show first a linear evolution going then to sub-linear behaviour at high conductance. The simulation in panel (b) shows that the peaks corresponding to ground state tunneling are already sublinear. In contrast to that, the the EST peaks first grow in a superlinear fashion and then eventually become sublinear too.

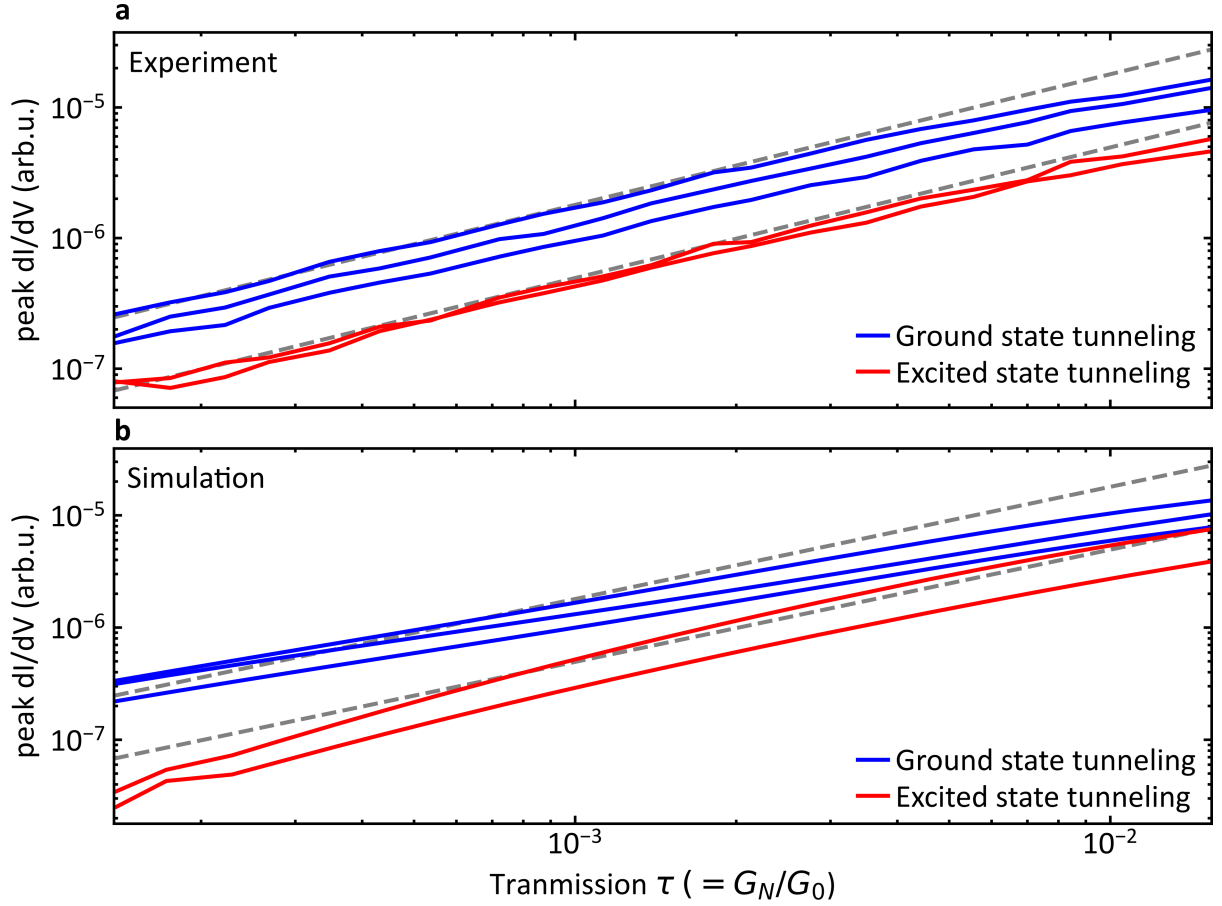


Figure 6.6: Evolution of peak height with conductance. (a) shows the peak height found in experiment at the positions marked in Figure 6.5. (b) illustrates theoretical peak evolution of these same peaks. The parameters are (in meV) $\Delta_L = 0.724$, $\Delta_R = 0.59$, $J = 75.5$, $U = 0$, $\Gamma_R = 100$, $\eta_{L,R} = 10^{-4}$, $\sigma_{\text{Gauss}} = 12.5 \times 10^{-3}$. The frequency is 60.05 GHz, $\alpha = 2.4$.

The simplified model in section 5.5.2 describes excited state tunneling as a two-electron process. This raises the natural question why in Figure 6.6, we do not see a quadratic dependence, neither in experiment nor in the simulation. There are several reasons for this:

1. Even the second order model has to include a regularization in the denominator due to higher order processes, thereby clouding the pure $\propto \tau^2$ dependence.
2. The resonance of this process means that higher order contributions become relevant much earlier as seen in Figure 6.4. The lowest measured transparency in experiment is $\tau = 1.4 \times 10^{-4}$, which is already in the regime where the simple model breaks down and higher order processes need to be considered.
3. It should be noted that the peaks are not infinitely sharp. The overlap makes an analysis of the conductance dependence even harder. For example, consider the peak at ± 1.06 mV in

Figure 6.5, which is EST. However, there is a significant contribution from the GST peak nearby.

6.4 Outlook

We have examined the validity of the models under microwaves and seen that the resonances necessitate the inclusion of higher order processes for experimentally realistic parameters. This leads to a complex evolution of the peak height. Future work could extend the range of experimental transparencies by working on YSR states with smaller BCS channel and longer integration times. Currents down to 10 pA (corresponding to $\tau = 4 \times 10^{-5}$ at 3 mV bias voltage) would be realistic. This would then allow to study the superlinear dependence of the excited state tunneling predicted in the model in more depth. While there has been work exploring conductances down to $10^{-9}G_0$ [43], it should be noted that microwaves lead to a reduction in spectral weight of the main peaks, meaning that it is not possible to go that low in transmission for microwave-assisted tunneling.

7

Conclusion and Outlook

This thesis is devoted to the study of energy scales in scanning tunneling microscopy. One key requirement for such experiments is a sufficiently high energy resolution. Therefore, the first part of this work had the objective to develop a system where the influence of the various sources of noise would be minimised. In particular, we presented the construction of a setup operating at 0.56 K by means of a ^3He cryostat. This temperature corresponds to a thermal energy of $k_B \sim 50 \mu\text{eV}$. This is well below the microwave energy $\hbar\omega$ which we apply to the junction with an external microwave antenna in the band of 60 – 90 GHz. By means of various improvements, most notably the inclusion of cold powder filters at the scan head, we achieved a width in the Josephson effect of $12 \mu\text{V}$. Now the width of the Josephson effect is strongly dependent on the electronic noise of a system, so that we conclude that cold powder filters led to a significant reduction of the electronic noise. This is in spite of the fact that the system is located in a building not optimized for such low noise measurements. The observed energy resolution is relevant for two reasons. Firstly it proves that powder filters installed at the scan head are a powerful tool for reducing the electronic noise in STM. Additionally this result serves as a guidance for optimizing the performance in machines to be built in the future by providing proof-of-principle for techniques novel to STM such as the use of superconducting coaxial cables, customized $I - V$ converters or the use of screw-in filters as interface into the scan head. With this state-of-the-art energy resolution, the width of features in a spectrum is greatly reduced, allowing to distinguish peaks which are very close to each other. More precisely, the observed width of YSR states in contact with a superconductor was seen to be just $40 \mu\text{V}$. With this improvement applied to systems at mK temperatures, one can only speculate about the energy resolution possible there. This would open new paths of research as for example the study of nuclear spins. With an improved energy resolution, one could perform DC measurements in a magnetic field and detect the splitting of energy levels simply by sweeping the bias voltage. Finally, the narrow Josephson effect is a useful foundation for exploring phenomena in the field of Josephson physics. In particular the periodic microwave drive might lead to so-called Andreev-Floquet states which have been predicted theoretically [156] and first attempts in planar junctions have been made

[129].

The second part of the thesis exploited the improved energy resolution to study how YSR states behave under microwave irradiation. The target system was a V(100) surface which was probed with a YSR-functionalized vanadium tip. These YSR states typically lead to two main peaks in a differential conductance spectrum. Once microwaves are applied, Tien-Gordon theory predicts the formation of replicas offset by multiples of $\hbar\omega/e$ along the voltage axis [116]. We observed a series of anomalous peaks appearing at bias voltages $eV = \Delta - \epsilon \pm n\hbar\omega$, where Δ is the superconducting gap, ϵ the energy of the YSR state and $\hbar\omega$ the microwave energy. We labelled this family of peaks *excited state tunneling* as opposed to *ground state tunneling* which gives rise to peaks at $eV = \Delta + \epsilon \pm n\hbar\omega$. The anomalous peaks originate from a second order Andreev process, where the first electron absorbs a sufficient number of quanta to excite the YSR state and the excited YSR state then resonantly relaxes. This process is only possible due to the combination of the tunnel contact with microwave irradiation and the peaks can clearly be told apart owing to the improved energy resolution. This makes the present setup an ideal candidate for studying the excitation of YSR states. We derive a simplified model which relies on a threshold function to describe quantitatively the threshold for exciting YSR states and thereby enabling the tunnel process leading to the anomalous peaks. The fact that it is possible to set the bias voltage and microwave parameters such that an excitation process is in resonance means that we can excite the YSR state in a CW mode. Furthermore, sweeping the frequency allowed us to track down these two processes. This method makes it possible to study resonances on the frequency axis, thereby giving improved resolution. A natural next step would be an extension to pump-probe measurements which ideally would enable us to controllably excite the state and then deduce the lifetime of the YSR states. Another route of research could be the study of shot noise under microwave irradiation, with a MHz amplifier which has already been used in other work [48, 108].

The final section of the thesis was about the analysis of the experimental data using a full Green's function approach. Firstly, we found that a full approach gives excellent quantitative agreement with the data, indicating that it is a powerful and reliable tool to describe the microwave excitation of YSR states. By comparing several approximations in the model, we found that the resonant nature of the excited state tunneling process makes the full model deviate from the lowest order approximation at much lower transparencies ($\tau = 10^{-4}$) than in the model without microwaves ($\tau = 10^{-2}$), implying that proposed approximations [23] should be viewed critically. Apart from that, this early onset of resonances explains why the conductance dependence of experimental spectra cannot be divided into regimes of powers of transparency τ^n . This has important implications for future experiments, for example shot noise measurements. In such experiments, the Fano factor, i.e. the ratio of noise to the current, is determined as a function of the applied bias voltage. Depending on which processes are possible, this Fano factor deviates from the classical result $F = 1$. Our analysis implies that such Fano factors would then have to be

analysed using a full approach [62]. Finally, from the intensity of EST peaks with respect to GST peaks, we deduce a rough estimate of the lower limit of the lifetimes of the YSR states, which is $\hbar/\Gamma > 40$ ns. This is in line with previously reported work (48 ns at 10 mK [43]). Overall this fitting provides another indirect method of estimating the lifetime of YSR states – with the advantage that this can be done at much lower conductances than in other methods.

Bibliography

1. Abbott, B. *et al.* Properties of the Binary Black Hole Merger GW150914. *Physical Review Letters* **116**, 241102 (2016).
2. Ewen, H. I. & Purcell, E. M. Observation of a Line in the Galactic Radio Spectrum: Radiation from Galactic Hydrogen at 1,420 Mc./sec. *Nature* **168**, 356–356 (1951).
3. Fricke, L. *et al.* Coherent control of a donor-molecule electron spin qubit in silicon. *Nature Communications* **12** (2021).
4. Veldhorst, M. *et al.* An addressable quantum dot qubit with fault-tolerant control-fidelity. *Nature Nanotechnology* **9**, 981–985 (2014).
5. Binnig, G. & Rohrer, H. Scanning tunneling microscopy. *Surface Science* **126**, 236–244 (1983).
6. Crommie, M. F., Lutz, C. P. & Eigler, D. M. Confinement of Electrons to Quantum Corrals on a Metal Surface. *Science* **262**, 218–220 (1993).
7. Schwenk, J. *et al.* Achieving μeV tunneling resolution in an in-operando scanning tunneling microscopy, atomic force microscopy, and magnetotransport system for quantum materials research. *Review of Scientific Instruments* **91**, 071101 (2020).
8. Zu, H., Dai, W. & de Waele, A. Development of dilution refrigerators—A review. *Cryogenics* **121**, 103390 (2022).
9. Phillips, W. D. Nobel Lecture: Laser cooling and trapping of neutral atoms. *Reviews of Modern Physics* **70**, 721–741 (1998).
10. Assig, M. *et al.* A 10 mK scanning tunneling microscope operating in ultra high vacuum and high magnetic fields. *Review of Scientific Instruments* **84**, 033903 (2013).
11. Misra, S. *et al.* Design and performance of an ultra-high vacuum scanning tunneling microscope operating at dilution refrigerator temperatures and high magnetic fields. *Review of Scientific Instruments* **84**, 103903 (2013).
12. Song, Y. J. *et al.* Invited Review Article: A 10 mK scanning probe microscopy facility. *Review of Scientific Instruments* **81**, 121101 (2010).
13. Ast, C. R. *et al.* Sensing the quantum limit in scanning tunnelling spectroscopy. *Nature Communications* **7** (2016).

14. Fernández-Lomana, M. *et al.* Millikelvin scanning tunneling microscope at 20/22 T with a graphite enabled stick–slip approach and an energy resolution below 8 μeV : Application to conductance quantization at 20 T in single atom point contacts of Al and Au and to the charge density wave of 2H–NbSe₂. *Review of Scientific Instruments* **92**, 093701 (2021).
15. Lukashenko, A. & Ustinov, A. V. Improved powder filters for qubit measurements. *Review of Scientific Instruments* **79**, 014701 (2008).
16. Jaklevic, R. C., Lambe, J., Silver, A. H. & Mercereau, J. E. Quantum Interference Effects in Josephson Tunneling. *Physical Review Letters* **12**, 159–160 (1964).
17. Behr, R., Kieler, O., Kohlmann, J., Müller, F. & Palafox, L. Development and metrological applications of Josephson arrays at PTB. *Measurement Science and Technology* **23**, 124002 (2012).
18. Martinis, J. M. Superconducting phase qubits. *Quantum Information Processing* **8**, 81–103 (2009).
19. Makhlin, Y., Schön, G. & Shnirman, A. Quantum-state engineering with Josephson-junction devices. *Reviews of Modern Physics* **73**, 357–400 (2001).
20. DiVincenzo, D. P. The Physical Implementation of Quantum Computation. *Fortschritte der Physik* **48**, 771–783 (2000).
21. Kukulín, V. I., Krasnopol'sky, V. & Horáček, J. *Theory of resonances: Principles and Applications* (Springer Science & Business Media, 2013).
22. Miroshnichenko, A. E., Flach, S. & Kivshar, Y. S. Fano resonances in nanoscale structures. *Reviews of Modern Physics* **82**, 2257–2298 (2010).
23. Gonzalez, S. A. *et al.* Photon-assisted resonant Andreev reflections: Yu-Shiba-Rusinov and Majorana states. *Phys. Rev. B* **102**, 045413 (4 2020).
24. Beiser, A. *Concepts of modern physics (6th edition)* (McGraw-Hill, 2003).
25. Hölzl, J. & Schulte, F. K. in *Springer Tracts in Modern Physics* 1–150 (Springer Berlin Heidelberg, 1979).
26. Bardeen, J. Tunnelling from a Many-Particle Point of View. *Physical Review Letters* **6**, 57–59 (1961).
27. Chen, J. C. *Introduction to Scanning Tunneling Microscopy, 2nd Edition* (Oxford University Press, 2007).
28. Tersoff, J. & Hamann, D. R. Theory of the scanning tunneling microscope. *Physical Review B* **31**, 805–813 (1985).
29. Klein, J., Léger, A., Belin, M., Défourneau, D. & Sangster, M. J. L. Inelastic-Electron-Tunneling Spectroscopy of Metal-Insulator-Metal Junctions. *Physical Review B* **7**, 2336–2348 (1973).

30. Hwang, J. *et al.* Development of a scanning tunneling microscope for variable temperature electron spin resonance. *Review of Scientific Instruments* **93**, 093703 (2022).
31. Musket, R., McLean, W., Colmenares, C., Makowiecki, D. & Siekhaus, W. Preparation of atomically clean surfaces of selected elements: A review. *Applications of Surface Science* **10**, 143–207 (1982).
32. Kezilebieke, S. *et al.* Topological superconductivity in a van der Waals heterostructure. *Nature* **588**, 424–428 (2020).
33. Zhao, A. *et al.* Kondo effect in single cobalt phthalocyanine molecules adsorbed on Au(111) monoatomic steps. *The Journal of Chemical Physics* **128**, 234705 (2008).
34. Kondo, J. Resistance Minimum in Dilute Magnetic Alloys. *Progress of Theoretical Physics* **32**, 37–49 (1964).
35. Wu, X. *et al.* Imaging single glycans. *Nature* **582**, 375–378 (2020).
36. Hebenstreit, W. *et al.* Atomic resolution by STM on ultra-thin films of alkali halides: experiment and local density calculations. *Surface Science* **424**, L321–L328 (1999).
37. Schintke, S. *et al.* Insulator at the Ultrathin Limit: MgO on Ag(001). *Physical Review Letters* **87**, 276801 (2001).
38. Heinze, S. *et al.* Spontaneous atomic-scale magnetic skyrmion lattice in two dimensions. *Nature Physics* **7**, 713–718 (2011).
39. Forrester, P. R., Bilgeri, T., Patthey, F., Brune, H. & Natterer, F. D. Antiferromagnetic MnNi tips for spin-polarized scanning probe microscopy. *Review of Scientific Instruments* **89**, 123706 (2018).
40. Ternes, M. *et al.* Subgap structure in asymmetric superconducting tunnel junctions. *Physical Review B* **74**, 132501 (2006).
41. Meservey, R. & Tedrow, P. Spin-polarized electron tunneling. *Physics Reports* **238**, 173–243 (1994).
42. Eltschka, M. *et al.* Probing Absolute Spin Polarization at the Nanoscale. *Nano Letters* **14**, 7171–7174 (2014).
43. Huang, H. *et al.* Tunnelling dynamics between superconducting bound states at the atomic limit. *Nature Physics* **16**, 1227–1231 (2020).
44. Baumann, S. *et al.* Electron paramagnetic resonance of individual atoms on a surface. *Science* **350**, 417–420 (2015).
45. Alexa, P. *et al.* Enhancing Hydrogen Evolution Activity of Au(111) in Alkaline Media through Molecular Engineering of a 2D Polymer. *Angewandte Chemie International Edition* **59**, 8411–8415 (2020).

-
46. Kezilebieke, S., Dvorak, M., Ojanen, T. & Liljeroth, P. Coupled Yu–Shiba–Rusinov States in Molecular Dimers on NbSe₂. *Nano Letters* **18**, PMID: 29533636, 2311–2315 (2018).
 47. Blanter, Y. & Büttiker, M. Shot noise in mesoscopic conductors. *Physics Reports* **336**, 1–166 (2000).
 48. Bastiaans, K. M. *et al.* Direct evidence for Cooper pairing without a spectral gap in a disordered superconductor above T_C . *Science* **374**, 608–611 (2021).
 49. Hänze, M. *et al.* Quantum stochastic resonance of individual Fe atoms. *Science Advances* **7** (2021).
 50. Alvarado, S., Libioulle, L. & Seidler, P. STM-excited luminescence on organic materials. *Synthetic Metals* **91**, 69–72 (1997).
 51. Merino, P., Große, C., Rosławska, A., Kuhnke, K. & Kern, K. Exciton dynamics of C60-based single-photon emitters explored by Hanbury Brown–Twiss scanning tunnelling microscopy. *Nature Communications* **6** (2015).
 52. Loth, S., Etzkorn, M., Lutz, C. P., Eigler, D. M. & Heinrich, A. J. Measurement of Fast Electron Spin Relaxation Times with Atomic Resolution. *Science* **329**, 1628–1630 (2010).
 53. Yang, K. *et al.* Coherent spin manipulation of individual atoms on a surface. *Science* **366**, 509–512 (2019).
 54. Zhang, Y.-h. *et al.* Temperature and magnetic field dependence of a Kondo system in the weak coupling regime. *Nature Communications* **4** (2013).
 55. Abdo, M. *et al.* Variable Repetition Rate THz Source for Ultrafast Scanning Tunneling Microscopy. *ACS Photonics* **8**, 702–708 (2021).
 56. Yoshida, S. *et al.* Terahertz Scanning Tunneling Microscopy for Visualizing Ultrafast Electron Motion in Nanoscale Potential Variations. *ACS Photonics* **8**, 315–323 (2021).
 57. Garg, M. & Kern, K. Attosecond coherent manipulation of electrons in tunneling microscopy. *Science* **367**, 411–415 (2020).
 58. Garg, M. *et al.* Real-space subfemtosecond imaging of quantum electronic coherences in molecules. *Nature Photonics* **16**, 196–202 (2021).
 59. Rammer, J. & Smith, H. Quantum field-theoretical methods in transport theory of metals. *Reviews of Modern Physics* **58**, 323–359 (1986).
 60. Cuevas, J. C. & Scheer, E. *Molecular Electronics* (WORLD SCIENTIFIC, 2010).
 61. Engquist, H. L. & Anderson, P. W. Definition and measurement of the electrical and thermal resistances. *Physical Review B* **24**, 1151–1154 (1981).

62. Cuevas, J. C., Martin-Rodero, A. & Yeyati, A. L. Shot Noise and Coherent Multiple Charge Transfer in Superconducting Quantum Point Contacts. *Physical Review Letters* **82**, 4086–4089 (1999).
63. Cyrot, M. Ginzburg-Landau theory for superconductors. *Reports on Progress in Physics* **36**, 103–158 (1973).
64. Abrikosov, A. The magnetic properties of superconducting alloys. *Journal of Physics and Chemistry of Solids* **2**, 199–208 (1957).
65. Bardeen, J., Cooper, L. N. & Schrieffer, J. R. Theory of Superconductivity. *Physical Review* **108**, 1175–1204 (1957).
66. Dynes, R. C., Narayanamurti, V. & Garno, J. P. Direct Measurement of Quasiparticle-Lifetime Broadening in a Strong-Coupled Superconductor. *Physical Review Letters* **41**, 1509–1512 (1978).
67. Bednorz, J. G. & Müller, K. A. Possible high T_c superconductivity in the Ba-La-Cu-O system. *Zeitschrift für Physik B Condensed Matter* **64**, 189–193 (1986).
68. Kamihara, Y. *et al.* Iron-Based Layered Superconductor: LaOFeP. *Journal of the American Chemical Society* **128**, 10012–10013 (2006).
69. Steglich, F. *et al.* Superconductivity in the Presence of Strong Pauli Paramagnetism: CeCu₂Si₂. *Physical Review Letters* **43**, 1892–1896 (1979).
70. Maki, K. *Introduction to d-wave superconductivity in AIP Conference Proceedings* (American Institute of Physics, 1998).
71. Gu, Q. *et al.* Directly visualizing the sign change of d-wave superconducting gap in Bi₂Sr₂CaCu₂O₈ by phase-referenced quasiparticle interference. *Nature Communications* **10** (2019).
72. Mackenzie, A. & Maeno, Y. p-wave superconductivity. *Physica B: Condensed Matter* **280**, 148–153 (2000).
73. Yu, L. Bound State in Superconductors with Paramagnetic Impurities. *Acta Physica Sinica* **21**, 75 (1965).
74. Shiba, H. Classical Spins in Superconductors. *Progress of Theoretical Physics* **40**, 435–451 (1968).
75. Rusinov, A. I. Superconductivity near a paramagnetic impurity. *JETP Lett. (USSR) (Engl. Transl.)*, 9: 85-7 (Jan. 20, 1969). (1969).
76. Ruby, M. *et al.* Tunneling Processes into Localized Subgap States in Superconductors. *Physical Review Letters* **115**, 087001 (2015).
77. Anderson, P. W. Localized Magnetic States in Metals. *Physical Review* **124**, 41–53 (1961).

78. Yoshioka, T. & Ohashi, Y. Numerical Renormalization Group Studies on Single Impurity Anderson Model in Superconductivity: A Unified Treatment of Magnetic, Nonmagnetic Impurities, and Resonance Scattering. *Journal of the Physical Society of Japan* **69**, 1812–1823 (2000).
79. Martin-Rodero, A. & Yeyati, A. L. The Andreev states of a superconducting quantum dot: mean field versus exact numerical results. *Journal of Physics: Condensed Matter* **24**, 385303 (2012).
80. Villas, A. *et al.* Interplay between Yu-Shiba-Rusinov states and multiple Andreev reflections. *Physical Review B* **101**, 235445 (2020).
81. Huang, H. *et al.* Quantum phase transitions and the role of impurity-substrate hybridization in Yu-Shiba-Rusinov states. *Communications Physics* **3** (2020).
82. *Mesoscopic Electron Transport* (eds Sohn, L. L., Kouwenhoven, L. P. & Schön, G.) (Springer Netherlands, 1997).
83. Goldhaber-Gordon, D. *et al.* Kondo effect in a single-electron transistor. *Nature* **391**, 156–159 (1998).
84. *Mesoscopic Physics and Electronics* (eds Ando, T., Arakawa, Y., Furuya, K., Komiyama, S. & Nakashima, H.) (Springer Berlin Heidelberg, 1998).
85. Senkpiel, J. *et al.* Dynamical Coulomb Blockade as a Local Probe for Quantum Transport. *Physical Review Letters* **124**, 156803 (2020).
86. Jørgensen, H. I., Novotný, T., Grove-Rasmussen, K., Flensberg, K. & Lindelof, P. E. Critical Current $0-\pi$ Transition in Designed Josephson Quantum Dot Junctions. *Nano Letters* **7**, 2441–2445 (2007).
87. Karan, S. *et al.* Superconducting quantum interference at the atomic scale. *Nature Physics* **18**, 893–898 (2022).
88. Hofstetter, L., Csonka, S., Nygård, J. & Schönenberger, C. Cooper pair splitter realized in a two-quantum-dot Y-junction. *Nature* **461**, 960–963 (2009).
89. Hays, M. *et al.* Coherent manipulation of an Andreev spin qubit. *Science* **373**, 430–433 (2021).
90. Padurariu, C. & Nazarov, Y. V. Theoretical proposal for superconducting spin qubits. *Physical Review B* **81**, 144519 (2010).
91. Yazdani, A., Jones, B. A., Lutz, C. P., Crommie, M. F. & Eigler, D. M. Probing the Local Effects of Magnetic Impurities on Superconductivity. *Science* **275**, 1767–1770 (1997).
92. Küster, F. *et al.* Correlating Josephson supercurrents and Shiba states in quantum spins unconventionally coupled to superconductors. *Nature Communications* **12** (2021).

93. Beck, P. *et al.* Spin-orbit coupling induced splitting of Yu-Shiba-Rusinov states in antiferromagnetic dimers. *Nature Communications* **12** (2021).
94. Farinacci, L. *et al.* Tuning the Coupling of an Individual Magnetic Impurity to a Superconductor: Quantum Phase Transition and Transport. *Physical Review Letters* **121**, 196803 (2018).
95. Franke, K. J., Schulze, G. & Pascual, J. I. Competition of Superconducting Phenomena and Kondo Screening at the Nanoscale. *Science* **332**, 940–944 (2011).
96. Peters, O. *et al.* Resonant Andreev reflections probed by photon-assisted tunnelling at the atomic scale. *Nature Physics* **16**, 1222–1226 (2020).
97. Randeria, M. T., Feldman, B. E., Drozdov, I. K. & Yazdani, A. Scanning Josephson spectroscopy on the atomic scale. *Physical Review B* **93**, 161115 (2016).
98. Ji, S.-H. *et al.* High-Resolution Scanning Tunneling Spectroscopy of Magnetic Impurity Induced Bound States in the Superconducting Gap of Pb Thin Films. *Physical Review Letters* **100**, 226801 (2008).
99. Huang, H. *et al.* Spin-dependent tunneling between individual superconducting bound states. *Phys. Rev. Research* **3**, L032008 (3 2021).
100. Wang, D., Wiebe, J., Zhong, R., Gu, G. & Wiesendanger, R. Spin-Polarized Yu-Shiba-Rusinov States in an Iron-Based Superconductor. *Phys. Rev. Lett.* **126**, 076802 (7 2021).
101. Kezilebieke, S., Žitko, R., Dvorak, M., Ojanen, T. & Liljeroth, P. Observation of Coexistence of Yu-Shiba-Rusinov States and Spin-Flip Excitations. *Nano Letters* **19**, 4614–4619 (2019).
102. Senkpiel, J. *et al.* Robustness of Yu-Shiba-Rusinov resonances in the presence of a complex superconducting order parameter. *Physical Review B* **100**, 014502 (2019).
103. Choi, D.-J. *et al.* Influence of Magnetic Ordering between Cr Adatoms on the Yu-Shiba-Rusinov States of the β -Bi₂Pd Superconductor. *Phys. Rev. Lett.* **120**, 167001 (16 2018).
104. Ding, H. *et al.* Tuning interactions between spins in a superconductor. *Proceedings of the National Academy of Sciences* **118** (2021).
105. Cornils, L. *et al.* Spin-Resolved Spectroscopy of the Yu-Shiba-Rusinov States of Individual Atoms. *Physical Review Letters* **119**, 197002 (2017).
106. Kamlapure, A. *et al.* Correlation of Yu-Shiba-Rusinov States and Kondo Resonances in Artificial Spin Arrays on an s-Wave Superconductor. *Nano Letters* **21**, 6748–6755 (2021).
107. Schneider, L. *et al.* Magnetism and in-gap states of 3d transition metal atoms on superconducting Re. *npj Quantum Materials* **4** (2019).

108. Thupakula, U. *et al.* Coherent and Incoherent Tunneling into Yu-Shiba-Rusinov States Revealed by Atomic Scale Shot-Noise Spectroscopy. *Physical Review Letters* **128**, 247001 (2022).
109. Majorana, E. & Maiani, L. in *Ettore Majorana Scientific Papers* 201–233 (Springer Berlin Heidelberg).
110. Lindner, N. H., Berg, E., Refael, G. & Stern, A. Fractionalizing Majorana Fermions: Non-Abelian Statistics on the Edges of Abelian Quantum Hall States. *Physical Review X* **2**, 041002 (2012).
111. Kitaev, A. Y. Unpaired Majorana fermions in quantum wires. *Physics-Uspekhi* **44**, 131–136 (2001).
112. Law, K. T., Lee, P. A. & Ng, T. K. Majorana Fermion Induced Resonant Andreev Reflection. *Physical Review Letters* **103**, 237001 (2009).
113. Nadj-Perge, S. *et al.* Observation of Majorana fermions in ferromagnetic atomic chains on a superconductor. *Science* **346**, 602–607 (2014).
114. Das, A. *et al.* Zero-bias peaks and splitting in an Al–InAs nanowire topological superconductor as a signature of Majorana fermions. *Nature Physics* **8**, 887–895 (2012).
115. Ingold, G.-L. & Nazarov, Y. V. in *NATO ASI Series* 21–107 (Springer US, 1992).
116. Tien, P. K. & Gordon, J. P. Multiphoton Process Observed in the Interaction of Microwave Fields with the Tunneling between Superconductor Films. *Physical Review* **129**, 647–651 (1963).
117. Falci, G., Bujanja, V. & Schön, G. Quasiparticle and Cooper pair tunneling in small capacitance Josephson junctions. *Zeitschrift für Physik B Condensed Matter* **85**, 451–458 (1991).
118. Zimmermann, U. & Keck, K. Multiple Andreev-reflection in superconducting weak-links in the interaction with external microwave-fields. *Zeitschrift für Physik B Condensed Matter* **101**, 555–560 (1996).
119. Kot, P. *et al.* Microwave-assisted tunneling and interference effects in superconducting junctions under fast driving signals. *Physical Review B* **101**, 134507 (2020).
120. Josephson, B. D. Coupled Superconductors. *Reviews of Modern Physics* **36**, 216–220 (1964).
121. Josephson, B. Supercurrents through barriers. *Advances in Physics* **14**, 419–451 (1965).
122. Ambegaokar, V. & Baratoff, A. Tunneling Between Superconductors. *Physical Review Letters* **10**, 486–489 (1963).

123. Rodrigo, J., Crespo, V. & Vieira, S. Josephson current at atomic scale: Tunneling and nanocontacts using a STM. *Physica C: Superconductivity and its Applications* **437-438**, 270–273 (2006).
124. Kimura, H., Barber, R. P., Ono, S., Ando, Y. & Dynes, R. C. Josephson scanning tunneling microscopy: A local and direct probe of the superconducting order parameter. *Physical Review B* **80**, 144506 (2009).
125. Harada, Y., Takayanagi, H. & Odintsov, A. A. Cooper-pair tunneling in small junctions with tunable Josephson coupling. *Physical Review B* **54**, 6608–6613 (1996).
126. Ivanchenko, Y. & Zil’berman, L. The Josephson Effect in Small Tunnel Contacts. *Soviet Journal of Experimental and Theoretical Physics* **28**, 1272 (1969).
127. Tamir, I., Caspari, V., Rolf, D., Lotze, C. & Franke, K. J. Shot-noise measurements of single-atom junctions. *Review of Scientific Instruments* **93**, 023702 (2022) (2021).
128. Cuevas, J. C., Martín-Rodero, A. & Yeyati, A. L. Hamiltonian approach to the transport properties of superconducting quantum point contacts. *Phys. Rev. B* **54**, 7366–7379 (10 1996).
129. Park, S. *et al.* Steady Floquet–Andreev states in graphene Josephson junctions. *Nature* **603**, 421–426 (2022).
130. Golubov, A. A., Kupriyanov, M. Y. & Il’ichev, E. The current-phase relation in Josephson junctions. *Reviews of Modern Physics* **76**, 411–469 (2004).
131. Senkpiel, J. *et al.* Single channel Josephson effect in a high transmission atomic contact. *Communications Physics* **3** (2020).
132. Ast, C. R., Assig, M., Ast, A. & Kern, K. Design criteria for scanning tunneling microscopes to reduce the response to external mechanical disturbances. *Review of Scientific Instruments* **79**, 093704 (2008).
133. Drost, R. *et al.* Combining electron spin resonance spectroscopy with scanning tunneling microscopy at high magnetic fields. *Review of Scientific Instruments* **93**, 043705 (2022).
134. Merkt, J. *Entwurf und Untersuchung einer Antenne für 84 GHz zur Strahlungseinkopplung in ein STM* Bachelor’s Thesis (KIT Karlsruher Institut für Technologie, 2017).
135. Zeppettella, D. & Ali, M. A broadband directional circularly polarized spiral antenna on EBG structure. *Journal of Electromagnetic Waves and Applications* **34**, 1563–1585 (2020).
136. Sciver, S. W. V. *Helium Cryogenics* (Springer New York, 2012).
137. Pan, S. H., Hudson, E. W. & Davis, J. C. ³He refrigerator based very low temperature scanning tunneling microscope. *Review of Scientific Instruments* **70**, 1459–1463 (1999).
138. Keller, W. E. *Helium-3 and Helium-4* (Springer US, 1969).

139. Pollack, G. L. Kapitza Resistance. *Reviews of Modern Physics* **41**, 48–81 (1969).
140. Vasilić, B., Shitov, S. V., Lobb, C. J. & Barbara, P. Josephson-junction arrays as high-efficiency sources of coherent millimeter-wave radiation. *Applied Physics Letters* **78**, 1137–1139 (2001).
141. Kieler, O. F. *et al.* Towards a 1 V Josephson Arbitrary Waveform Synthesizer. *IEEE Transactions on Applied Superconductivity* **25**, 1–5 (2015).
142. Imai, S., Shinagawa, M., Morita, S., Takeuti, Y. T. Y. & Mikoshiba, N. M. N. Simulation of Shapiro Steps in a Josephson Junction Based on the Microscopic Theory of the Tunnel Junction. *Japanese Journal of Applied Physics* **31**, 3546 (1992).
143. Horowitz, P. & Hill, W. *The Art of Electronics* (Cambridge University Pr., 2015).
144. Ludwig, R. & Bogdanov, G. *RF Circuit Design: Theory and Applications: International Edition* (Pearson; 2nd edition, 2007).
145. Thalmann, M., Pernau, H.-F., Strunk, C., Scheer, E. & Pietsch, T. Comparison of cryogenic low-pass filters. *Review of Scientific Instruments* **88**, 114703 (2017).
146. Scheller, C. P. *et al.* Silver-epoxy microwave filters and thermalizers for millikelvin experiments. *Applied Physics Letters* **104**, 211106 (2014).
147. Jensen, V., Andersen, J., Nielsen, H. & Adams, D. The surface structure of V(100). *Surface Science* **116**, 66–84 (1982).
148. Koller, R. *et al.* The structure of the oxygen induced (1×5) reconstruction of V(100). *Surface Science* **480**, 11–24 (2001).
149. Diebold, U. The surface science of titanium dioxide. *Surface Science Reports* **48**, 53–229 (2003).
150. Paul, W., Baumann, S., Lutz, C. P. & Heinrich, A. J. Generation of constant-amplitude radio-frequency sweeps at a tunnel junction for spin resonance STM. *Review of Scientific Instruments* **87**, 074703 (2016).
151. Yeyati, A. L., Cuevas, J. C., López-Dávalos, A. & Martín-Rodero, A. Resonant tunneling through a small quantum dot coupled to superconducting leads. *Physical Review B* **55**, R6137–R6140 (1997).
152. Feist, A. *et al.* Quantum coherent optical phase modulation in an ultrafast transmission electron microscope. *Nature* **521**, 200–203 (2015).
153. Soerensen, O. H., Kofoed, B., Pedersen, N. F. & Shapiro, S. Microwave dependence of subharmonic gap structure in superconducting junctions. *Physical Review B* **9**, 3746–3756 (1974).

- 154. Cuevas, J. C., Heurich, J., Martín-Rodero, A., Yeyati, A. L. & Schön, G. Subharmonic Shapiro Steps and Assisted Tunneling in Superconducting Point Contacts. *Physical Review Letters* **88**, 157001 (2002).
- 155. Tao, T. *Topics in random matrix theory* (American Mathematical Society, 2012).
- 156. Melin, R., Danneau, R., Yang, K., Caputo, J.-G. & Doucot, B. Engineering the Floquet spectrum of superconducting multiterminal quantum dots. *Physical Review B* **100**, 035450 (2019).

Acknowledgements

At this point, I would like to thank numerous people who have helped me throughout the course of my dissertation.

Firstly, I am grateful for **Priv.-Doz. Dr. Christian Ast** for taking me into his group and giving me guidance and advice at all stages of the project. Secondly I would like to thank **Prof. Klaus Kern** for letting me join his department and allowing me to benefit from its infrastructure.

A warm "Thank you" goes to the members of the Ast Group, in particular **Maneesha Ismail, Dr. Haonan Huang, Dr. Piotr Kot, Dr. Maximilian Uhl, Dr. Robert Drost, Soumyaranjan Jhankar** and **Dr. Sujoy Karan** . It was a pleasure to work with all of you and I am grateful for the many things I learned from all of you.

The theoretical part of this thesis would not have been possible without the valuable help of **Prof. Juan Carlos Cuevas** and I would like to express my appreciation for his constructive and inspiring inputs. I also thank **Dr. Ciprian Padurariu, Dr. Björn Kubala** and **Prof. Joachim Ankerhold** for interesting discussions in Ulm and Stuttgart.

I express my gratitude to **Peter Andler** for taking responsibility for the setup of the chamber and for his hands-on help with maintenance of the setup. I am grateful to **Wolfgang Stiepany** for teaching me CAD and for his expertise with engineering and I thank **Marco Memmler** for helping me with the construction of various accessories. Many thanks also to **Isabel Pfänder** for the help with various cables.

For the high frequency, I acknowledge previous work from **Dr. Stefan Wunsch, Prof. Reinhold Kleiner, Prof. Michael Siegel** and **Jonas Merkt**. The Josephson junction arrays have been supplied **Prof. Oliver Kieler** and I am grateful for his explanations. I thank **Marion Hagel** for meticulous work with the wire bonding.

Importantly, I also thank all the other members of the Nanoscale Science Department for the discussions and fun moments we shared, most notably **Dr. Manish Garg, Dr. Alberto Martín-Jiménez, Dr. Dhaneesh Golapakrishnan, Dr. Kelvin Anggara, Dr. Abhishek Grewal, Dr. Anna Rosławska, Dr. Tomasz Michnowicz, Dr. Sven Szilagyi, Lukas Powalla, Sayooj Satheesh, Dr. Yuqi Wang, Dr. Christopher Leon, Dr. Aparajita Singha, Dinesh Pinto, Dr. Domenico Paone, Dr. Toni Hache, Dr. Klaus Kuhnke, Dr. Rico Gutzler, Tobias Wollandt** and **Aditya Desai**.

I thank **Sabine Birtel** and **Robert Müller** for their competent and timely support with administrative tasks. I owe **Paul Huber**, **Christiane Baumgartner** and **Detlef Wimmer** a "Thank you" for their reliable support with everything related to cryogenics. I thank **Dr. Michael Krzyzowski** and **Gottfried Eisele** for their help with the cryostat.

Finally I am indebted to my friends, my family and my girlfriend for their love and for being there for me at all times.

Curriculum Vitae

Education

09/2018–now PhD Student, IMPRS-CMS

Max-Planck-Institute for Solid State Research and University of Stuttgart

- „Resolving Tunneling Processes into Yu-Shiba-Rusinov States under Microwave Irradiation”, supervisor: Priz.-Doz. Dr. Christian Ast

10/2014–06/2018 M.Sci., B.A. Natural Sciences (Physics)

University of Cambridge, United Kingdom

- „Spin Transport in Organic Semiconductors”, supervisor: Prof. Henning Sirringhaus

09/2008–07/2014 Allgemeine Hochschulreife

Albertus-Magnus-Gymnasium Bensberg, Bergisch Gladbach

Publications

1. Siebrecht J., Huang H., Drost R., Padurariu C., Kubala B., Levy Yeyati A., Cuevas J.C., Ankerhold J., Ast C.R. Microwave Excitation of Atomic Scale Yu-Shiba-Rusinov States, *in preparation*
2. Kot P., Ismail M., Siebrecht J., Drost R., Ast. C.R. Electric field control of spin transitions on the atomic scale. *submitted*
3. Drost R., Uhl M., Kot P., Siebrecht J., Schmid A., Merkt J., Wunsch S., Siegel M., Kieler O., Kleiner R., Ast C.R. Combining electron spin resonance spectroscopy with scanning tunneling microscopy at high magnetic fields. *Review of Scientific Instruments* **93**, 043705 (Apr. 2022).
4. Wang S.-J., Venkateshvaran D., Mahani M.R., Chopra U., McNellis E.R., Di Pietro R., Schott S., Wittmann A., Schweicher G., Cubukcu M., Kang K., Carey R., Wagner T.J., Siebrecht J.N.M., Wong D.P.G.H., Jacobs I.E., Aboljadayel R.O., Ionescu A., Egorov S.A., Mueller S., Zadvorna O., Skalski P., Jellett C., Little M., Marks A., McCulloch I., Wunderlich J., Sinova J., Sirringhaus H. Long spin diffusion lengths in doped conjugated polymers due to enhanced exchange coupling. *Nature Electronics* **2**, 98-107 (Mar. 2019)

Eigenständigkeitserklärung

Schriftliche Bestätigung der eigenständig erbrachten Leistung gemäß § 6 Absatz 2 der Promotionsordnung der Universität Stuttgart

Die eingereichte Dissertation zum Thema „Resolving Tunneling Processes into Yu-Shiba-Rusinov States under Microwave Irradiation“ stellt meine eigenständig erbrachte Leistung dar.

Ich habe ausschließlich die angegebenen Quellen und Hilfsmittel benutzt. Wörtlich oder inhaltlich aus anderen Werken übernommene Angaben habe ich als solche kenntlich gemacht.

Die Richtigkeit der hier getätigten Angaben bestätige ich und versichere, nach bestem Wissen die Wahrheit erklärt zu haben.

Stuttgart, den